Universality in Systems of up to Four Particles – From Nuclei to Ultracold Atoms

Dissertation

von

Christiane Schmickler

Darmstadt 2019

Universality in Systems of up to Four Particles – From Nuclei to Ultracold Atoms

Dem Fachbereich Physik

der Technischen Universität Darmstadt

zur Erlangung des Grades

eines Doktors der Naturwissenschaften (Dr. rer. nat.)

vorgelegte Dissertation von

Christiane Schmickler

aus Bonn

Erstgutachter: Prof. Dr. Hans-Werner Hammer
Zweitgutachter: Prof. Dr. Robert Roth

Darmstadt 2019

Schmickler, Christiane : Universality in Systems of up to Four Particles – From Nuclei to Ultracold Atoms
Darmstadt, Technische Universität Darmstadt,
Jahr der Veröffentlichung der Dissertation auf TUprints: 2020
URN: urn:nbn:de:tuda-tuprints-117800
Tag der mündlichen Prüfung: 20.05.2019

Abstract

Universal physics manifests in low-energy phenomena over a large array of different systems from nuclear to atomic physics.
Here, two interesting aspects of universality are studied using the Gaussian Expansion Method (GEM). This is a variational method that uses products of Gaussians as basis functions. Gaussian potentials are used as a short-range potential. The first aspect is the behaviour close to the dimer + atom breakup threshold of Efimov states and associated universal tetramers in ultra-cold mixtures of alkali atoms. These can be treated as bosons here. It is shown that trimer and tetramer vanish into the threshold at almost the same point.
The predictions of effective Efimov states in the vicinity of the dimer + atom breakup threshold are addressed, but the results are inconclusive.
The second aspect is the interplay between universal states of up to four bosons and the Coulomb interaction. This is interesting because it opens up nuclear physics to the investigation.
First, the effect of the Coulomb interaction on universal states is studied in natural units. This introduces a scale for the Coulomb potential's strength relative to the strength of the short-range Gaussian potential. A generalised Efimov plot of the binding energies of states of charged bosons versus the Coulomb-modified scattering length is shown. This plot illustrates the impact of different relative strengths of the Coulomb potential on universal states.
To complement this analysis, the structure is also calculated via root mean square (rms) radius calculations and contour plots.
The results are then applied to the excited state of ^{17}F, which has a proton halo. The binding energy of this state can be reproduced after fixing the effective range of the potential to the physical value.
The $N\alpha$ system proved more problematic. It was found that the ground state of ^{12}C was too deep to be described within the framework used and the highest excited state of ^{16}O below the 4α breakup threshold proved difficult to describe. I discuss possible reasons for this.
In the last part I studied the zero-range limit in the presence of the Coulomb interaction. I show that my results for the dimer and trimer can be rescaled to coincide with the zero-range result. An extrapolation towards the zero-range limit for the tetramer ground state is also presented.

Zusammenfassung

Universelle Physik zeigt sich in Niedrigenergiephänomenen in vielen verschiedenen Systemen von Kern- bis Atomphysik.
Hier werden zwei interessante Aspekte der Universalität mit der GEM (Gauß-Funktion-Entwicklungs-Methode) untersucht. Dies ist eine Methode mit Produkten von Gaußschen Funktionen als Basisfunktionen, die das Variationsprinzip benutzt. Dabei werden Gauß-Potentiale als kurzreichweitige Potentiale benutzt. Der erste Aspekt ist das Verhalten von Efimovzuständen und dazugehörigen universellen Tetrameren in ultrakalten Mischungen von Alkaliatomen in der Nähe der Dimer-Atom-Zerfalls-Schwelle. Die Alkaliatome können hier als Bosonen behandelt werden. Es wird gezeigt, dass Trimer and Tetramer fast im selben Punkt in die Schwelle verschwinden.
Die Vorhersagen bezüglich effektiver Efimovzustände in der Nähe der Dimer-Atom-Zerfalls-Schwelle werden diskutiert, aber die Ergebnisse sind nicht eindeutig.
Der zweite Aspekt ist das Zusammenspiel von universellen Zuständen von bis zu vier Bosonen mit der Coulomb-Wechselwirkung. Dadurch können auch kernphysikalische Systeme untersucht werden.
Als erstes werden die Auswirkungen der Coulomb-Wechselwirkung auf universelle Zustände in natürlichen Einheiten untersucht. Dadurch wird eine Skala für die Stärke der Coulomb-Wechselwirkung relativ zur Stärke des kurzreichweitigen Gauß-Potentials eingeführt. Ein generalisierter Efimovplot der Bindungsenergie von Systemen geladener Bosonen als Funktion der Coulomb-modifizierten Streulänge wird gezeigt. Dies illustriert den Einfluss von verschieden starken Coulomb-Potentialen auf die universellen Zustände. Dabei ist stark oder schwach relativ zum kurzreichweitigen Potential zu verstehen.
Um diese Untersuchung zu ergänzen, wird außerdem die Struktur der Zustände über quadratische Mittelwertsradien und Konturenplots ermittelt.
Die Ergebnisse werden dann auf den angeregten Zustand von ^{17}F, einen Protonhalokern, angewandt. Die Bindungsenergie konnte reproduziert werden, nachdem die effektive Reichweite des kurzreichweitigen Potentials auf den physikalischen Wert festgelegt wurde.
Das $N\alpha$-System stellte sich als problematischer heraus. Der Grundzustand von ^{12}C erwies sich als zu tief für die Beschreibung innerhalb des hier vorgestellten Rahmens. Der höchste angeregte Zustand von ^{16}O unter der 4α-Schwelle war schwer zu beschreiben. Dafür werden mögliche Gründe diskutiert.
Im letzten Teil wurde der Null-Reichweiten-Grenzwert in Anwesenheit der Coulomb-Wechselwirkung untersucht. Es wird gezeigt, dass die Ergebnisse für den Dimer und Trimer reskaliert werden können, sodass sie mit dem Null-Reichweiten-Ergebnis übereinstimmen. Außerdem wird eine Extrapolation zum Null-Reichweiten-Grenzwert für den Tetramergrundzustand präsentiert.

Contents

1 Introduction

Universality is an intriguing aspect of physics, because it means that regardless of the specifics of the short-range interaction, the same universal bound states can form as long as the scattering length is large compared to the range of the potential.

This has implications for several fields where there are short-range interactions, notably nuclear physics, which has the short-ranged nuclear force, atomic physics, with the van-der-Waals force that falls off very quickly and effective short-range interactions between polarons.

Unsurprisingly, this has spurred a lot of research into many aspects of universal phenomena, the earliest of which is probably the universal dimer which was found by Wigner [1]. Thomas [2] showed in 1935 that three particles interacting with a zero-range pair interaction have a binding energy that is unbounded from below, which is known as the "Thomas collapse". This was a first step in a series of investigations that led to Efimov's formulation of the "Efimov effect" in [3], where he showed that a resonant two-body interaction in a system of three bosons leads to a tower of three-body bound states with a fixed scaling factor. In the limit where the scattering length becomes infinite, he even found infinitely many states. He notes that this "effect does not depend on the form of two-body forces – it is only their resonant character" that is required [3].

Interesting in this light were also the findings of Phillips and Tjon around this time, which connected the atom-dimer scattering length and the three-body binding energy [4] and the four-body and three-body binding energy [5] in a system of nuclons when calculated with different potentials that have the same scattering length and effective range. This also hinted at physics that were completely determined by a few parameters and only required one further three-body parameter to completely determine, which is also the case for the Efimov effect that features a discrete scaling that can be anchored by one three-body parameter.

Efimov tried to apply his findings qualitatively to nuclear physics, namely the three α system and the three nucleon system in [3], which he noted have both resonant interactions. He concluded however that more exact calculations were needed to ascertain whether the Efimov effect could be found in these systems.

After Efimov led the way, many investigations into universal physics followed. Amado & Greenwood investigated the four-body system and found no comparable effect [6]. Efimov himself further investigated and refined his formulations [7, 8]. Braaten *et al.* found a univeral equation for Efimov states [9].

Several authors pursued the idea of universal physics in nuclear physics further, Efimov himself and others for the N-nucleon problem [10–13], some for the three-α problem [14–16], some for halo nuclei [17–19], and some even on the boundary to particle physics, taking into account mesons [20].

Other authors proposed to investigate atomic physics systems, for example ^{4}He [21, 22] and loss rates in Bose-Einstein Condensates [23–25]. Using Feshbach-resonances [26, 27] to tune the scattering length to the unitary limit in experiments enabled the experimental discovery of Efimov states [28–31]. This spurred even more investigation, especially into experimentally accessible systems such as alkali atoms [32] and mixtures thereof [33–38].

Another direction that has been taken was to investigate universal states in systems of N bosons [39–50]. While not a true Efimov effect, interesting universal N-body states attached to each

Efimov trimer have been found in these studies.
Even effective Efimov trimers made up of a dimer and two atoms have been proposed [35, 51–53]. Experiments have kept up with this developement, investigating mixtures [54–59] and higher N-body universal states [60]. Imaging techniques have also been used to investigate Efimov states [61].
This thesis aims to contribute to this growing field in two main regions:

1. Mass-imbalanced cold-atom systems near the dimer threshold, where the aforementioned effective Efimov trimers have been predicted to arise, and

2. Revisiting the interplay of the Coulomb interaction with universal states in order to better understand them in the context of nuclear physics.

To this end, I will first introduce some general concepts in Chapter 2 and the methods I have used for the calculations in Chapter 3.
Then I will present my results for the mass-imbalanced cold-atoms systems in Chapter 4 and for the univeral aspects with the Coulomb interaction in Chapter 5. The results presented here were obtained in collaboration with H.-W. Hammer, E. Hiyama and in part A. G. Volosniev, and were published in [62–66].

2 General Concepts

In the following, some concepts are introduced that are important for the understanding of the topics presented in this thesis. The scattering length and how to calculate it will be explained, also for the case that a Coulomb interaction is present. Then I give a very short introduction into Effective Theories and Universality, and present the physical systems that will be important for the applications.

2.1 Scattering Length

The scattering length is an important parameter when treating low-energy physics. It describes scattering off a short-range potential at zero energy and is often the only parameter needed to describe universal phenomena, see Section 2.3.
It is related to the scattering phase shift through the effective range expansion

$$k \cot \delta_0 = -\frac{1}{a} + \frac{1}{2} r_{\text{eff}} k^2, \tag{2.1}$$

where δ_0 is the s-wave phase shift, k is the momentum, a is the s-wave scattering length and r_{eff} is the effective range[67]. Only the s-wave scattering length is treated here, because it is the only one that is needed in the following.
Taking only the leading order of Eq. (2.1) gives

$$k \cot \delta_0 = -\frac{1}{a}, \tag{2.2}$$

which can be rearranged to

$$a = -\frac{\tan \delta_0}{k}. \tag{2.3}$$

So, to find the scattering length for any given short-range potential one has to calculate the phase shift.

2.1.1 Calculation of the Scattering Length for a Given Short-Range Potential

To this end, one can divide space into an outside part ($r > R_0$), where the short-range potential has fallen off sufficiently to disregard it, and an inside part ($r \leq R_0$), where the potential has a significant impact. Since we consider s-wave scattering, we only have to treat the radial part.
So we consider the following Schrödinger Equation[1]:

$$E\varphi(r) = \begin{cases} \left(-\frac{\hbar^2}{2\mu}\frac{\partial^2}{\partial r^2} + V(r)\right)\varphi(r), & \text{for } r \leq R_0 \\ -\frac{\hbar^2}{2\mu}\frac{\partial^2}{\partial r^2}\varphi(r), & \text{for } r > R_0 \end{cases} \tag{2.4}$$

[1]For s-waves, the one-dimensional Schrödinger Equation can be shown to be equivalent to the radial part of the three-dimensional equation, see Appendix A.

A solution for the wave function in the outside region is

$$\varphi(r) = A(\sin(kr) + \tan\delta\cos(kr)) \tag{2.5}$$

with

$$E = \frac{\hbar^2 k^2}{2\mu} \tag{2.6}$$

and A an overall amplitude. Taking the derivative of the wave function yields

$$\varphi'(r) = A(k\cos(kr) - k\tan\delta\sin(kr)). \tag{2.7}$$

Equating the logarithmic derivative of the outside wave function to that of the inside wave function $\psi(r)$ at the boundary R_0 leads to the following equation:

$$\frac{\psi'(R_0)}{\psi(R_0)} = \frac{k\cos(kR_0) - k\tan\delta\sin(kR_0)}{\sin(kR_0) + \tan\delta\cos(kR_0)}. \tag{2.8}$$

Rearranging this and solving for $\tan\delta/k$ yields

$$\frac{\tan\delta}{k} = \frac{\psi(R_0)\cos(kR_0) - \psi'(R_0)\frac{\sin(kR_0)}{k}}{\psi'(R_0)\cos(kR_0) + \psi(R_0)k\sin(kR_0)}. \tag{2.9}$$

Taking the zero-energy limit $k \to 0$ one can replace $\cos(kR_0)$ by 1 and $\sin(kR_0)$ by kR_0. This yields

$$\frac{\tan\delta}{k} = \frac{\psi(R_0) - \psi'(R_0)R_0}{\psi'(R_0)}, \tag{2.10}$$

where $k^2 \approx 0$ has been used.
It can be shown that the δ in Eqs. (2.5) and (2.10) is consistent with other definitions of the phase shift and thus the δ_0 from Eq. (2.1), see Appendix A.1, which means that the left hand side of Eq. (2.10) is $-a$.
Therefore, to obtain the scattering length a one needs $\psi(R_0)$ and $\psi'(R_0)$. Since the inside and outside wave functions should be smooth at R_0, one can calculate the inside wave functions at R_0 numerically and by setting

$$\psi_{\text{in}}(R_0) = \psi(R_0) \tag{2.11}$$
$$\psi'_{\text{in}}(R_0) = \psi'(R_0) \tag{2.12}$$

one obtains the final formula

$$a = \frac{\psi'_{\text{in}}(R_0)R_0 - \psi_{\text{in}}(R_0)}{\psi'_{\text{in}}(R_0)}. \tag{2.13}$$

2.1.2 Coulomb-Modified Scattering Length

The Coulomb potential cannot be treated as a short-range potential because it only drops off as $1/r$. Because of this, the scattering length as presented above is ill-defined when a Coulomb potential is present. There is, however, an alternative way to define a scattering length in this case.
Instead of considering an outside solution of free waves, which as already mentioned cannot be done in the Coulomb case, one can consider Coulomb wave functions as the outside solutions and then calculate the scattering length in the same way as before.
This will yield a Coulomb-modified scattering length (a_C) and a Coulomb-modified effective range (r_{eff}^C).

To illustrate, I introduce the Coulomb potential as follows

$$H = -\frac{\hbar^2}{2\mu}\frac{\partial^2}{\partial r^2} + V_s(r) + \hbar c Z_1 Z_2 \frac{\alpha}{r}, \tag{2.14}$$

where μ is the reduced mass of the two scattered particles, $V_s(r)$ is the short-range potential present in addition to the Coulomb potential, c is the speed of light, Z_i are the charge numbers of the particle i and α is the fine-structure constant.
The Coulomb-modified effective range expansion for s-waves, i.e. the analogue of Eq. (2.1), is

$$C_{\eta,0}^2 k \cot\tilde{\delta}_0(k) + \gamma h(\eta) = -\frac{1}{a_C} + \frac{1}{2} r_{\text{eff}}^C k^2 + \ldots, \tag{2.15}$$

where

$$C_{\eta,0}^2 = \frac{2\pi\eta}{e^{2\pi\eta} - 1} \tag{2.16}$$

is the Sommerfeld factor with the dimensionless variable

$$\eta = \frac{\gamma}{2k} = \frac{\mu c}{\hbar} Z_1 Z_2 \frac{\alpha}{k}. \tag{2.17}$$

The constant γ is

$$\gamma = 2\frac{\mu c}{\hbar}\alpha Z_1 Z_2 \tag{2.18}$$

and has the dimension [length^{-1}]. The function $h(\eta)$ is

$$h(\eta) = \text{Re}\left(\frac{\Gamma'(i\eta)}{\Gamma(i\eta)}\right) - \log(\eta), \tag{2.19}$$

which contains the Γ function and its derivative. More detail about the derivation can be found in [68–70].
From these formulae it can be easily seen that taking $k \to 0$ as in the previous calculation of the scattering length will introduce complications.
This necessitates calculating for k close to zero and then extrapolating to $k \to 0$. To find the Coulomb-modified scattering length and the Coulomb-modified effective range, one can calculate the left-hand side of Eq. (2.15) for different k^2 and then fit a straight line through the resulting points, which yields $r_C/2$ as the slope and $-\frac{1}{a_C}$ as y-axis intercept. This is illustrated in Fig. 2.1.
To calculate the left-hand side of Eq. (2.15), the phase shift has to be calculated. This can be done much in the same way as described for the case without Coulomb interaction.
To this end, one can consider the radial Schrödinger equation

$$E\varphi(r) = \begin{cases} \left(-\frac{\hbar^2}{2\mu}\frac{\partial^2}{\partial r^2} + V(r) + \hbar c Z_1 Z_2 \frac{\alpha}{r}\right)\varphi(r), & \text{for } r \le R_0 \\ \left(-\frac{\hbar^2}{2\mu}\frac{\partial^2}{\partial r^2} + \hbar c Z_1 Z_2 \frac{\alpha}{r}\right)\varphi(r), & \text{for } r > R_0 \end{cases} \tag{2.20}$$

with an inside region where the short-range potential has some effect and an outside region where it is 0.
The outside solution is known to be composed of the Coulomb wave functions, $F_0(r)$ and $G_0(r)$, where $F_0(r)$ cannot be the solution for the free Coulomb case, because that would lead to a singularity at $r = 0$.
But with a short-range potential added, the outside wave function can be shifted

$$\varphi(r) \propto \cot\tilde{\delta}_0(k) F_0(r) + G_0(r), \tag{2.21}$$

where $\tilde{\delta}_0$ is the phase shift. It can be expressed as

$$\cot\tilde{\delta}_0(k) = -\frac{G_0(r_{\text{zero}})}{F_0(r_{\text{zero}})}, \tag{2.22}$$

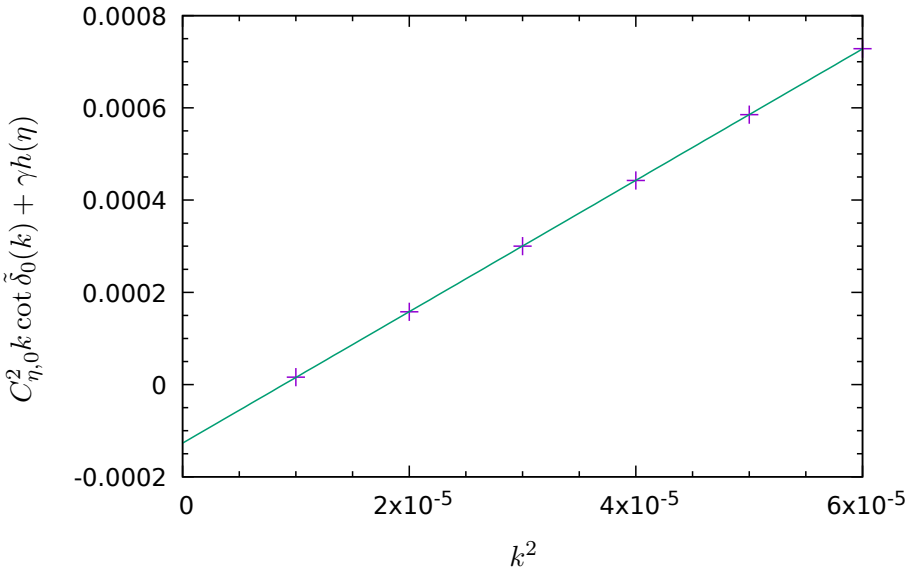

Figure 2.1: Example of the procedure to calculate the Coulomb-modified scattering length and the Coulomb-modified effective range expansion from Eq. (2.15). The calculations are for $\tilde{c} = 0.7$, $V_0 = -0.00219$ and $r_0 = 40$ in dimensionless units where $\hbar = 1$, $c = 1$ and $m = 1$.

with r_{zero} a zero of $\varphi(r)$.
With this connection in place, all that is left to be done is calculate $\varphi(r)$ for $r < nR_0$ numerically (where n can be adjusted during the calculation but is typically of order 500 to make sure that direct effects of the short-range potential have tapered off at the upper limit) and find a zero of $\varphi(r)$ outside of the range of the short-range potential R_0 to be able to calculate the phase shift.
Repeating these steps for different k allows one to extract a_C and r_{eff}^C for each set of V_0, r_0, which are parameters for the short-range Gaussian potential which will be introduced in Section 3.3, and c_c, which is defined as

$$c_c = \hbar c Z_1 Z_2 \alpha. \tag{2.23}$$

The Coulomb-modified effective range expansion parameters a_C and r_{eff}^C can be extracted with very high accuracy, with errors which are negligible in comparison to other uncertainties arising in the calculations presented in the main part. They will therefore not be discussed in the following.

2.2 Effective Theories

One of the underlying principles of physics is that for a specific domain, it is possible to find a theory that describes phenomena in this domain correctly without any knowledge about what happens outside this domain. Historically this behaviour has made possible the development of theories that were later found to be approximations of more complex theories for a specific domain. To name a few examples, Newtonian mechanics can be regarded as a low-velocity approximation of special relativity, or the theory of atomic nuclei consisting of nucleons instead of just being "elementary" particles as they are treated in chemistry, where energies that are sufficiently high to resolve this are not reached.
One interesting aspect of such theories is that they usually contain constants that cannot be further explained within the theory, but can be calculated from underlying principles when such principles become known. For example when considering atomic nuclei as "elementary" particles one has to include constants in the theory describing the masses and other properties, which can in principle be calculated from the masses and interactions of nucleons.

In the history of physics, the direction has usually been going from specialised theory to more complex underlying theory. This has often been due to the fact that new experiments probing new domains showed that the theory is not sufficient to describe everything.
However, as the complexity of underlying theories increases and surpasses computational capabilities, as with QCD, the other direction, going from underlying theory to specialised theory that is easier to calculate, has gained interest. This has led to the development of effective field theories, which provide a systematic way of deriving a low-energy theory from an underlying theory, especially QCD. Crucial for the success of this approach is the fact that they also provide a way to quantify approximation errors. Successful examples include the pionless EFT[51] and chiral perturbation theory[71].
An important step when deriving an effective theory is to identify the energy scales of the problem. One has to identify the low-energy scale which should be taken into account explicitly and also a high-energy scale at which the theory should break down. These scales often correspond to the masses of the particles in the problem.
All other values in this system are then described in terms of the scales and constants via dimensional analysis.
An important feature of effective theories are that values can be expanded in the expansion parameter, which is the low-energy scale divided by the high-energy scale. This allows expressions to be calculated order by order, and errors made by omitting the higher orders to be estimated. The coefficients are assumed by the naturalness argument to be of order 1. If that is not the case, usually fine-tuning is involved, i.e. some mechanism that explains why a certain value is much larger or smaller than its natural value would be.
If the scales are chosen correctly and an approximate picture is sought after, often the leading order already suffices to describe the physics.
For some applications it is also possible to derive quantum mechanical descriptions that follow these ideas. For example representing an arbitrary short-range potential simply by a Gaussian potential

$$V(r) = V_0 e^{-\frac{r^2}{r_0^2}} \tag{2.24}$$

is equivalent to a contact term with Gaussian smearing. This represents the leading order term of an effective description of a short-range potential with large scattering length [2] and is therefore only valid for energies well below the natural energy scale

$$E_s = \frac{\hbar^2}{2\mu r_0^2}. \tag{2.25}$$

To illustrate the point about scales from above, r_0 is the short-range scale, which corresponds to the high-energy scale. Things smaller than r_0 cannot be resolved in this theory.

2.3 Universality

As already discussed above in Section 2.1, with short-range potentials it is possible to describe the physics of the outside wave function knowing only the phase shift that is caused by the short-range potential, but not any more detail about it. Shallow and large bound states, that live mostly outside the range of the short-range potential, can be described by this outside wave function as long as a few short-range parameters (most importantly the scattering length) are correctly reproduced[51]. This is also reflected by the fact that a Gaussian potential can be used to describe an arbitrary short-range potential in leading order for this kind of states, as discussed in Section 2.2.

[2] The scattering length has to be large to ensure the separation of scales between the short range physics of order of r_0, which corresponds to the high-energy scale, and the long-range physics of order of the scattering length a, which corresponds to the low-energy scale

This phenomenon, that low-energy physics is independent of the details of the interaction in these cases, is called universality. There are several interesting examples of this.

2.3.1 Universal Dimer

If the scattering length a is large compared to the short-range length scale R_0, a dimer can be formed that is determined only by the scattering length. With μ the reduced mass of the two particles, it has the binding energy

$$B_2 = \frac{\hbar^2}{2\mu a^2} \tag{2.26}$$

and exists only when the scattering length is positive. This connection was first recognised by Wigner[1]. To see where this binding energy comes from, we look again at the Schrödinger Equation for the outside part of the wave function Eq. (2.4).
Since we are considering a bound state now, we know the outside radial wave function to be proportional to $e^{-\kappa r}$ with $\kappa > 0$. On the other hand, for $k \to 0$ the outside Schrödinger Equation just becomes

$$\frac{\partial^2 \varphi(r)}{\partial r^2} = 0, \tag{2.27}$$

which can be solved by

$$\varphi(r) = N(r - a), \tag{2.28}$$

as discussed in Appendix B, with N a normalisation constant and a the scattering length. For $\kappa r \to 0$ the wave function should go to this limit, so expanding the wave function for the outside part yields

$$\tilde{N} e^{-\kappa r} \approx \tilde{N}(1 - \kappa r) = N(r - a), \tag{2.29}$$

with $\tilde{N}$ a new normalisation constant. Comparing coefficients of r and 1 one arrives at

$$\kappa \approx \frac{1}{a} \tag{2.30}$$

for positive a, because κ is positive, which translates into a binding energy of

$$B_2 = \frac{\hbar^2 \kappa^2}{2\mu} \approx \frac{\hbar^2}{2\mu a^2}, \tag{2.31}$$

as claimed above. This relation holds for κr small enough, where the smallest r that can be input here is R_0, the range of the short-range potential, because this discussion is only valid for the outside part of the wave function. This leads to the condition

$$1 \gg \kappa R_0 \approx \frac{R_0}{a}. \tag{2.32}$$

So if the scattering length is large compared to the range R_0 of the potential and positive, the universal dimer is expected to form regardless of the details of the interaction.
Although the universal dimer is often discussed in the context of the deuteron, probably the best example for the universal dimer in nature is the Helium dimer. It is bound very weakly by van-der-Waals forces between the Helium atoms. Different calculations give different scattering lengths of around 190 a.u. [43]. Taking this value, the universal estimate for the binding energy is

$$B_2 = \frac{\hbar^2}{2\mu a^2} = \frac{\hbar^2}{m_{\mathrm{He}} a^2} \approx 1.2\,\mathrm{mK}, \tag{2.33}$$

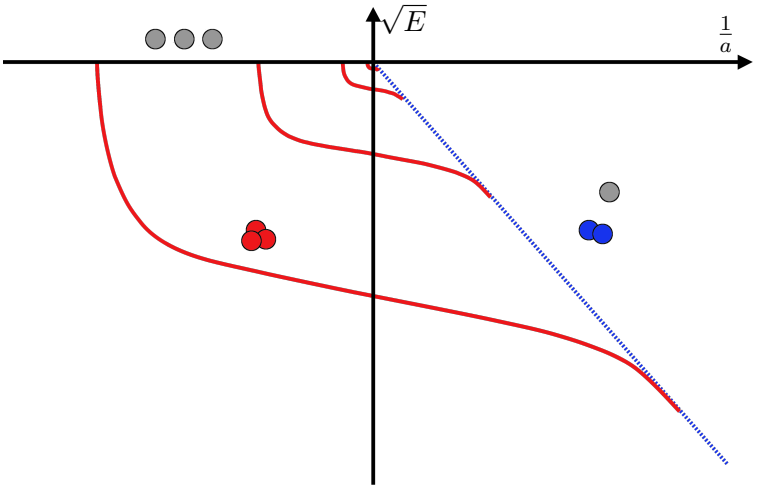

Figure 2.2: Illustration of the Efimov effect in a so-called Efimov plot of the square root of the energy versus the inverse scattering length. The Efimov states are the solid red lines and the universal dimer is shown as a dotted blue line. The scaling factor shown is much smaller than in the identical bosons case, in order to make more states visible.

where

$$\frac{\hbar^2}{m_{\mathrm{He}}} = 43.281307(\text{a.u.})^2\text{K} \tag{2.34}$$

from [43] has been used. Literature values for the Helium dimer range from 1.1 mK [72] for a model-dependent experimental extraction, over ≈ 1.3 mK for calculations with comparatively simple models [43] to ≈ 1.6 mK from a very involved numerical calculation [73]. Thus, the universal dimer value is very close to the binding energy for each of these results.

2.3.2 Efimov Effect

The Efimov effect is a universal effect that can arise in three-body systems. It leads to a distinctive spectrum of states which can be shown in a plot of energy versus the scattering length, see Fig. 2.2. This type of plot is known as the Efimov plot.
Interesting to note are the following features of the Efimov plot:

1. The binding energy in the unitary limit (where $a \to \pm\infty$) of the nth state is related to the binding energy of the next state by a simple factor, called the scaling factor:

$$E_n = \lambda^2 E_{n+1} \tag{2.35}$$

2. The points on the $1/a$-axis where the Efimov states vanish are also governed by the same scaling factor:

$$a_{n+1}^{(-)} = \lambda a_n^{(-)} \tag{2.36}$$

3. Since this pattern theoretically holds for $a \to \pm\infty$, it follows that at unitarity there is an accumulation point with infinitely many infinitely shallow states.[3]

[3]However, since the size of the states is also governed by the same scaling law, the states eventually reach sizes that are larger than the known universe, which means that at some point the theory will break down.

The effect is caused by the emergence of a $1/r^2$ potential in the hyperradius [3]

$$R_{123}^2 = \frac{2}{3}(r_{12}^2 + r_{23}^2 + r_{31}^2) \tag{2.37}$$

for resonant ($a \to \pm\infty$) two-body interaction. For a detailed derivation see [74]. The potential derived in the hyperspherical formalism starting from a zero-range two-body potential has the form

$$V_0(R_{123}) = -\frac{s_0^2 + \frac{1}{4}}{R_{123}^2} \tag{2.38}$$

with $s_0 = 1.00624$ in the case of three identical bosons. Note that for consistency with other coefficients s_n, s_0 is sometimes (for example in [74]) defined as $s_0 = 1.00624i$, i.e. purely imaginary. The whole Schrödinger equation is then

$$\left(-\frac{\partial^2}{\partial R_{123}^2} + V_0(R_{123}) - k^2\right) \sqrt{R_{123}} F_0(R_{123}) = 0, \tag{2.39}$$

where $F_0(R_{123})$ is a hyper-radial function, which connects back to the wave function that solves the original three-body Schrödinger equation via the hyperspherical formalism.
Scaling R_{123} by a factor $1/\lambda$,

$$R_{123} = \lambda R \tag{2.40}$$

and defining $u(r) = \sqrt{r} F_0(r)$, we get

$$\frac{1}{\lambda^2}\left(-\frac{\partial^2}{\partial R^2} + V_0(R) - \lambda^2 k^2\right) u(\lambda R) = 0. \tag{2.41}$$

Defining $\tilde{u}(r) = u(\lambda r)$ and $\tilde{k} = \lambda k$, we have the same equation as before, which is solved by a scaled wave function $\tilde{u}(R)$ for an energy scaled by λ^2. The λ can be pulled out of the equation because the kinetic energy and $V_0(R)$ scale in the same way.
Since this is possible for any λ, there is no lowest bound state. This is known as the Thomas collapse [2]. Setting a boundary condition to remedy this yields a new scale, which is called the three-body parameter. The three-body parameter encapsulates the high-energy physics that occurs for small hyperradii and is connected to the boundary condition, because the boundary condition contains some information about the physics at small hyperradii.
Going back to Eq. (2.39), and imposing a boundary condition on $F_0(R)$ for a small hyperradius, gives a solution proportional to

$$F_0(R) = N_F \cos(s_0 \ln(\Lambda R)), \tag{2.42}$$

where N_F is a normalisation constant and Λ is an inverse length scale. For a detailed derivation see [51][74]. From this one can easily see that scaling R by a factor $\lambda = e^{\tilde{s}}$ yields

$$F_0(\lambda R) = N_F \cos(s_0 \ln(\Lambda \lambda R)) = N_F \cos(s_0(\ln \lambda + \ln(\Lambda R)) = N_F \cos(s_0 \tilde{s} + s_0 \ln(\Lambda R)), \tag{2.43}$$

which equals $\pm F_0(R)$ if

$$s_0 \tilde{s} = n\pi \tag{2.44}$$

for any integer n. The scaling factor λ is therefore

$$\lambda^n = e^{n\frac{\pi}{s_0}}. \tag{2.45}$$

This leads to a discrete scaling symmetry and consequently to the properties of the Efimov states described at the beginning of this section.
Apart from the three identical particle scenario described here, the Efimov effect also occurs for mixtures of particles, albeit with different scaling factors [75]. Particularly, for two heavy bosons and one light particle, the scaling factor is substantially smaller, which makes experimental detection of several consecutive states feasible [51].

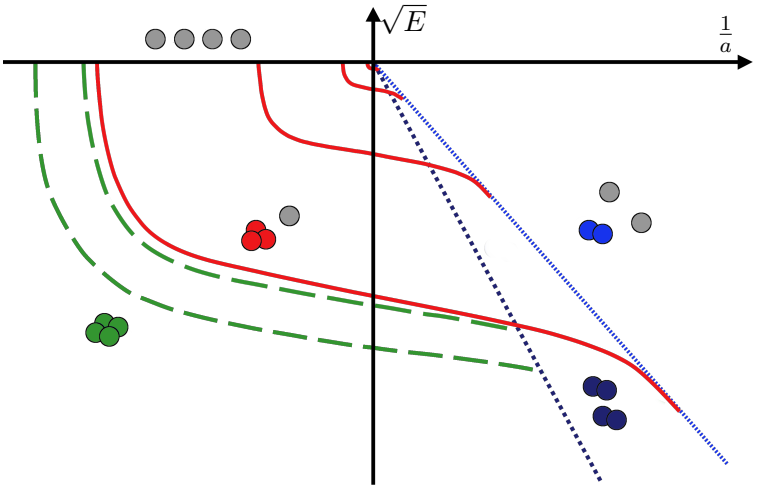

Figure 2.3: Figure 2.2 with added universal tetramer states (shown as a dashed green line) and the two-dimer threshold (dark-blue dotted line). The scaling factors are again not realistic for the identical bosons case in this picture.

2.3.3 Universal N-Body States

After the original discovery of the Efimov effect by Efimov [3], there have been attempts to find a similar effect in higher N-body systems. Amado & Greenwood found that there is no Efimov effect in the four-body system[6], but other universal effects have been found [39][41][76][43]. Platter, Hammer & Meißner showed that for identical bosons there are two universal tetramers attached to the lowest Efimov trimer and von Stecher, D'Incao & Greene showed that these states exist even above the atom-trimer breakup threshold as resonances and suggested they could be detected as loss-features in ultra-cold atom systems. Deltuva finally calculated the ratios in the unitary limit to be

$$\frac{B_{n,1}^{(4)}}{B_n^{(3)}} = 4.610(1) \quad \text{and} \tag{2.46}$$

$$\frac{B_{n,2}^{(4)}}{B_n^{(3)}} = 1.00227(1) \tag{2.47}$$

for high n [45]. The results for the lowest n are usually tainted by the specifics of the potential that was used for the calculation, but higher resonances eventually converge on the universal value. Gattobigio, Kievsky & Viviani further calculated states for five- and six-body systems, where they found that there are also two N-body states attached to each $(N-1)$-body ground state [43]. Going in a slightly different direction, for mixtures of particles of different mass, there are also universal tetramers [35][36]. The number of universal tetramers that can be found for a specific scattering length depends on the mass ratio.

2.3.4 Finite-Range Effects

The relations that have been enumerated in this chapter do not always hold perfectly. In cases where the scattering length is not much larger than the range of the short-range potential or where the energies are so high that some short-range information of the potential can be resolved, so-called

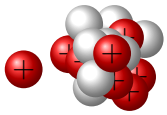

Figure 2.4: Illustration of a halo state consisting of a proton and a tightly bound core.

finite range effects[4] arise.
This means that some dependence on the details of the short-range interaction can be expected, but often, the universal behaviour is preserved in first approximation. However, to accurately predict the outcome of experiments, which are often not carried out in the perfectly universal regime, finite range effects have to be calculated[77, 78].

2.4 Nuclear Structure

Some nuclei will be discussed in the main part, which is why I will introduce some special cases of nuclear structure. Since I concentrate on universal physics, only nuclear states that are weakly bound are of interest.

2.4.1 Halo States

Halo states are nuclei that have a strongly bound core and one or two protons or neutrons that are weakly bound to the core. Examples are ^{11}Be for a one-neutron halo or ^{6}He for a two-neutron halo. An example of a proton halo is ^{17}F, which consists of an ^{16}O core and a proton[79], see the illustration shown in Fig. 2.4. A good overview is presented in [18][19].
Treating the core as one particle, these states can be regarded as few-body systems and calculated using few-body methods. A specialised method is halo effective field theory, used for example in [79][80][81].

2.4.2 α-Clustering

Another interesting aspect of nuclear structure that opens up the possibility to use few-body methods are cluster structures. These form due to the fact that some nuclei are much more deeply bound than others, so that these more tightly bound units can form inside an overall more weakly bound nucleus.
Examples of this include the Hoyle state, an excited state of ^{12}C that is approximately 0.38 MeV above the 3α threshold, and which has received much interest because of its role in the formation of ^{12}C and consequently other elements. It can be described as a cluster of three α particles [7][82][83][84][85]. An illustration is shown in Fig. 2.5.
Clusters of more α particles have also been proposed [86][87][88][89]. For heavier nuclei, ^{12}C or ^{16}O can also be treated as one particle in a clustering approach, because they are also very deeply bound, but here the focus is on α-clusters.

2.5 Cold Atom Physics

The development of techniques in cold atom physics has played a major role in bringing about progress in the field of Efimov physics. After a way to observe Efimov states via loss features was pointed out [23][90], the first experimental observation of Efimov states in 2006[28] spurred a lot

[4] The name comes from using finite range potentials to calculate these effects as opposed to zero-range potentials which by design to not contain these effects and give purely universal results.

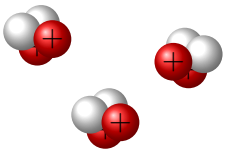

Figure 2.5: Illustration of a dilute state consisting of three α particles.

of investigation into Efimov physics. This approach relies on Feshbach resonances [26, 27], which are tunable by a magnetic field, to change the scattering length. This makes it possible to scan loss rates for a range of scattering lengths and see loss peaks caused by Efimov physics at specific values of the scattering length.
Shortly after the first breakthrough, experiments improved and found Efimov resonances for a variety of atom species and mixtures thereof [54][30], culminating in the observation of more than one Efimov resonance in one experiment, making it possible to confirm the theoretically predicted scaling [31][91][56]. Universal four-body states were also investigated and observed [92]. This in turn motivated theorists to calculate finite range effects that affect the Efimov states away from unitarity and bridge the gap between theory and experimental observation [77][78].
Other recent experimental approaches include imaging techniques [93] and bound state spectroscopy [94].

3 Methods

In this chapter, the methods used in this thesis are introduced. First the Jacobi Coordinates will be introduced, because they form the basis of the understanding of the Gaussian Expansion Method (GEM). Then the GEM will be explained in some detail. At the end I will explain why the Gaussian potential is used in all the calculations presented in this thesis.

3.1 Jacobi Coordinates

Jacobi coordinates are a set of relative coordinates that are useful for the description of few-body systems. They separate the center of mass from the relative coordinates. For a two-body system, the spatial coordinates $\mathbf{x_1}$ and $\mathbf{x_2}$ are replaced by the center of mass coordinates $\mathbf{S}$ and the relative coordinate $\mathbf{r_{12}}$, where

$$\mathbf{S} = \frac{m_1\mathbf{x_1} + m_2\mathbf{x_2}}{m_1 + m_2} \tag{3.1}$$

$$\mathbf{r_{12}} = \mathbf{x_1} - \mathbf{x_2}. \tag{3.2}$$

For the three-body system this can easily be generalised:

$$\mathbf{S} = \sum_{i=1}^{3} \frac{m_i\mathbf{x_i}}{M}, \quad M = \sum_{i=1}^{3} m_i, \tag{3.3}$$

$$\mathbf{r_{12}} = \mathbf{x_1} - \mathbf{x_2}, \tag{3.4}$$

$$\mathbf{R_{12,3}} = \frac{1}{m_1 + m_2}(m_1\mathbf{x_1} + m_2\mathbf{x_2}) - \mathbf{x_3}, \tag{3.5}$$

i.e. the third coordinate points from the center of mass of the first two particles to the third particle.
In the four-body system, there are two different ways to assign coordinates. The Jacobi coordinates in the usual sense just follow the pattern and add a third vector that points from the center of mass of the three-body system to the fourth particle (often called K-configuration):

$$\mathbf{S} = \sum_{i=1}^{3} \frac{m_i\mathbf{x_i}}{M}, \quad M = \sum_{i=1}^{4} m_i, \tag{3.6}$$

$$\mathbf{r_{12}} = \mathbf{x_1} - \mathbf{x_2}, \tag{3.7}$$

$$\mathbf{R_{12,3}} = \frac{1}{m_1 + m_2}(m_1\mathbf{x_1} + m_2\mathbf{x_2}) - \mathbf{x_3}, \tag{3.8}$$

$$\rho_{\mathbf{123,4}} = \frac{1}{m_1 + m_2 + m_3}(m_1\mathbf{x_1} + m_2\mathbf{x_2} + m_3\mathbf{x_3}) - \mathbf{x_4}. \tag{3.9}$$

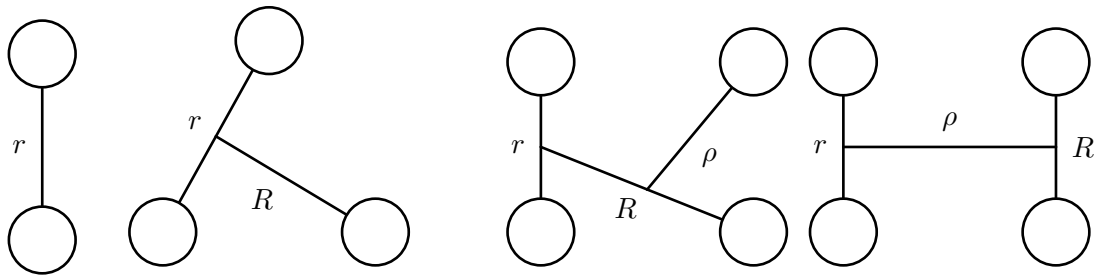

Figure 3.1: Illustration of Jacobi coordinate sets.

But there is also a second way to introduce relative coordinates in the four-body system, which is to form two dimers and connect them by connecting their centers of mass (often called H-configuration):

$$\mathbf{S} = \sum_{i=1}^{3} \frac{m_i \mathbf{x_i}}{M}, \quad M = \sum_{i=1}^{4} m_i, \tag{3.10}$$

$$\mathbf{r_{12}} = \mathbf{x_1} - \mathbf{x_2}, \tag{3.11}$$

$$\mathbf{R_{34}} = \mathbf{x_3} - \mathbf{x_4}, \tag{3.12}$$

$$\rho_{\mathbf{12,34}} = \frac{1}{m_1 + m_2}(m_1\mathbf{x_1} + m_2\mathbf{x_2}) - \frac{1}{m_3 + m_4}(m_3\mathbf{x_3} + m_4\mathbf{x_4}). \tag{3.13}$$

These configurations can be represented pictorially as shown in Fig. 3.1. Except permutations of the particles, these are the only configurations possible in the two-, three-, and four-body systems. Reduced masses corresponding to different Jacobi coordinate sets can be introduced.
For the two-body system, there is obviously only

$$\mu_{r_{12}} = \frac{m_1 m_2}{m_1 + m_2}. \tag{3.14}$$

For three particles, there is an additional

$$\mu_{R_{ij,k}} = \frac{(m_i + m_j)m_k}{m_i + m_j + m_k}, \tag{3.15}$$

and the dimer reduced mass can be defined for all particle pairs

$$\mu_{r_{ij}} = \frac{m_i m_j}{m_i + m_j}. \tag{3.16}$$

In the four-body system two distinct configurations are possible as explained above, so the reduced masses corresponding to the different Jacobi coordinates are

$$\mu_{\rho_{ijk,l}} = \frac{(m_i + m_j + m_k)m_l}{m_i + m_j + m_k + m_l} \tag{3.17}$$

for the K-configuration in addition to the reduced masses defined for the three-body case and

$$\mu_{R_{kl}} = \frac{m_k m_l}{m_k + m_l} \tag{3.18}$$

$$\mu_{\rho_{ij,kl}} = \frac{(m_i + m_j)(m_k + m_l)}{m_i + m_j + m_k + m_l} \tag{3.19}$$

for the H-configuration. In the following, the indices of r, R, ρ are omitted when one set of Jacobi coordinates has been chosen to avoid cluttering of the equations.

3.2 Gaussian Expansion Method

The GEM [95] is a specific iteration of stochastic variational methods that use Gaussian basis functions.
There have been many successful applications, e.g. in hypernuclear systems [96–101] and in atomic systems [102–104].

3.2.1 Variational Methods

The underlying principle of variational methods is that when calculating the energy eigenvalue of a Hamiltonian with an approximate eigenfunction the resulting energy will be higher than that calculated with the exact function[105–108].
This is known as the Ritz variational principle[108–111]:

$$E_0 = \frac{\langle \Psi_0 | \, H \, | \Psi_0 \rangle}{\langle \Psi_0 \mid \Psi_0 \rangle} \geq E_{\text{exact}}, \tag{3.20}$$

where Ψ_0 is the test function, H is the Hamiltonian and E_0 is the approximated energy.
This can be exploited to find a good numerical approximation of the lowest eigenfunctions by simply starting from a generic set of functions and finding the function that gives the lowest energy value. This can be done iteratively, modifying the current best function in random ways to find an increasingly better approximation of the wave function.
There are many different methods based on this idea, which differ mainly in their choice of basis functions. For example explicitly correlated Gaussians use basis functions of the form

$$e^{-\mathbf{x}^T A \mathbf{x}} = \exp\left(- \sum_{j>i=1}^{N} \alpha_{ij} (\mathbf{r}_i - \mathbf{r}_j)^2 - \sum_{i=1}^{N} \beta_i \mathbf{r}_i^2 \right), \tag{3.21}$$

where A is an $n \times n$ symmetric positive-definite matrix of variational parameters and $\mathbf{x}$ is a vector containing $\mathbf{r}_i$, the positions of particles i in space. The variational parameters α_{ij} and β_i can be related back to A_{ij}. Here, α_{ij} are connected explicitly to the pair correlations between particles i and j, which is where the name "explicitly correlated Gaussians" comes from[106, 108].
Sums and/or products of Gaussian functions with several coefficients are a popular choice for the basis functions. A difference between methods is also how many iterations are typically needed to reach convergence and how much knowledge about the state is input a priori.
On one side of the spectrum are methods that start with very few basis functions and increase the number in each step [105–108, 112] and on the other side are methods that give a very good initial result when the parameters are chosen well and do not require many iterations to ascertain convergence if the precision that is needed is not too high. The GEM that I used here falls into the latter category.

3.2.2 Basis Functions for the Gaussian Expansion Method

The basis functions are constructed by taking a Jacobi coordinate configuration (or several) and representing each Jacobi coordinate by a Gaussian function. This yields a total wave function Ψ as explained in the following.
For each Jacobi coordinate, the basis functions are

$$\phi_{nlm}(\mathbf{r}) = \phi^{\text{G}}_{nl}(r) Y_{lm}(\widehat{\mathbf{r}}), \qquad \phi^{\text{G}}_{nl}(r) = N_{nl}\, r^l e^{-(r/r_n)^2}, \tag{3.22}$$

$$\psi_{NLM}(\mathbf{R}) = \psi^{\text{G}}_{NL}(R) Y_{LM}(\widehat{\mathbf{R}}), \qquad \psi^{\text{G}}_{NL}(R) = N_{NL}\, R^L e^{-(R/R_N)^2}, \tag{3.23}$$

$$\xi_{\nu\lambda\mu}(\rho) = \xi^{\text{G}}_{\nu\lambda\mu}(\rho) Y_{\lambda\mu}(\widehat{\rho}), \qquad \xi^{\text{G}}_{\nu\lambda}(\rho) = N_{\nu\lambda}\, \rho^\lambda e^{-(\rho/\rho_\nu)^2}, \tag{3.24}$$

where N_{nl}, N_{NL}, $N_{\nu\lambda}$ denote the normalization constants. The range parameters of the Gaussians are given as shown in the following, which leads to a geometric progression:

$$r_n = r_{\min}\, a^{n-1}, \qquad a = \left(\frac{r_{\max}}{r_{\min}}\right)^{\frac{1}{n_{\max}-1}} \qquad (n = 1, ..., n_{\max}), \tag{3.25}$$

$$R_n = R_{\min}\, A^{N-1}, \qquad A = \left(\frac{R_{\max}}{R_{\min}}\right)^{\frac{1}{N_{\max}-1}} \qquad (N = 1, ..., N_{\max}), \tag{3.26}$$

$$\rho_n = \rho_{\min}\, \alpha^{\nu-1}, \qquad \alpha = \left(\frac{\rho_{\max}}{\rho_{\min}}\right)^{\frac{1}{\nu_{\max}-1}} \qquad (\nu = 1, ..., \nu_{\max}). \tag{3.27}$$

The geometric progression ensures that short-range and long-range correlations can both be described very well at the same time. This property is important for both applications presented here (see Chapter 4 and Chapter 5).
The total wave function is then

$$\Psi^{\text{trimer}}_{JM} = \sum_c \sum_{n_c} \sum_{N_c} \sum_{\ell_c} \sum_{L_c} C^{(c)}_{n_c\ell_c N_c L_c} \sum_{b\in p(c)} [\phi^{(c)}_{n_c\ell_c}(\mathbf{r}_b)\psi^{(c)}_{N_cL_c}(\mathbf{R}_b)]_{JM}, \tag{3.28}$$

$$\Psi^{\text{tetramer}}_{JM} = \sum_c \sum_{n_c} \sum_{N_c} \sum_{\nu_c} \sum_{\ell_c} \sum_{L_c} \sum_{\lambda_c} C^{(c)}_{n_c\ell_c N_c L_c\nu_c\lambda_c} \sum_{b\in p(c)} [[\phi^{(c)}_{n_c\ell_c}(\mathbf{r}_b)\psi^{(c)}_{N_cL_c}(\mathbf{R}_b)]_I \xi^{(c)}_{\nu_c\lambda_c}(\rho_b)]_{JM}, \tag{3.29}$$

where c is the so-called configuration channel (illustrated in Fig. 3.1) and $p(c)$ are all possible permutations of particles in a given channel. $C^{(c)}_{n_c\ell_c N_c L_c}$ and $C^{(c)}_{n_c\ell_c N_c L_c\nu_c\lambda_c}$ are coefficients.
The basis functions presented here are not orthogonal, which necessitates some care to be taken when calculating matrix elements and eigenvalues, as described in Section 3.2.4 and Section 3.2.5. All calculations here are in leading order and all states of interest have zero total angular momentum which means that all angular momentum quantum numbers (ℓ, L, λ) are taken to be zero. Due to the construction of the total wave function, identical bosons are automatically symmetrized under these conditions. The symmetric construction of the wave function also leads to the implicit inclusion of some higher partial wave contributions. As discussed in Section 3.2.5, this is enough to treat the Coulomb potential accurately, even though higher partial wave contributions are expected in this case.

3.2.3 Schrödinger Equation

To calculate energies and wave functions, the Schrödinger equation has to be solved. Starting from the Schrödinger equation

$$H\psi := (T + V)\psi = E\psi, \tag{3.30}$$

where H is the Hamiltonian, T is the kinetic energy term and V is the potential, while E is an energy eigenstate corresponding to the eigenfunction ψ of H.
Within the method of the GEM, the Schrödinger equation is expanded in the Gaussian basis. The Schrödinger equation for the three-body system then becomes

$$\sum_c \sum_{n_c l_c N_c L_c} \sum_{b\in p(c)} \sum_{b'\in p(c')} C^{(c)}_{n_c l_c N_c L_c} \tag{3.31}$$

$$\times \left\langle [\phi^{(c')}_{n_{c'}\ell_{c'}}(\mathbf{r}_{b'})\psi^{(c')}_{N_{c'}L_{c'}}(\mathbf{R}_{b'})]_{JM} \right| (H - E) \left| [\phi^{(c)}_{n_c\ell_c}(\mathbf{r}_b)\psi^{(c)}_{N_cL_c}(\mathbf{R}_b)]_{JM} \right\rangle = 0. \tag{3.32}$$

The three-body system is taken as an example here. Two- and four-body systems can be treated analogously. The coefficients introduced in Eq. (3.29) then correspond to an eigenvector of the

Hamiltonian, which becomes a matrix when expanded in the Gaussian basis. The last equation can be rewritten as a matrix equation:

$$\sum_{\tilde{n}}(H_{\tilde{n}'\tilde{n}} - EN_{\tilde{n}'\tilde{n}})C_{\tilde{n}} = 0, \tag{3.33}$$

where $H_{\tilde{n}'\tilde{n}}$ and $N_{\tilde{n}'\tilde{n}}$ are matrix elements and will be discussed in more detail in Section 3.2.4 and $\tilde{n}$ and $\tilde{n}'$ are a shorthand for all undashed / dashed indices. The $C_{\tilde{n}}$ are the eigenvector elements that can be used to reconstruct the wave function after solving the equation.
Because the basis functions are not orthogonal, $N_{\tilde{n}'\tilde{n}}$ is a normalization matrix and not the identity matrix. This means that Eq. (3.33) is a general eigenvalue problem which can be solved by standard linear algebra methods. Here, LAPACK's DSPGVX routine was used[113].

3.2.4 Matrix Elements

A strong advantage of the GEM is that matrix elements can be calculated analytically for many widely used potentials. This eliminates potential numerical problems that might arise when calculating matrix elements numerically and enables high precision calculations. All potentials used here were calculated analytically.
To illustrate the method, three-body matrix elements will be shown. The step from three- to four-body is straightforward.
In order to simplify the equations and because the results shown in Chapter 4 and Chapter 5 do not make use of higher angular momenta, the angular momenta l, L are taken to be zero. This eliminates the spherical harmonics.
The full calculations were however done using infinitesimally shifted Gaussians, which are mathematically equivalent to spherical harmonics, but easier to handle in the matrix element calculations. A detailed description of the calculations involved can be found in the appendix of [95].

General Steps

Calculating the matrix elements can be divided into two steps, separating out all prefactors and simplifying the exponents, and then integrating the expression. Starting from

$$\left\langle [\phi^{(c')}_{n_{c'}\ell_{c'}}(\mathbf{r}_a)\psi^{(c')}_{N_{c'}L_{c'}}(\mathbf{R}_a)]_{JM} \right| X(r_d, R_d) \left| [\phi^{(c)}_{n_c\ell_c}(\mathbf{r}_b)\psi^{(c)}_{N_cL_c}(\mathbf{R}_b)]_{JM} \right\rangle, \tag{3.34}$$

where $X(\mathbf{r}_d, \mathbf{R}_d)$ is some function of $\mathbf{r}_d$ and $\mathbf{R}_d$, which are associated to Jacobi coordinate configuration d. This is necessary in order to be able to sum over all configurations for the wave functions on the left and right side and for the inner part separately.
Inserting the definitions of ϕ_{nlm} and ψ_{NLM} yields

$$N_{n_{c'}0}N_{N_{c'}0}N_{n_c0}N_{N_c0}\frac{1}{(4\pi)^2}\left\langle e^{-\nu_{c'}r_a^2}e^{-\lambda_{c'}R_a^2} \right| X(r_d, R_d) \left| e^{-\nu_c r_b^2}e^{-\lambda_c R_b^2} \right\rangle, \tag{3.35}$$

where

$$\nu_c = \frac{1}{r_{n_c}^2} \quad \text{and} \quad \lambda_c = \frac{1}{R_{N_c}^2}. \tag{3.36}$$

In order to reduce this to one r that can be integrated over, the Jacobi coordinates are all transformed into the same configuration.

$$\mathbf{r}_a = \alpha_{ad}\mathbf{r}_d + \beta_{ad}\mathbf{R}_d \qquad \mathbf{r}_b = \alpha_{bd}\mathbf{r}_d + \beta_{bd}\mathbf{R}_d \tag{3.37}$$

$$\mathbf{R}_a = \alpha'_{ad}\mathbf{r}_d + \beta'_{ad}\mathbf{R}_d \qquad \mathbf{R}_b = \alpha'_{bd}\mathbf{r}_d + \beta'_{bd}\mathbf{R}_d \tag{3.38}$$

The factors α_{ad}, β_{ad} etc are easily worked out by replacing $\mathbf{r}_a$ by the appropriate $\mathbf{x}_i - \mathbf{x}_j$ (see the definition of Jacobi coordinates in Section 3.1), and seeing how to combine these to find Jacobi coordinates based on a different pairing of particles.
Taking out the prefactor $N_{n_{c'}0}N_{N_{c'}0}N_{n_c0}N_{N_c0}\frac{1}{(4\pi)^2}$ this yields

$$\left\langle e^{-\nu_{c'}(\alpha_{ad}\mathbf{r}_d+\beta_{ad}\mathbf{R}_d)^2}e^{-\lambda_{c'}(\alpha'_{ad}\mathbf{r}_d+\beta'_{ad}\mathbf{R}_d)^2}\right| X(r_d,R_d)\left|e^{-\nu_c(\alpha_{bd}\mathbf{r}_d+\beta_{bd}\mathbf{R}_d)^2}e^{-\lambda_c(\alpha'_{bd}\mathbf{r}_d+\beta'_{bd}\mathbf{R}_d)^2}\right\rangle. \quad (3.39)$$

As a short-hand notation, I introduce

$$\langle a|\, X(r,R)\,|b\rangle \quad (3.40)$$

for the previous equation. Equation 3.39 can now be rewritten as an integral, where the index d was dropped to simplify the notation:

$$\int \mathrm{d}^3r\mathrm{d}^3R e^{-\nu_{c'}(\alpha_{ad}\mathbf{r}+\beta_{ad}\mathbf{R})^2}e^{-\lambda_{c'}(\alpha'_{ad}\mathbf{r}+\beta'_{ad}\mathbf{R})^2}X(r,R)e^{-\nu_c(\alpha_{bd}\mathbf{r}+\beta_{bd}\mathbf{R})^2}e^{-\lambda_c(\alpha'_{bd}\mathbf{r}+\beta'_{bd}\mathbf{R})^2}. \quad (3.41)$$

At this point, the calculation diverges for different $X(r,R)$.

Normalization Matrix

Since the basis is not orthogonal, the matrix elements of the identity have to be calculated as well. To calculate the normalization matrix, Eq. (3.41) for $X(r,R) = 1$ has to be solved.
This is a special case of the matrix element for a Gaussian potential

$$X(r,R) = V_0 e^{-ur^2}, \quad (3.42)$$

with $u = 0$ and $V_0 = 1$. It will therefore be treated in Section 3.2.4. The result is

$$\langle a|\, 1\,|b\rangle = e^{-A}\left(\frac{\pi}{C}\right)^{\frac{3}{2}}\left(\frac{\pi}{B+\frac{D^2}{C}}\right)^{\frac{3}{2}}, \quad (3.43)$$

with A, B, C, D defined in Eqs. (3.53) to (3.56).

Kinetic Energy Matrix

The kinetic energy term contains derivatives which have to be carried out first:

$$X(r,R) = -\frac{\hbar^2}{2\mu_r}\frac{\partial^2}{\partial r^2} - \frac{\hbar^2}{2\mu_R}\frac{\partial^2}{\partial R^2}. \quad (3.44)$$

Taking the derivatives is straightforward:

$$\frac{\partial^2}{\partial r^2}e^{-\nu_c(\alpha_{bd}\mathbf{r}+\beta_{bd}\mathbf{R})^2}e^{-\lambda_c(\alpha'_{bd}\mathbf{r}+\beta'_{bd}\mathbf{R})^2} = (E+Fr^2+GR^2)e^{-\nu_c(\alpha_{bd}\mathbf{r}+\beta_{bd}\mathbf{R})^2}e^{-\lambda_c(\alpha'_{bd}\mathbf{r}+\beta'_{bd}\mathbf{R})^2}, \quad (3.45)$$

$$E = -6(\nu_c\alpha_{bd}^2 + \lambda_c\alpha_{bd}'^2), \quad (3.46)$$

$$F = 4(\nu_c\alpha_{bd}^2 + \lambda_c\alpha_{bd}'^2)^2, \quad (3.47)$$

$$G = 36(\nu_c\alpha_{bd}\beta_{bd} + \lambda_c\alpha'_{bd}\beta'_{bd})^2, \quad (3.48)$$

where terms proportional to $\mathbf{r}$ and $\mathbf{R}$ have been omitted because they will vanish in the integral. The derivative in R gives the same result with $\beta \leftrightarrow \alpha$. This means that to calculate the kinetic energy matrix element, one needs the matrix elements for

$$X(r,R) = 1, \quad (3.49)$$

which is the same as for the normalization matrix,

$$X(r,R) = r^2, \tag{3.50}$$

which is the same matrix element that needs to be solved to calculate the root mean square (rms) radius, and

$$X(r,R) = R^2, \tag{3.51}$$

which is the same as the matrix element for r^2 with $\beta \leftrightarrow \alpha$. This, together with the appropriate prefactors, will form the matrix element for the kinetic energy T.
So, only $X(r,R) = r^2$ has to be calculated ($X(r,R) = 1$ will be shown in Section 3.2.4):
Plugging this in in Eq. (3.41) and sorting the terms in the exponent one obtains

$$\left\langle a\right| r^2 \left|b\right\rangle = e^{-A} \int \mathrm{d}^3r \mathrm{d}^3R e^{-Br^2} e^{-CR^2} e^{-2D\mathbf{rR}} r^2, \tag{3.52}$$

$$A = 0, \tag{3.53}$$

$$B = \nu_{c'}\alpha_{ad}^2 + \lambda_{c'}\alpha_{ad}'^2 + \nu_c\alpha_{bd}^2 + \lambda_c\alpha_{bd}'^2, \tag{3.54}$$

$$C = \nu_{c'}\beta_{ad}^2 + \lambda_{c'}\beta_{ad}'^2 + \nu_c\beta_{bd}^2 + \lambda_c\beta_{bd}'^2, \tag{3.55}$$

$$D = \nu_{c'}\alpha_{ad}\beta_{ad} + \lambda_{c'}\alpha_{ad}'\beta_{ad}' + \nu_c\alpha_{bd}\beta_{bd} + \lambda_c\alpha_{bd}'\beta_{bd}'. \tag{3.56}$$

Integrating first over R, one can shift $\mathbf{R} \to \mathbf{R} - \frac{D}{C}\mathbf{r}$ and obtain

$$\left\langle a\right| r^2 \left|b\right\rangle = e^{-A} \left(\frac{\pi}{C}\right)^{\frac{3}{2}} \int \mathrm{d}^3r e^{-(B+\frac{D^2}{C})r^2} r^2. \tag{3.57}$$

Now the angles can be integrated out and the well-known Gaussian integral can be solved:

$$\left\langle a\right| r^2 \left|b\right\rangle = e^{-A} \left(\frac{\pi}{C}\right)^{\frac{3}{2}} \left(\frac{\pi}{B+\frac{D^2}{C}}\right)^{\frac{3}{2}} \frac{3}{2(B+\frac{D^2}{C})}. \tag{3.58}$$

So,

$$\begin{aligned}\langle a| T |b\rangle = &\left(-\frac{\hbar^2}{2\mu_r}E - \frac{\hbar^2}{2\mu_R}\tilde{E}\right) e^{-A} \left(\frac{\pi}{C}\right)^{\frac{3}{2}} \left(\frac{\pi}{B+\frac{D^2}{C}}\right)^{\frac{3}{2}} \\ &+ \left(-\frac{\hbar^2}{2\mu_r}F - \frac{\hbar^2}{2\mu_R}\tilde{G}\right) e^{-A} \left(\frac{\pi}{C}\right)^{\frac{3}{2}} \left(\frac{\pi}{B+\frac{D^2}{C}}\right)^{\frac{3}{2}} \frac{3}{2(B+\frac{D^2}{C})} \\ &+ \left(-\frac{\hbar^2}{2\mu_r}G - \frac{\hbar^2}{2\mu_R}\tilde{F}\right) e^{-A} \left(\frac{\pi}{B}\right)^{\frac{3}{2}} \left(\frac{\pi}{C+\frac{D^2}{B}}\right)^{\frac{3}{2}} \frac{3}{2(C+\frac{D^2}{B})}\end{aligned} \tag{3.59}$$

where advantage has been taken of the fact that $\left\langle a\right| R^2 \left|b\right\rangle$ is the same as $\left\langle a\right| r^2 \left|b\right\rangle$ with $B \leftrightarrow C$. $\tilde{E}$, $\tilde{F}$, and $\tilde{G}$ are the same as E, F, G with $\alpha \leftrightarrow \beta$.

Gaussian Potential Matrix

The Gaussian potential has the form

$$V_G(r) = V_0 e^{-ur^2}, \tag{3.60}$$

which can be easily plugged in in Eq. (3.41) and calculated. Sorting the terms in the exponent one obtains

$$\left\langle a\right| V_0 e^{-ur^2} \left|b\right\rangle = V_0 e^{-A} \int \mathrm{d}^3 r \mathrm{d}^3 R e^{-\tilde{B}r^2} e^{-CR^2} e^{-2D\mathbf{rR}}, \tag{3.61}$$

$$\tilde{B} = B + u. \tag{3.62}$$

Integrating over R first by shifting it as before ($\mathbf{R} \to \mathbf{R} - \frac{D}{C}\mathbf{r}$) and then solving the well-known Gaussian integral yields

$$\langle a| V_G(r) |b\rangle = V_0 e^{-A} \left(\frac{\pi}{C}\right)^{\frac{3}{2}} \left(\frac{\pi}{\tilde{B} + \frac{D^2}{C}}\right)^{\frac{3}{2}}. \tag{3.63}$$

Since in practice the interaction is between several particle pairs, this has to be summed over the appropriate r_{ij}. This can be achieved by picking the appropriate Jacobi coordinate configurations $\tilde{p}(c)$ in a given configuration channel and summing over $d \in \tilde{p}(c)$.

Gaussian Three-body Potential Matrix

Building the three-body potential is a bit more tricky, because it is

$$V_3(r_{ij}, r_{jk}, r_{ki}) = W_0 e^{-w(r_{ij}^2 + r_{ji}^2 + r_{ki}^2)}. \tag{3.64}$$

Using the properties of Jacobi coordinates, this can be rewritten as

$$V_3(r_d, r_e, r_f) = W_0 e^{-w(r_d^2 + r_e^2 + r_f^2)}, \tag{3.65}$$

with configurations d, e, f chosen appropriately to form a triangle. In the three-body case there is only one triangle that can be formed, but in the four-body case, a sum has to be taken over all possible triangles.
Like r_a and r_b, r_e and r_f can also be rewritten in terms of r_d using α_{ed}, β_{ed} etc., see Eq. (3.37). This yields the following integral that has to be solved:

$$\langle a| V_3(r) |b\rangle = W_0 e^{-A} \int \mathrm{d}^3 r \mathrm{d}^3 R e^{-B_3 r^2} e^{-C_3 R^2} e^{-2D_3 \mathbf{rR}}, \tag{3.66}$$

$$B_3 = B + w(1 + \alpha_{ed}^2 + \alpha_{fd}^2), \tag{3.67}$$

$$C_3 = C + w(\beta_{ed}^2 + \beta_{fd}^2), \tag{3.68}$$

$$D_3 = D + w(\alpha_{ed}\beta_{ed} + \alpha_{fd}\beta_{fd}). \tag{3.69}$$

This has the same form as Eq. (3.61), and therefore the solution is

$$\langle a| V_3(r) |b\rangle = W_0 e^{-A} \left(\frac{\pi}{C_3}\right)^{\frac{3}{2}} \left(\frac{\pi}{B_3 + \frac{D_3^2}{C_3}}\right)^{\frac{3}{2}}. \tag{3.70}$$

As already mentioned, in the four-body case this has to be summed over appropriate combinations of d, e, and f.

Coulomb Potential Matrix

Using the definition in Eq. (2.23), in this case

$$X(r, R) = \frac{c_c}{r}. \tag{3.71}$$

Plugging this in in Eq. (3.41) and sorting the terms in the exponent one obtains

$$c_c e^{-A} \int \mathrm{d}^3r \mathrm{d}^3R e^{-Br^2} e^{-CR^2} e^{-2D\mathbf{rR}} \frac{1}{r}. \tag{3.72}$$

For R, this is the same integral as before, which leads to

$$c_c e^{-A} \left(\frac{\pi}{C}\right)^{\frac{3}{2}} \int \mathrm{d}^3r e^{-(B-\frac{D^2}{C})r^2} \frac{1}{r}. \tag{3.73}$$

This is now spherically symmetrical again, so the angles can be integrated out. Using well-known formulae for Gaussian integrals, the resulting matrix element is

$$\langle a| V_c(r) |b\rangle = c_c e^{-A} \left(\frac{\pi}{C}\right)^{\frac{3}{2}} 4\pi \frac{1}{2(B-\frac{D^2}{C})}. \tag{3.74}$$

Of course, the note about having to sum over the appropiate Jacobi configurations in order to introduce interactions between all desired pairings that was made in Section 3.2.4 also applies here.

Root Mean Square Radius

To calculate the rms radius one has to calculate the following expression

$$r_{\mathrm{rms}} = \sqrt{\frac{1}{N_p} \sum_i^{N_p} \langle r_i^2 \rangle}, \tag{3.75}$$

where N_p is the number of pairs, i.e. the square root of the mean of all pair distances r_i squared. To achieve this the matrix element

$$\left\langle a \middle| r^2 \middle| b \right\rangle \tag{3.76}$$

is needed. This was already calculated in Section 3.2.4 and the result is (Eq. (3.58))

$$\left\langle a \middle| r^2 \middle| b \right\rangle = e^{-A} \left(\frac{\pi}{C}\right)^{\frac{3}{2}} \left(\frac{\pi}{B+\frac{D^2}{C}}\right)^{\frac{3}{2}} \frac{3}{2(B+\frac{D^2}{C})}. \tag{3.77}$$

These matrix elements can be used when the $C_{\tilde{n}}$ (see 3.33) have been found to calculate the rms radius using Eq. (3.75).

3.2.5 Implementation

I implemented a program for two-body systems that I used for all two-body calculations. For three- and four-body calculations I adapted code provided by E. Hiyama [114] for the different systems and interactions, because it is well-tested, fast and deals with numerical issues that might arise during calculations.

The input provided to the programs are the configuration channels, which are based on possible Jacobi coordinate configurations as discussed in Section 3.1. Depending on the number of particles and the number of distinct particles, there can be for example up to 18 different configuration channels in the four-body system, without considering angular momentum quantum numbers. Including these might increase the number further.

One important step when using the GEM is therefore to identify all configuration channels that contribute within the desired accuracy. Analysing which configuration channels produce the largest effects in turn can provide information about the structure of the calculated state.

Numerical Issues

A limitation is of course the matrix size which can become quite large with the GEM in comparison with other variational methods. This is because the strict geometrical spacing between consecutive basis states inevitably leads to the inclusion of "unneeded" basis states. On the other hand, the GEM gives a very good first estimate when physically sensible parameters are chosen.
The potentially large basis size can also lead to numerical problems of overcompleteness. These can usually be avoided by using slightly different parameters. Of course, this limits the number of configuration channels that can be incorporated in a calculation.
To discard overcomplete basis sets I set a deepest energy threshold , discarding all basis sets that lead to results below this threshold. The threshold is typically two or three times the expected energy to make sure no valid basis sets are discarded.
In addition, checking the behaviour of the state under slight variations of the potential depth also helps rule out overcomplete basis sets, which show jumping instead of smooth progression when the potential depth is varied.

Parameter Optimization

To find improved basis sets I wrote scripts in perl that start the programs with several randomly chosen parameters and then keep the parameters that give the lowest result for the energy (which, barring numerical issues is the most accurate estimate, see Section 3.2.1). This procedure can be done for the ground state and excited states, where care has to be taken that the lower states stay separated from the state of interest.
The workflow to optimize parameters for a specific state is therefore to first find good starting parameters by using physically motivated estimates about the size and shape of the state. "Good" starting parameters here means that the state is bound and the size of the state is reasonable. It is also advisable to start with a medium-sized basis, i.e. where computation time is relatively short while not any increase in the basis size gives a significant improvement in the energy.
For deep states it can be very easy to find a set of starting parameters. States that are close to some threshold are usually harder to find. If starting parameters cannot be found by simply guessing, it can help to start with a deeper or shallower potential (depending on how the state approaches the threshold), optimize there and use the optimized basis set as a starting point. Sometimes this has to be done in several steps, optimizing again at intermediate points. This approach has been used extensively in Section 4.3.
Once a starting parameter set is input in the optimization scripts, they will start the calculation with slightly varied parameter sets in parallel. Slightly varied means that one parameter (one of $n, r_{\min}, r_{\max}$ for one Jacobi coordinate in one configuration channel) at a time is changed within a predefined range, which was chosen to be very large to make sure nothing was omitted. The number of calculations that run in parallel depends on the available computing resources. For the trimer and dimer systems, the parallelisation was omitted because they run very fast.
When one of the calculations returns an energy that is lower than the lowest one to date, the parameter set will be set as the starting point for the next round of optimization. If there are several runs that return lower energy values, the lowest of these is chosen. Calculations that still run for more than two minutes after a lower energy candidate has been found are aborted.
This gives slight preference to smaller basis sizes, which run faster, and ensures that the optimization can go through as many rounds as possible in a limited time. It does not rule out that the basis size grows, but rather it tends to optimize at a fixed basis size until that does not yield significant improvements any more and then increase the basis size.
The optimization scripts check for numerical issues. They discard results that are below a predefined threshold, which can arise because an overcomplete basis set was chosen. They also check if the ground state is still there if optimizing the excited state (otherwise the ground and excited states

W_0/E_s	$\sqrt{E_3^0/E_s}$		$\sqrt{E_3^0/E_3^1}$	
	our result	[36]	our result	[36]
0.00	0.314347	0.314348	3.9341	3.9326
0.16	0.188463	0.188467	4.1225	4.1205
2.56	0.031410	0.031417	4.8955	4.8968
9.60	0.025999	0.026004	4.9023	4.9025

Table 3.1: Comparison of results from [63] with [36]. Shown are results for the mass ratio $M/m = 133/6$. The numbers were provided by D. Blume [115], and are shown in Fig. 2 of the supplement of [36]. In the first column the strength parameter of the three-body potential is listed in units of the natural energy scale E_s (Eq. (2.25)). The next two columns show the results for the trimer ground state energy in units of E_s. The last two columns show the ratio between the binding energies of the trimer ground and excited states. Table taken from [63].

might become mixed up). Of course, they also discard the run if an error is returned.
The scripts keep track of the improvements and send an alert when no improvements above a predefined threshold could be found for several rounds. This means that the result is converged.
One potential problem with this approach is that the local minimum the optimization finds might not be the global minimum. This can be mitigated by starting the optimization process from several different starting parameter sets and by checking the physical assumptions put into the starting parameter sets by comparing them with the outcome.

Cross-checking and Benchmarks

I checked my implementations of the potentials by comparing them to values available in the literature in [36, 43, 107].
In addition, it is also possible to compare the code for the N-body problem to the code for the corresponding $(N-1)$-body problem, by restricting the Nth particle to be very far away. This way it is possible to do for example three-body calculations with the four-body code and compare the two implementations.
For the Coulomb potential with a short-range Gaussian potential I also compared to results for the trimer provided to me by Artem Volosniev that were calculated with his Stochastic Variational Method (SVM) code. This was mainly to see whether higher partial waves, which are included in the SVM but only indirectly and partially included in the GEM as it was used here[1], made a significant contribution to the binding energy. Our results agreed within approximately one percent for the parameter sets we tested. Since this is more accurate than what is needed in the part that deals with the Coulomb force (Chapter 5), this was not pursued more rigorously.
I was also able to reproduce the value $-0.62\,\mathrm{MeV}$ from [107] for the trimer binding energy with the Ali-Bodmer potential (the sum of two Gaussians) and a Coulomb force to the precision given in their article. There, also the SVM was used, which also means that the higher partial wave contributions that are omitted in the GEM as used here do not play a big role. In addition to that, their value for the rms radius (2.64 fm) was also reproduced.
For the part that investigated the threshold behaviour of mass-imbalanced trimers and tetramers very close to the dimer + (2 atom) threshold (4.3), much higher accuracy is needed.
To benchmark the calculations, I tried to reproduce the results of Blume & Yan[36], which were provided with several significant digits. The results are shown in Table 3.1 and Table 3.2, which were

[1] It is possible to include higher partial waves explicitly in GEM calculations, but this was not done throughout this work.

W_0/E_s	$\sqrt{E_4^{0,0}/E_3^0}$		$\sqrt{E_4^{0,1}/E_3^0}$	
	our result	[36]	our result	[36]
0.00	1.89891	1.89890		
2.56	1.51452	1.51425	1.0119	1.0116
9.60	1.51121	1.51119	1.0110	1.0106

Table 3.2: Same as Table 3.1, but with the results for the four-body system in the form of ratios between the tetramer and the trimer ground state binding energies and between the binding energies of the excited tetramer and trimer ground state. Table taken from [63]. © 2017 American Physical Society

taken from [63]. The results shown are close to the unitary limit for the mass ratio $M/m = 133/6$. My own calculations were carried out at $|a|/r_0 \approx 10^{10}$.
As one can see in the Tables 3.1 and 3.2, the agreement is three digits or more, which is very good.

3.3 Gaussian Potentials

As described in Section 2.2 and Section 2.3, if one wants to calculate universal effects, it does not matter which potential is chosen as long as it reproduces the correct scattering length and three-body parameter.
Therefore, one is free to choose a potential with which it is easy to do calculations, like the Gaussian potential, and adjust it to produce the desired scattering length.
Examples of this approach in the literature can be easily found. Here, the same potential as in [43][36] has been used.
The two-body potential is

$$V(r_{ij}) = V_0 e^{-\frac{r_{ij}^2}{2r_0^2}}, \tag{3.78}$$

where r_{ij} is the distance between two particles and V_0 is a parameter governing the strength of the potential. The length scale r_0 is also a measure for the range of the potential.
Sometimes a three-body force is needed to move the whole spectrum up or down in energy. In this case

$$V_3(r_{ij}, r_{jk}, r_{ki}) = W_0 e^{-\frac{r_{ij}^2 + r_{jk}^2 + r_{ki}^2}{16 r_0^2}} \tag{3.79}$$

for $i \neq j \neq k \neq i$. W_0 is the strength of the three-body potential. The choice of the range parameter $\rho_0 = \sqrt{8} r_0$ is made for consistency with [36], but Gattobigio, Kievsky & Viviani showed that it does not make a large difference for the four-body states [43]. For three-body states, W_0 can be changed to fit them, so for a given three-body state there are many possible (W_0, ρ_0) pairs that reproduce the binding energy.
Both the two- and three-body potentials presented here are a standard approach in ultra-cold-atom physics when universal properties are of interest.
In nuclear physics, which is the focus of the second part of this thesis, the more standard approach is using the Ali-Bodmer potential, which correctly reproduces the α-α phase shifts.
However, since the focus is on universal properties, a phenomenological potential is not desirable. Instead, a Gaussian potential that correctly reproduces the α-α Coulomb modified s-wave scattering length is used together with the Coulomb potential. A goal of this investigation is to learn how much of the spectrum of α clusters could be explained by universal physics.

4 Mass-Imbalanced Systems

In this chapter, I will present the results obtained for the case of mixtures of two different atomic species with different masses. This has been investigated in part by Wang *et al.*[35] and Blume & Yan[36]. Wang *et al.* used the Born-Oppenheimer approximation and calculated for very large mass ratios. Blume & Yan used Gaussian potentials together with a correlated Gaussians method to study atom mixtures with experimentally relevant mass ratios in the unitary limit and near the three-body breakup threshold. The results here confirm and complement the results of Blume & Yan, and shed some light on claims made in [35].

I will refer to the heavier species with mass M as H and to the lighter species with mass m as L in the following. Due to the favourable scaling factor, systems of N heavy and one light atom have been calculated as illustrated in Fig. 4.1. In all calculations it is assumed that the interaction between unlike atoms is resonant or near-resonant, while the interaction between atoms of the same species is non-resonant and can be neglected. This assumption is generally sound, because for a resonant interaction, the scattering length has to be fine-tuned to a large value, and it is unlikely that two independent fine-tunings happen at the same time.

However, for some combinations of atom species, it is indeed the case that the intraspecies interaction is comparatively strong when the interspecies interaction is resonant. So, in order to fully compare the presented results with experiment, this would have to be considered in addition to finite-range effects.

The assumption of no interaction between like particles also means that there is no two-dimer threshold (as can be seen in Fig. 2.3), because two heavy particles cannot form a dimer without an interaction between them, so the only possible dimer in the system is a HL dimer. The results have been published in [62] and [63].

Figure 4.1: Illustration of the heteronuclear systems under investigation. The small black dot represents the light atom L of mass m and the big white circles the heavy atoms H of mass M. The lines connecting the atoms represent interaction; where there is no line, there is no interaction built into the Hamiltonian that was used.

4.1 Interaction

For the reasons outlined in Section 3.3, Gaussian potentials are used here to represent the interaction. Since there is only interaction between H and L particles and not among H particles, the potentials are not summed over all pairs:

$$V_G = \sum_{i<N} V_0 e^{-\frac{r_{iN}^2}{2r_0^2}}, \tag{4.1}$$

$$V_3 = \sum_{i\neq j<N} W_0 e^{-\frac{r_{ij}^2+r_{iN}^2+r_{jN}^2}{16r_0^2}}, \tag{4.2}$$

where r_{ij} is the distance between particles i and j, and the light particle L is the Nth particle. All other particles are heavy (H). This potential was also used by [36].
Using the (repulsive) three-body potential it is ensured that the energies stay in the universal window of $E \ll E_s$ (cf. Eq. (2.25)), which means that finite-range effects are negligible [36]. E_s here is

$$E_s = \frac{\hbar^2}{2\mu r_0^2}, \tag{4.3}$$

with μ the reduced mass of the HL-dimer. In practice, $E \leq 0.13E_s$ for all calculations in this chapter. This requires $W_0/E_s \approx 9.6$.
The full Hamiltonians solved here are

$$H_2 = -\frac{\hbar^2}{2\mu}\frac{\partial^2}{\partial r^2} + V_G, \tag{4.4}$$

$$H_3 = -\frac{\hbar^2}{2\mu_r}\nabla_r^2 - \frac{\hbar^2}{2\mu_R}\nabla_R^2 + V_G + V_3, \tag{4.5}$$

$$H_4 = -\frac{\hbar^2}{2\mu_r}\nabla_r^2 - \frac{\hbar^2}{2\mu_R}\nabla_R^2 - \frac{\hbar^2}{2\mu_\rho}\nabla_\rho^2 + V_G + V_3, \tag{4.6}$$

where $\mu_{r,R,\rho}$ are defined in Section 3.1.

4.2 Efimov Plot

To depict the behaviour of the Efimov trimers and the attached universal tetramers for different mass ratios, the Efimov plot is shown in Fig. 4.2. Since the behaviour of the Efimov trimers is well-known in these cases, the focus here is to show the tetramer behaviour.
In Fig. 4.2, the lowest Efimov trimer and the attached universal tetramer(s) are shown for two different mass ratios, $M/m = 133/6$ and $M/m = 7/6$. These correspond to mixtures of either ^{133}Cs or ^{7}Li with ^{6}Li, which are both accessible to experiments.
The units are chosen in such a way that the universal dimer aligns for both cases, i.e. the reduced mass of the HL dimer is chosen to be

$$\mu_{HL} = \frac{mM}{M+m} = 1. \tag{4.7}$$

To be able to rescale the plot without distorting it, the units H and ξ are introduced as

$$\frac{r_0}{a} = H\cos\xi \tag{4.8}$$

$$-\sqrt{\frac{|E|}{E_s}} = H\sin\xi, \tag{4.9}$$

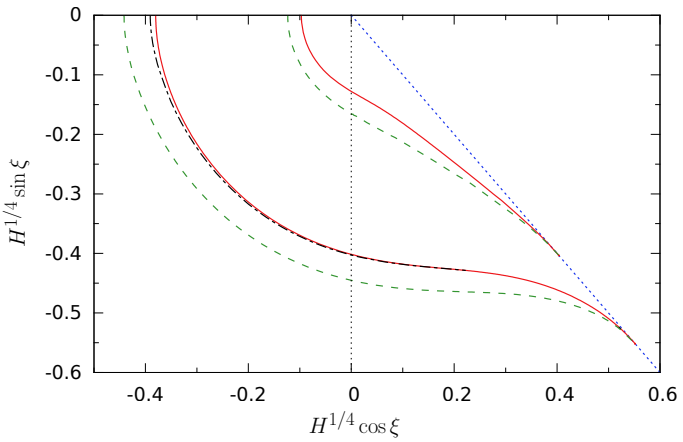

Figure 4.2: Lowest states in the Efimov plot of H_2L trimers and H_3L tetramers in a mixture of ^{133}Cs and ^{6}Li for the lower group of lines and ^{7}Li and ^{6}Li for the upper group of lines. The dashed blue line is the HL dimer for both cases and the red solid lines are the lowest Efimov trimer for each system. They represent the dimer + $2H$ threshold and the trimer + H threshold, respectively. The green long-dashed line is the tetramer ground state and the black dot-dashed line is the excited tetramer. The radial variable H has been rescaled by taking the fourth root. This makes the features at the tail end near the dimer threshold more visible. The calculated dimer threshold is replaced by the universal threshold and the difference to the dimer threshold is plotted on the positive scattering length side to make the two mass ratios more easily comparable, see text. This plot first appeared in [63]. © 2017 American Physical Society

where r_0 is the range of the Gaussian potential and therefore a measure for the interaction range, a is the HL scattering length, and E_s is the natural energy scale discussed in Eq. (2.25). These units have also been used in [51].
The dimer has been replaced by the universal dimer and the difference between the dimer and the trimer and tetramer states are plotted in the positive scattering length side of the plot, because the rescaling magnifies the small deviations of the dimer from the universal dimer and makes it more difficult to compare the two mass ratio cases.
As can be seen from Fig. 4.2, there are two tetramer states attached to the Efimov trimer for the high mass ratio, but only one tetramer for the low mass ratio. Also note that the excited tetramer vanishes for the higher mass ratio at some scattering length a_4^+ into the trimer + atom threshold. Calculations for other mass ratios, especially $M/m = 87/7$ which is not shown in Fig. 4.2 because it would overlap with the lines for $M/m = 133/6$, and comparison to the data for different mass ratios in the unitary limit from [36] suggest that $1/a_4^+$ becomes smaller and eventually negative for decreasing mass ratio until it vanishes completely.
The results are completely consistent with [36] as well as [58]. In the latter study, the ^{23}Na-^{87}Rb-system has been investigated, which corresponds to a mass ratio of about 3.8.
The values shown in the plot are all well within the window for universality, i.e. the conditions

$$E \ll E_s \quad \text{and} \quad r_0 \ll a \tag{4.10}$$

are fulfilled.
Another important thing to note is that the trimer and tetramer states seem to vanish at exactly the same point into the dimer threshold, which was not clear a priori. Wang *et al.* also found the same behaviour for the ^{23}Na-^{87}Rb mixture they studied [58]. This behaviour will be investigated more closely in the following section.
In addition, the slope of the curve for the ^{7}Li-^{6}Li mixture is much smaller than the slope of the ^{133}Cs-^{6}Li mixture. This behaviour persists when the three-body potential is changed to make the

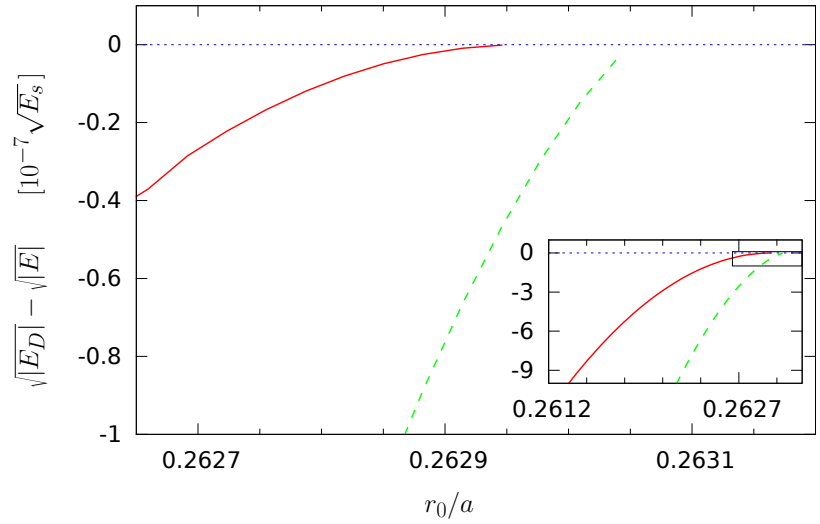

Figure 4.3: Binding energies of H_2L trimer (red solid line) and H_3L tetramer (green dashed line) relative to the HL dimer + $2H$ threshold, for the mass ratio of 133/6 corresponding to a ^{133}Cs-^{6}Li mixture. The dimer threshold is shown as a dotted blue line. The inset shows a larger region, and the large plot shows the portion of the inset that is marked by a black rectangle. A slightly modified version of this figure first appeared in [62]. Reprinted by permission from Springer Nature Customer Service Centre GmbH: Springer Nature, Few-Body Systems 58, 22, "Trimer and Tetramer Bound States in Heteronuclear Systems", C. H. Schmickler, H.-W. Hammer and E. Hiyama, © Springer-Verlag Wien 2016 (2017).

trimers for both mixtures vanish at the same point.

4.3 Behaviour Close to the HL Dimer Threshold

Here, the behaviour of the H_3L tetramer and the H_2L trimer close to the HL dimer + H atom threshold is studied. This is an interesting region for a number of reasons. Firstly, it is possible to directly investigate experimentally the scattering length for which the Efimov states and universal tetramers vanish because of loss features that are caused by this. Secondly there is a prediction that a special kind of Efimov trimers could form near the threshold. Braaten & Hammer argued that close to the dimer threshold, the dimer is much more deeply bound than the trimer and tetramer and thus can be regarded as one particle. It then follows that "effective Efimov trimers" consisting of a dimer + $2H$ should form, with a large scaling factor that corresponds to the mass ratio of the HL dimer and the H atom, because the atom-dimer scattering length becomes large at the threshold [51]. This will be explained in more detail in the next section. The behaviour of the tetramer near the dimer-atom-atom threshold has not been studied previously in a full four-body approach, except for the study [58], which investigated the spectrum for the specific case of a ^{23}Na-^{87}Rb mixture.

4.3.1 Trimer and Tetramer States

The calculations were carried out to very high precision in an effort to find a resolution at which a difference could be discerned between the point where the tetramer vanishes into the dimer threshold and the point where the trimer vanishes and to ascertain that the tetramer does not vanish through the trimer + atom threshold. The results can be seen in Figs. 4.3 to 4.5. The

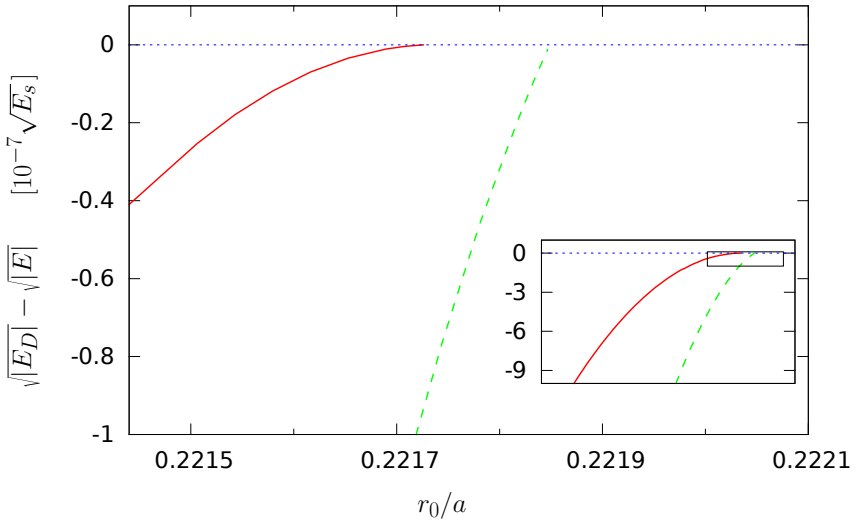

Figure 4.4: Binding energies of H_2L trimer (red solid line) and H_3L tetramer (green dashed line) relative to the HL dimer + $2H$ threshold, for the mass ratio of 87/7 corresponding to a ^{87}Rb-^{7}Li mixture. The dimer threshold is shown as a dotted blue line. The inset shows a larger region, and the large plot shows the portion of the inset that is marked by a black rectangle. A modified version of this figure first appeared in [63].

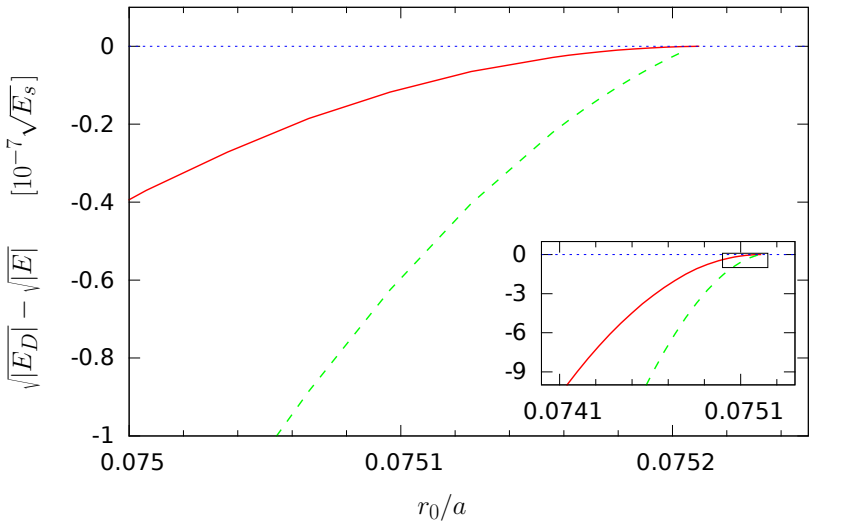

Figure 4.5: Binding energies of H_2L trimer (red solid line) and H_3L tetramer (green dashed line) relative to the HL dimer + $2H$ threshold, for the mass ratio of 7/6 corresponding to a ^{7}Li-^{6}Li mixture. The dimer threshold is shown as a dotted blue line. The inset shows a larger region, and the large plot shows the portion of the inset that is marked by a black rectangle. A slightly modified version of this figure first appeared in [62]. Reprinted by permission from Springer Nature Customer Service Centre GmbH: Springer Nature, Few-Body Systems 58, 22, "Trimer and Tetramer Bound States in Heteronuclear Systems", C. H. Schmickler, H.-W. Hammer and E. Hiyama, © Springer-Verlag Wien 2016 (2017).

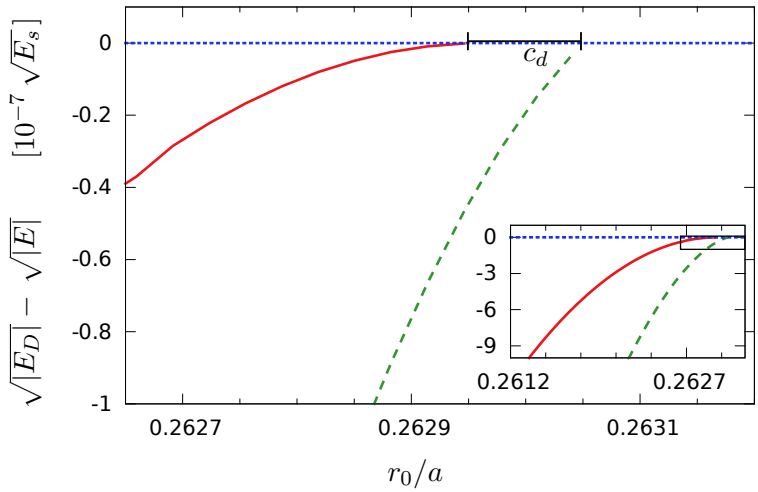

Figure 4.6: Demonstration of c_d for the example of mass ratio 133/6. For a description of the figure, see Fig. 4.3. The figure first appeared in [62]. Reprinted by permission from Springer Nature Customer Service Centre GmbH: Springer Nature, Few-Body Systems 58, 22, "Trimer and Tetramer Bound States in Heteronuclear Systems", C. H. Schmickler, H.-W. Hammer and E. Hiyama, © Springer-Verlag Wien 2016 (2017).

main conclusion that can be drawn here is that the trimer and tetramer states vanish at almost exactly the same point. Comparing the results for different mass ratios, one can see that the plots for the mass ratios $133/6 \approx 22$ (Fig. 4.3) and $87/7 \approx 12$ (Fig. 4.4) are very similar. This may also explain why they would overlap in Fig. 4.2. On the other hand, Fig. 4.5 is qualitatively different, because even at the high resolution that was chosen here, still no difference between the trimer and tetramer vanishing points can be seen.
To quantify the difference between the vanishing points, the methodology as demonstrated in Fig. 4.6 was used, i.e. a parameter c_d was defined as

$$c_d = c_4 - c_3, \tag{4.11}$$

where c_4 is the point on the r_0/a axis where the tetramer vanishes, and c_3 is the point on the r_0/a axis where the trimer vanishes. Errors were estimated for c_3 and c_4 by taking into account possible variations in slope near the threshold, based on the convergence of the calculated points and the distance to the threshold. The error for c_d is then calculated by error propagation.
The resulting c_d with error bars for different mass ratios is shown in Fig. 4.7. It can be observed that the relation is not linear. However, the error bars are quite large because of uncertainties in the extrapolation, so the functional dependency remains unclear. To understand these data points, an effective model was used to calculate the expected mass ratio dependence. For the model, it was assumed that the dimer is much more deeply bound than the trimer and tetramer and therefore can be regarded as a single particle. This makes it possible to use three-body calculations to solve this problem.
The EFT formalism from [34] was used to calculate a three-body system consisting of the dimer with mass $m + M$ and two heavy bosons of mass M.[1]
In line with the original system, an interaction was assumed only between the dimer and the bosons, and not between the bosons. The dimer inherits the interaction from the interaction between the light and heavy atoms. From the calculations one gets a functional dependency of c_d from the

[1]The code for this calculation was provided by the authors of [34], to whom I extend my thanks.

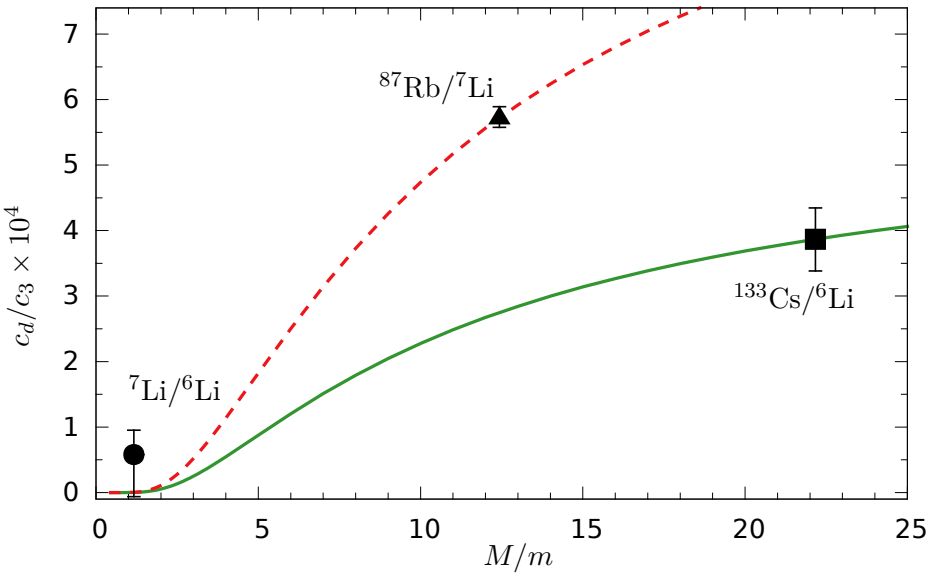

Figure 4.7: Difference c_d between the points where the trimer (c_3) and tetramer (c_4) vanish for different mass ratios, in units of r_0/a and normalised by c_3 in order to capture only relative effects. The points with error bars are extracted from Figs. 4.3 to 4.5 and the lines are from effective calculations of a three-body system with a HL dimer and two H atoms. The dashed line was fitted to reproduce the point for $M/m = 87/7$ and the solid line was fitted to reproduce the point for $M/m = 133/6$. The figure first appeared in [62]. Reprinted by permission from Springer Nature Customer Service Centre GmbH: Springer Nature, Few-Body Systems 58, 22, "Trimer and Tetramer Bound States in Heteronuclear Systems", C. H. Schmickler, H.-W. Hammer and E. Hiyama, © Springer-Verlag Wien 2016 (2017).

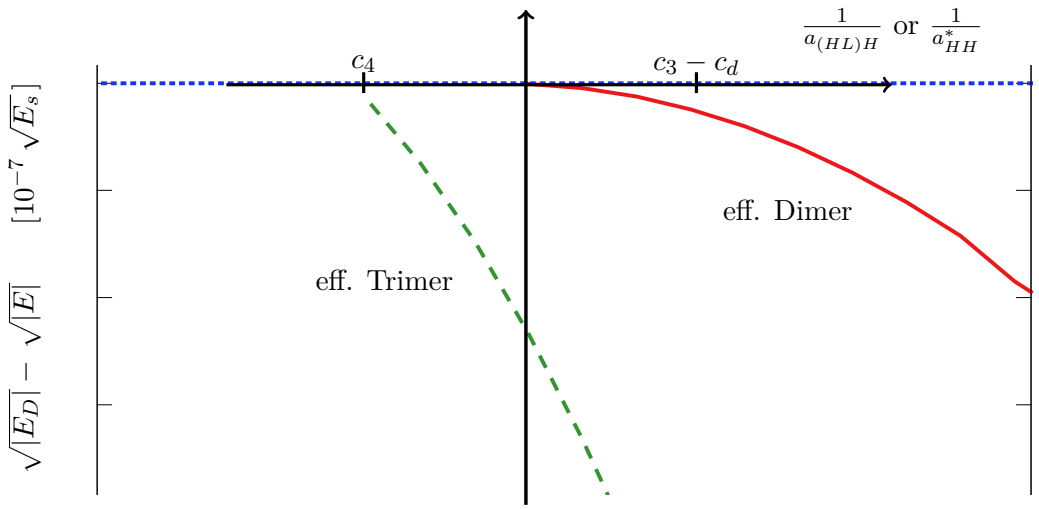

Figure 4.8: Illustration of the effective roles of the dimer, trimer and tetramer, by mirroring Fig. 4.3 and adding new labels. As explained in the text, the trimer (red line) becomes the effective $(HL)H$ dimer, and the tetramer becomes the effective $(HL)H_2$ trimer. The illustration is such that it can be easily compared to the Efimov plot (Fig. 2.2).

mass ratio M/m, but there is an undetermined free parameter, which is the three-body parameter. The two curves shown in Fig. 4.7 are thus fits of the three-body parameter to either reproduce the c_d value for $M/m = 87/7$ or for $M/m = 133/6$. Both curves show that c_d approaches zero as $M/m \to 0$ and has a small but non-zero value at $M = m$.
As can be seen, the fits result in different lines and it is difficult to argue that all points are represented by one fit without increasing the error bars. It should be noted, however, that the effective theory approach is strictly only valid for very large atom-dimer scattering length and therefore for $c_d \approx 0$. The atom-dimer scattering length at the point where the tetramer (or in the model, the $HL - H - H$ trimer) vanishes can be inferred from Eq. (2.26) as follows:

$$a_{HL-H} = \frac{\hbar}{\sqrt{2\mu B_{HL-H}}}. \tag{4.12}$$

Now, the dimer binding energy B_{HL-H} that should be input here is estimated by taking the length c_d, and subtracting it from c_3 (instead of adding it to get c_4). If one assumes the r_0/a_{HL-H} dependence from r_0/a to be approximately linear in a small range around c_3, r_0/a_{HL-H} at the point $c_3 - c_d$ should be the same value with the opposite sign as r_0/a_{HL-H} at the point c_4. Thus, if we take the value for B_{HL-H}, i.e. with respect to the HL dimer threshold, at the point $c_3 - c_d$, and input it to Eq. (4.12), we should get a rough estimate for the $HL - H$ scattering length at point c_4, by multiplying the result by -1. This is illustrated in Fig. 4.8.
For larger mass ratios the estimated atom-dimer scattering length was two orders of magnitude smaller than for the mass ratio 7/6, which means that the results should be more accurate for the smallest mass ratio.
Deltuva calculated similar values for the case of four identical bosons in [52]. He found $c_d/c_3 < 1.2 \times 10^{-6}$ for equal masses, whereas the value for $M/m = 7/6$ found here is $c_d/c_3 = 5.8 \times 10^{-5}$. Taking into account that the two different system are not directly comparable, these values are consistent. In the identical bosons case there are obviously interactions between all particles, while here the interactions are only between heavy and light atoms. This should however not have a very large effect, because while the atom-dimer interaction is resonant near c_3, the atom-atom interaction is not resonant away from the unitary limit, so close enough to c_3, it should be negligible.

In the effective three-body calculations at the point of equal masses, values between 10^{-8} and 10^{-7} were obtained for the three-body parameters that were used. Deltuva did effective three-body calculations with the same approximation used here as well and shows that the approximation is valid close to the dimer-atom-atom threshold [52].
However, since scattering lengths in all cases are quite large, it is more probable that either the error bars are underestimated, due to missing higher partial wave contributions or numerical problems that went undetected in spite of rigorous checks, or some important four-body physics is missing in the EFT description that would modify the mass ratio dependence. As will be discussed in the next section, there are different approximation schemes that lead to different effective three-body systems. This may point to missing four-body physics in one or both cases.

4.3.2 A Note on Precision

For the calculations shown in this section, optimization time has been much longer than for the results presented in Section 3.2.5, Tables 3.1 and 3.2 (about 20 times as long), and an approximately twice as large basis has been used. This ensures that the results here are converged to 8 digits, or a precision of $10^{-8}\sqrt{E_s}$, where E_s is the natural energy scale defined in Eq. (2.25).
In order to make sure that no important contributions are neglected, as many configurations as numerically possible were included in the calculations. As discussed earlier in Section 3.2, higher partial wave contributions are not fully contained in the Gaussian Expansion Method (GEM), because only a finite number of configurations and relative angular momenta can be included. However, they are also not expected to be important for the very shallow states near the threshold. The inclusion of relative angular momentum $L = 1$ and $\lambda = 1$ in the tetramer calculations, where L is the relative angular momentum between the dimer and the third particle (associated to Jacobi coordinate R) and λ is the relative angular momentum between the trimer and the fourth particle (associated to Jacobi coordinate ρ, compare Fig. 3.1), leads to a correction of the order of $10^{-7}E_s$. This is the configuration that is expected to contribute the most, so that including higher relative angular momenta should not contribute significantly at the accuracy that was reached.

4.4 Effective Efimov States of Dimer + $2H$ Atoms

As mentioned above, it has been predicted by Braaten & Hammer that near the dimer-atom-atom threshold there should be effective Efimov states that consist of the dimer plus two atoms. They argue that since the HL dimer is much more deeply bound than either the trimer or the tetramer, it could be regarded as one particle [51]. One then has the situation of a heavy particle (the dimer, with mass $M + m$) and two "light" bosons H, with mass M, near the point where the atom-dimer scattering length becomes large, which is the Efimov scenario. An intuitive argument for why the scattering length becomes large has been given in the last section. For more in-depth information on calculations of scattering lengths at various points in the Efimov spectrum, see [51].
Thus, the expectation is to find an effective $HL - H$ dimer, consisting of the HL dimer plus one H atom, which behaves like the universal dimer, and effective $HL - H - H$ Efimov trimers, consisting of the HL dimer plus two H atoms.

4.4.1 Expected Region of Occurence

This is expected to happen close to the region where the HHL trimer vanishes into the HL dimer threshold as illustrated in Fig. 4.10. Since the tetramer ground state also vanishes into the HL dimer threshold, it confines this region to above the tetramer state. This tetramer (or, in the effective three-body picture, the $HL - H - H$ trimer) can be seen as the lowest "effective Efimov" state, which however might be strongly influenced by finite range effects, as is often the case with

the lowest Efimov state. The size of the region where the "effective Efimov" effect may occur is therefore determined by c_d, which was already shown to be very small.
Since the interaction between the dimer and the atoms is inherited from the $H-L$ interaction and there is still no interaction between the H bosons, it is the same scenario as discussed in Section 4.2, only with a mass ratio less than 1. The expected scaling factor is therefore very large [51].
Deltuva studied this effect for four identical bosons [52]. He estimated the scaling factor to be 5×10^5 for the effective Efimov states [52]. This is in line with the prediction from [51].
However, one study that tackled this problem in the heteronuclear case for higher mass ratios ($M/m = 30$ and 50) using the Born-Oppenheimer approximation concluded that the scaling factor should be much smaller, around 20 [35]. They used the Born-Oppenheimer approximation to calculate the H_2L trimer as a two-body system and the H_3L tetramer and the $HL-H-H$ effective Efimov states as an effective three-body system. Wang *et al.* also checked some of their results with correlated Gaussian calculations [35].
They also included a sketch showing where the dimer-atom-atom Efimov states should appear. Compared to the results presented here, the c_d shown in this sketch is significantly larger. It can also be extracted from Fig. 2 of [35] and is

$$\frac{c_d}{c_3} \approx 0.03 \tag{4.13}$$

for $M/m = 30$. Extrapolating via the effective three-body calculations plotted in Fig. 4.7, the value should be around 10^{-3} to be consistent, which is significantly smaller than the value from [35]. So, while the sketch may only be misleading as it is a qualitative one, the scaling factors that were found are several orders of magnitude smaller than the estimate by Braaten & Hammer[51] and c_d/c_3 is much larger than in estimates based on the calculations presented here. Using the data from the previous calculations, I attempt to solve this puzzle.
There are a few possible reasons for the different results. One possibility is that c_d/c_3 depends on the potential between the H and L atoms and is not universal as was assumed here. This could be because while here, a Gaussian potential was used, in [35] Wang *et al.* used a Yamaguchi type separable potential [116].
To answer this question definitively, one would have to redo the calculations with a different potential. This may be an interesting question that could be answered in the future. One can however try to estimate whether non-universal effects should play a role, by observing the r_{eff}/a_{HL} dependence. If different results for different values of r_{eff}/a_{HL} were found that would be an indication that the effects are not universal.
For the calculations from [35] it is stated that $a_{HL} \gg r_{\text{ch}}$, where r_{ch} is a "characteristic two-body interaction range", is not well satisfied. It can be safely assumed that $r_{\text{ch}} \approx r_{\text{eff}}$, at least regarding the order of magnitude. Also, reading off c_d/c_3 for the excited and ground state trimers they show, it can be noted that they are both very similar, even though r_{eff}/a_{HL} is different in these cases. In the calculations carried out here, $r_0/a_{HL} \approx 1/4$ for the larger mass ratios $M/m = 87/7$ and $M/m = 133/6$, and $r_0/a_{HL} \approx 1/13$ for the small mass ratio $M/m = 7/6$. Typically $r_{\text{eff}} \approx 2r_0$ for the calculations here. c_d/c_3 is roughly of the same order of magnitude for all these cases. This means that in both cases the r_{eff}/a_{HL} dependence is small and therefore it is not very probable that non-universal effects are the issue here.
A second possibility is that using the Born-Oppenheimer (BO) approximation might be problematic near the dimer-atom-atom threshold and/or for this relatively small (for applications of the BO approximation) mass ratio. The scaling factor between (normal) Efimov states was calculated to be 5.5, which is almost 1.5 times the universal value 3.96 [51].
Following in this vein, the effective three-body calculations shown in the previous section also did not agree too well with the data. This might point to four-body physics that are missing in both effective three-body approaches.

Lastly, it is possible that for the effective three-body calculation used here, which is valid only in the region around $c_d/c_3 \approx 0$, the mass ratio $M/m = 30$ is too far away from the region of validity and therefore the extrapolation to this mass ratio using the effective three-body calculation should not be made. However, since $M/m \approx 12$ and $M/m \approx 22$ have datapoints and the atom-dimer scattering length $a_{(HL)H} \gtrsim 10^7 r_0$ for both points, the extrapolation to $M/m = 30$ should at least yield the correct order of magnitude.

4.4.2 Scaling Factor

As mentioned above, the effective Efimov trimer was predicted to be governed by the scaling factor for a system with one heavy and two light bosons, with no interaction between the light particles and a resonant interaction between the light and heavy particles [51].
This is illustrated in Fig. 4.9 a). Since the mass of the dimer is $M + m$ and the mass of the H bosons is M, the relevant mass ratio here is

$$\frac{M}{M+m} < 1. \tag{4.14}$$

This means that the scaling factor is very large,

$$\lambda > 1986.1, \tag{4.15}$$

which is the limit for $M/m \to \infty$ (and therefore $M/(M+m) \to 1$) [51].
However, a different picture emerged in [35] from the BO approximation. This competing picture is shown in Fig. 4.9 b). In the BO picture, the light atom L is mediating the interaction between the H bosons by moving between them. This means that in this picture, the light atom L is not bound to one of the H bosons thereby forming a dimer, but rather, it temporarily forms dimers with all the H bosons equally. This symmetric picture then leads to an interaction between all three H bosons with an associated effective scattering length a^*_{HH} which in turn leads to the Efimov scenario of three identical particles, which has a scaling factor of $\lambda \approx 22.7$ [35][51]. It was shown in [35] that a^*_{HH} diverges when the H_2L Efimov trimer becomes unbound, so it diverges at the same point as $a_{(HL)H}$.
The separation of scales in both pictures is the key difference here. While in the first picture the separation is between scales of binding energies with a deeply bound dimer and shallowly bound trimer and tetramer relative to the dimer, the BO picture separates the time scales of the heavy atoms and the light atom, which is assumed to move much faster than the heavy atoms. Then, the movement of the light atom is integrated out assuming stationary heavy atoms and becomes an effective interaction between the heavy atoms. Whether this separation is equally justified in the present case is unclear, because when the light atom is deeply bound to one heavy atom it is unclear whether its motion towards the other heavy atoms is on a shorter time-scale than the motion of the heavy atoms. This could mean that an interaction is only induced between two out of three pairs of heavy atoms because the light atom is localised on one of the heavy atoms.
The separation of energies on the other hand is clear since $|E_D|/|E_3^0 - E_D| > 300$ for the region shown in Fig. 4.3.
Another interpretation of the discrepancy is that the different pictures should be applied to slightly different scenarios. The BO picture from [35] does not assume a deeply bound dimer so it would be suitable for the situation where dimer and trimer are similarly shallowly bound. The picture brought forward by Braaten & Hammer on the other hand should apply in the situation where the dimer is very deeply bound and the trimer is very weakly bound with respect to the dimer.
Between these points, a transition is to be expected, going from a very large scaling factor in the infinitely-deep-dimer-case towards a much smaller scaling factor that was found in the BO case. For the region of interest here, this would mean that the scaling factor could be slightly smaller than predicted by Braaten & Hammer, because the dimer is not infinitely deep.

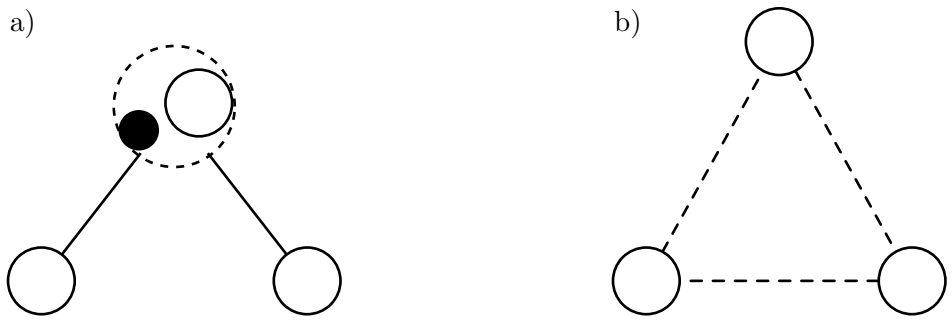

Figure 4.9: Two predicted dimer-atom-atom state scenarios. The prediction of [51] is illustrated in a), the prediction of [35] in b). The empty large circles are the H bosons and the black small circle the L atom. The solid lines denote the interaction between dimer and H boson that is inherited from the H-L-interaction. The dashed circle signifies that the dimer is to be treated as a single particle. The dashed lines denote the interaction between the H bosons that is mediated by the L atom.

Within the framework of the BO approximation, Wang *et al.* have found some evidence for an excited tetramer which is located at 14.3 times the a^*_{HH} scattering length where the ground state vanishes into the trimer+atom threshold on the positive a^*_{HH} scattering length side. On the negative a^*_{HH} scattering length side the scaling factor was found to be 19.3, which agrees reasonably well with their estimated scaling factor of 22.7, because the lowest tetramer state is not expected to be fully universal. However, this result was obtained from an effective three-body calculation using the BO approximation, so its validity depends on the validity of the BO approach in this case.
The calculations here yielded no excited tetramer at the precision that was possible to reach with the chosen method.
However, the results for the mass ratio $M/m = 133/6$ can be used to try to evaluate which one of these scenarios is correct. The largest mass ratio is best suited for this because in this case the scaling factor for the first scenario is favourable. In the second scenario, the scaling factor is predicted to be the same in principle for all mass ratios, but the BO approximation is valid only for large mass ratios, so of the ratios calculated it should also work best in the $M/m = 133/6$ case.
Assuming that the tetramer state that can be seen in Fig. 4.3 is the lowest of the presumed effective Efimov trimers it is possible to estimate where the next effective Efimov trimer should be with a specified scaling factor. This assumption was apparently also made in [35], even though it is not spelled out explicitly. To assess whether it should have appeared for the case of a small scaling factor of ≈ 20 as was proposed in [35] with the resolution that was reached, the tetramer was scaled accordingly in Fig. 4.10. This additionally assumes that the shape of the curve of the excited tetramer is similar to that of the ground state tetramer, which is a reasonable assumption when dealing with (suspected) Efimov states. As can be seen the estimated state is just in the energy region where the ground state tetramer ends, which corresponds to the resolution reached. Consequently, while it might be possible to find this state if it were there, it is so close to the resolution limit that not finding it does not exclude the existence of the state.
Finding states with an even larger scaling factor, especially if it is around 2000, is simply not possible within this approach.
Therefore, from the results presented here, a verdict on the existence and the scaling factor of the effective Efimov states cannot be made.

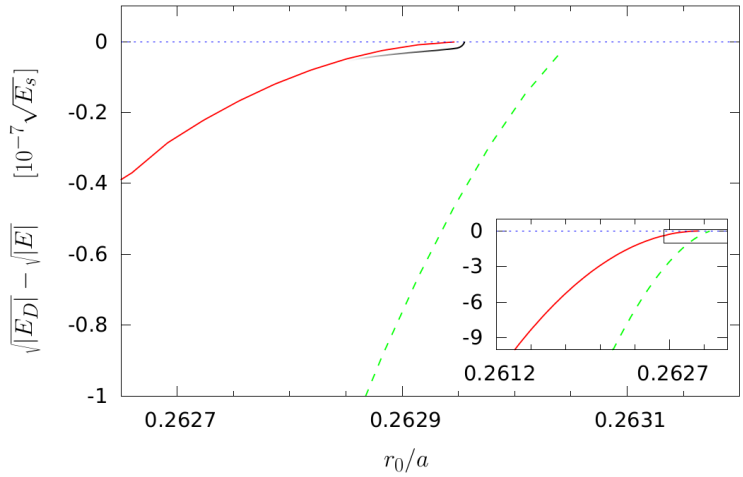

Figure 4.10: Fig. 4.3 with an estimate of where the next tetramer state should be according to [35], with a scaling factor of 20. The estimate is plotted as a black line. The calculations yielded no such state. For the prediction of [51] it would not be visible on this plot, as it would be much closer to the trimer (red line), where it vanishes into the dimer + atom + atom threshold (blue dotted line). As discussed in the text, finding a state with such a large scaling factor is not possible within the precision reached here. This figure first appeared in [63]. © 2017 American Physical Society

5 Universality and the Coulomb Force

In this chapter I will discuss how the Coulomb force affects the universal states, especially the universal dimer and the Efimov trimers.
This is an important question, because in many systems that have large scattering lengths between some or all of their constituents there is also the Coulomb force present, most importantly nuclear systems. The question of possible universal states in nuclear spectra has been in the focus of Efimov physics from the beginning [3]. But the long-range nature of the Coulomb interaction leads to complications that have long prevented an in-depth analysis of the interplay between universal effects and the Coulomb interaction.
Here, I present results divided into two categories. In the first category, the results are presented in terms of dimensionless quantities, which is achieved by dividing out natural values for those quantities. In the second category, results for specific systems are presented in terms of MeV and fm. These systems include ^{17}F, ^{12}C and ^{16}O. In these cases, subunits of the nucleus in question are regarded as particles, which makes it possible to treat these large systems (from the perspective of few-body physics) as two-, three- or four-body systems.

5.1 Natural Units

To calculate universal effects when a Coulomb interaction is present, a Gaussian potential, which is suitable to capture universal effects as discussed in Section 3.3, was combined with the Coulomb potential.
These kinds of potentials, i.e. a combination of short-range potentials with a Coulomb potential, are often used in nuclear physics in cluster models [17, 79, 117, 118] and to calculate interactions between charged polarons (quasi-particles) in solid-state physics [119–123].
The resulting two-body Hamiltonian is

$$H_2 = -\frac{\hbar^2}{2\mu}\frac{\partial^2}{\partial r^2} + V_0 e^{-\frac{r^2}{2r_0^2}} + \hbar c Z_1 Z_2 \frac{\alpha}{r} \tag{5.1}$$

with μ the effective mass, which is $\mu = \frac{m}{2}$ for identical particles, r the distance between the two particles, r_0 the width of the Gaussian potential and V_0 the depth, Z_1 and Z_2 the charge numbers of the particles, which are taken to be identical in the following, and $\alpha = \frac{1}{137}$ is the fine structure constant.
This Hamiltonian can easily be generalised to three- and four-body systems:

$$H_3 = -\frac{\hbar^2}{2\mu_r}\nabla_r^2 - \frac{\hbar^2}{2\mu_R}\nabla_R^2 + V_0 \sum_{i<j}^{3} e^{-\frac{r_{ij}^2}{2r_0^2}} + \hbar c \sum_{i<j}^{3} Z_i Z_j \frac{\alpha}{r_{ij}} \tag{5.2}$$

$$H_4 = -\frac{\hbar^2}{2\mu_r}\nabla_r^2 - \frac{\hbar^2}{2\mu_R}\nabla_R^2 - \frac{\hbar^2}{2\mu_\rho}\nabla_\rho^2 + V_0 \sum_{i<j}^{4} e^{-\frac{r_{ij}^2}{2r_0^2}} + \hbar c \sum_{i<j}^{4} Z_i Z_j \frac{\alpha}{r_{ij}} \tag{5.3}$$

Here, r_{ij} is the distance between particles i and j, and r, R and ρ are Jacobi coordinates as introduced in Fig. 3.1. The reduced masses μ_r, μ_R and μ_ρ are determined by the Jacobi coordinate set that is chosen, see Eqs. (3.14) to (3.17) and (3.19).
The only length scale included here is r_0, which can be used to derive a natural energy scale and a "natural charge" scale.
By dimensional analysis, the natural energy scale for identical particles of mass m is

$$E_s = \frac{\hbar^2}{m r_0^2}. \tag{5.4}$$

The Hamiltonian can then be divided by the natural energy scale E_s to derive the Hamiltonian in natural units $\tilde{H}$. For the two-body case this leads to

$$\tilde{H} = -\nabla_{\tilde{r}}^2 + \tilde{V}_0 e^{-\frac{\tilde{r}^2}{2}} + \frac{\tilde{c}}{\tilde{r}} \tag{5.5}$$

with

$$\tilde{r} = \frac{r}{r_0}, \tag{5.6}$$

$$\tilde{V}_0 = \frac{V_0}{E_s} \quad \text{and} \tag{5.7}$$

$$\tilde{c} = \frac{c_c}{c_s}, \text{ with } c_c = \hbar c Z_i Z_j \alpha \text{ and } c_s = \frac{\hbar^2}{m r_0}. \tag{5.8}$$

This can be extended trivially to the three- and four-body cases. With the Hamiltonian in this form, it is clear that $\tilde{c}$ is the relevant parameter when discussing the universal behaviour. The solution of the Schrödinger equation for two different r_0 will be the same functionally, i.e. except for scaling, if $\tilde{c}$ is the same in both cases. The parameter c_s is in this case a kind of natural strength of the Coulomb potential akin to the natural energy scale E_s. It gauges the Coulomb potential strength or barrier height against the depth and width of the Gaussian potential.
The charge of the particles can be expressed in terms of $\tilde{c}$ in order to connect this universal calculation back to physical systems:

$$Z_i Z_j = \tilde{c} \frac{\hbar}{c \alpha m r_0}. \tag{5.9}$$

In this expression r_0 is contained, which provides an easy way to see that universal scaling is broken with the inclusion of the Coulomb interaction unless the Coulomb interaction strength is scaled accordingly.
On the flip side of this expression, when trying to describe a physical system with specific charges of the particles, r_0 has to be chosen in order to determine $\tilde{c}$, which can then be used to do calculations. The problems that arise from this and the procedure that was chosen here will be discussed in the relevant section (Section 5.6).
First, however, the focus will be on results for different $\tilde{c}$ that can be seen as representing different universality classes which the universal scaling is broken into.

5.2 Generalised Efimov Plot

The term "Generalised Efimov Plot" was introduced in [65] to describe Efimov plots that do not have $\frac{1}{a}$ on the x-axis, but are plotted vs $\frac{1}{a_C}$ instead.
As discussed in the previous section, the Hamiltonian can be solved in natural units, which leads to the introduction of $\tilde{c}$, a dimensionless quantity that describes the strength of the Coulomb potential relative to a natural length scale which is dictated by the short-range potential.

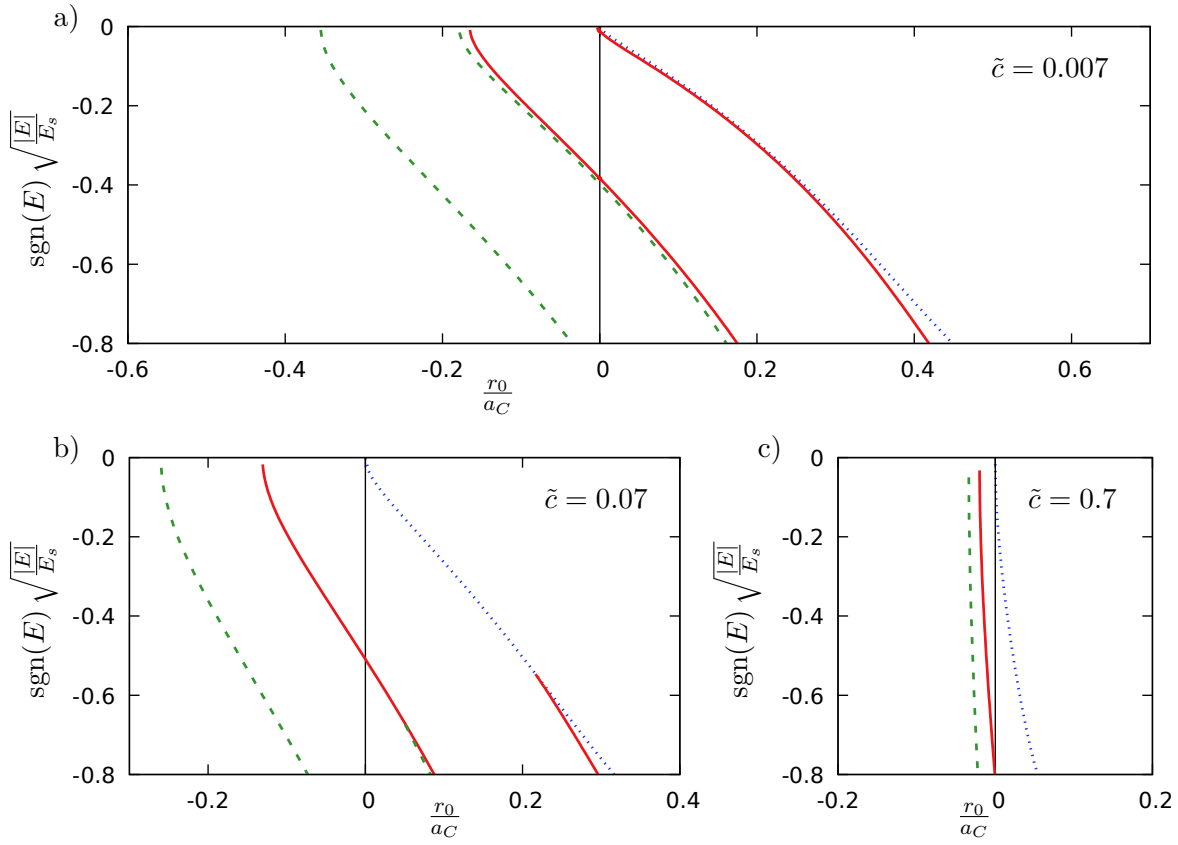

Figure 5.1: Generalised Efimov plots in natural units with different strengths of the Coulomb potential $\tilde{c}$. The dimer is shown by a dotted blue line, the trimer by solid red lines and the tetramers by dashed green lines. To make comparison between the plots easier, the scale on the x- and y-axes are the same in all plots. This figure was first published in [65]. © Società Italiana di Fisica / Springer-Verlag GmbH Germany, part of Springer Nature, 2019

Figure 5.1 shows the generalised Efimov plot for different values of $\tilde{c}$. The values were chosen to be inside the range accessible for calculations and such that they showed qualitatively different results. The region shown in Fig. 5.1 is the region where $|E| < E_s$, which is the maximum range where the effective theory that underlies the choice of the Gaussian potential is expected to hold. This is discussed in more detail in Section 2.2.

For relatively small values of $\tilde{c}$, the Efimov plot is almost unaltered. The Coulomb interaction only has a significant effect very close to the threshold, which leads to an increased slope of the curves near the threshold. This is noticeable when comparing the shape of the curve for the dimer in Fig. 5.1 a) to a straight line, which is the functional dependence for neutral particles.

It is also possible to see this in Fig. 5.2 when comparing the solid and the dashed lines.

This is the behaviour one would expect. Near the threshold the states are more dilute, as can be seen in Fig. 5.3, which means that the long-ranged Coulomb interaction will have more influence here. For more deeply-bound states, which are also smaller, the short-range interaction has a bigger influence.

As can be seen in Fig. 5.2, the energies of the states are pushed towards the threshold due to the Coulomb interaction, but near the threshold this effect becomes stronger.

Excited states are affected more by the Coulomb interaction as can be seen in Fig. 5.1 b). While they are still there in Fig. 5.1 a), in panel b) they have already almost vanished completely from

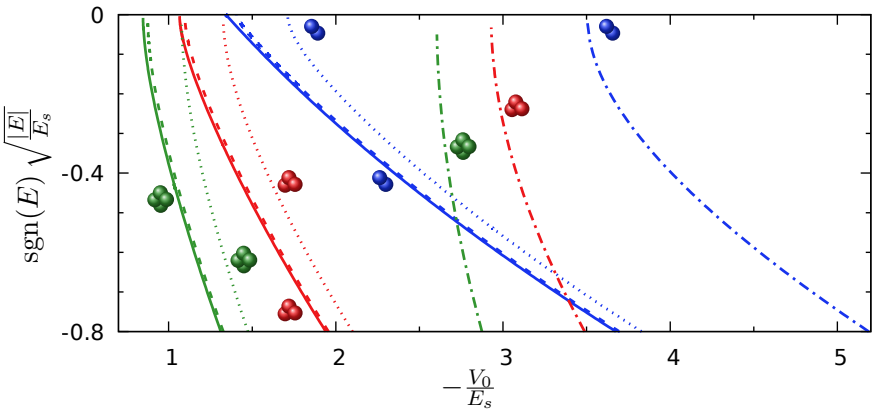

Figure 5.2: The Generalised Efimov Plot in terms of V_0 in order to show how the states are affected on an absolute scale. The solid lines are for the case without Coulomb interaction, the dashed lines are for $\tilde{c} = 0.007$, the dotted lines for $\tilde{c} = 0.07$ and the dash-dotted lines for $\tilde{c} = 0.7$. The blue lines represent the dimers, the red lines the trimer ground states and the green lines the tetramer ground states. To avoid confusion, excited states are not shown. This figure was first published in [65]. © Società Italiana di Fisica / Springer-Verlag GmbH Germany, part of Springer Nature, 2019

the region that is shown. Near the N-body breakup threshold they vanish first. This fits into the explanation because excited states are typically larger than ground states.
There is only one excited state discernible even in the case without Coulomb interaction, because the scaling factor in the identical boson case is very large ($\lambda = 22.7$).
One interesting feature to note here is that the tetramer excited state is more affected than the trimer excited state. This can be explained when reminding oneself that near the trimer+atom threhold or the dimer+atom threshold, excited states typically have the structure of a more deeply bound cluster (trimer or dimer) with the last particle only weakly bound to it and typically farther away. When the threshold is approached, this weakly bound particle detaches and becomes a free particle, leaving the cluster as a bound state.
If the particles involved are charged and repulse each other, there is effectively a particle with $Z_1 = 1$ and a cluster with charge $Z_2 = 2$ or 3, for the trimer and tetramer case, respectively. Thus, one would expect that the case with the higher charge is affected more by the presence of the Coulomb interaction than the state with less charges involved. This is exactly what can be observed in Fig. 5.1 b).
This is also corroborated by the root mean square (rms) radii calculated for different N, $\tilde{c}$ and binding energies, shown in Fig. 5.3. [1] There, the rms distance between two particles, $\sqrt{\langle r_{ij}^2 \rangle}$, is shown versus the binding energy relative to the N-particle breakup threshold. Since the particles are identical, which means that no pair can be singled out, the rms radius is averaged over all pairs and therefore represents a general size of the bound state.
The excited states (dashed lines) close to the point where they vanish can be seen becoming larger than their less charged and non-vanishing counterparts. Interesting to note here is that the trimer can sustain to become larger than the tetramer before it breaks up, because the effective Coulomb repulsion is less in this case.
Another interesting point to note here is that the ground state is generally smaller than the excited state at the same binding energies. This is due to the ground state not being fully universal. For any given binding energy it is farther away from unitarity than the corresponding excited state.

[1] For details on how the rms radius is calculated, see Section 3.2.4.

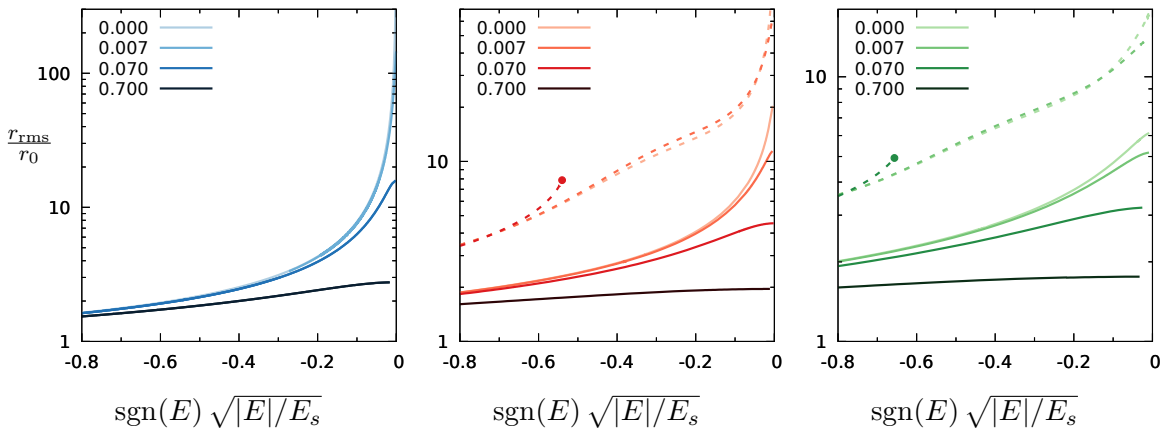

Figure 5.3: Rms radius r_{rms} in natural units for different strengths of the Coulomb potential $\tilde{c}$ versus the binding energy in natural units. The dimer is shown in the left panel, the trimer in the middle panel and the tetramer in the right panel. The legend notes the value of $\tilde{c}$. Solid lines represent the ground state while dashed lines represent the excited state. This figure was first published in [65]. © Società Italiana di Fisica / Springer-Verlag GmbH Germany, part of Springer Nature, 2019

In panel c) of Fig. 5.1 the trends described before continue. The excited states have completely vanished and the curves become increasingly steep and are being pushed closer together. After this, there is no qualitative change anymore. The steepness of the curves is also reflected in the rms radius calculations. As shown in Fig. 5.3 the rms radii for $\tilde{c} = 0.7$ stay almost constant while approaching the breakup threshold. The rms radius can be interpreted to be close to the maximum supported distance given the Coulomb interaction strength. Making the short-range interaction just slightly weaker which leads to a bigger rms radius makes the binding energy decrease rapidly because the balance is shifted towards the repulsive Coulomb interaction which does not decrease as much as the short-range interaction when the distance becomes larger.

5.3 Scaling Factors of the Three-Body States

To further assess how Efimov state characteristica are affected by the presence of the Coulomb force, I analysed the scaling factors that can be extracted from the generalised Efimov plots in Fig. 5.1.
There are two easy ways to calculate the scaling factor, which are dividing the square roots of the energies of the ground and excited states in the universal limit ($1/a_C = 0$), and dividing the $1/a_C$ where the energy becomes zero of the ground and excited states. This scattering length is usually called a^- in the literature. For clarity, I will call the ratio between energies

$$\lambda_E = \left.\frac{\sqrt{|E_3|}}{\sqrt{|E_3^*|}}\right|_{\frac{1}{a_C}=0} \tag{5.10}$$

and the ratio between scattering lengths

$$\lambda_a = \frac{a_C^{-*}}{a_C^-}, \tag{5.11}$$

where symbols with an asterisk pertain to the excited state and the others to the ground state.

$\tilde{c}$	λ_E	λ_a
0	23 ± 1	18 ± 1
0.007	32 ± 3	55 ± 5

Table 5.1: Ratios λ_E and λ_a as defined in the text for $\tilde{c} = 0$ and $\tilde{c} = 0.007$. For stronger Coulomb force there is no excited state any more and therefore also no ratios of this kind.

$\tilde{c}$	$a^- \sqrt{m\lvert E_3\rvert}/\hbar$	$a^{-*} \sqrt{m\lvert E_3^*\rvert}/\hbar$
0	2.1(1)	1.6(1)
0.007	2.3(1)	4(1)
0.07	4	-
0.7	40	-

Table 5.2: Values for the ratio of inverse scattering length and binding energy for the ground and excited states (where applicable) for different values of $\tilde{c}$.

These two ratios both give the scaling factor λ in the Efimov scenario, provided that the states are not affected by finite-range effects.
For the case without Coulomb, $\lambda_E = 23 \pm 1$ and $\lambda_a = 18 \pm 1$, which is reasonably close to the ideal case of $\lambda = 22.7$. The differences come from the fact that the ground state is too far away from the universal limit and therefore subject to finite range effects.
Comparing this now to the case with (weak) Coulomb, these ratios become much larger and more dissimilar, see Table 5.1. This means that the characteristical discrete scaling of Efimov states is disturbed very quickly, even for the weak-Coulomb case. When looking closely at the plots, one can see that this drastic change in the ratios λ_E and λ_a stem from a strong bending of the excited state curve near the three-particle breakup threshold. This is to be expected, because - as explained before - the states have the largest size close to the three-particle breakup threshold and this is where the Coulomb interaction is expected to play the largest role. The ground state is less affected, because it is more compact and therefore the short-range interaction is more important in this case.
Comparing the ratios for even stronger Coulomb interaction is not possible because the excited state does not exist any more close to the three-particle breakup threshold in that case.
One thing that can be compared, however, is the ratio between the binding energy in the unitary limit $|E_3|$ and the scattering length a_C^- for the corresponding state.
From the literature this value is known for identical bosons [124]:

$$a_n^- \sqrt{m|E_3^n|}/\hbar = -1.5077(1), \tag{5.12}$$

where the n refers to the nth excited state. Being closer to the unitary limit, the higher excited states are expected to approach the universal value that is presented in [124].
The results for the trimers shown in Fig. 5.1 are summarized in Table 5.2. The result without Coulomb for the excited state is consistent with the literature value Eq. (5.12). The ground state has a slightly larger ratio which is to be expected given that it is not very close to the unitary limit and therefore affected by finite range effects.
Comparing the values for $c_c = 0.007$ to the no-Coulomb case, it is interesting to note that the values for the ground states are almost the same, whereas the value for the excited state changes

$\tilde{c}$	$\frac{B_4^{0,n}}{B_3^n}$	$\frac{a_{4,n}^-}{a_{3,n}^-}$
0 ([45, 124])	4.610(1)	0.4254(2)
0	5.8(5)	0.43(1)
0.007	5.3(5)	0.45(3)
0.07	(4.4(4))	0.50(3)
0.7	(3.6(4))	0.59(4)

Table 5.3: Ratios between binding energies and scattering lengths extracted from Fig. 5.1 and Fig. 5.2 for different $\tilde{c}$ compared to literature values. Values in parentheses are outside the range where $|E| < E_s$.

significantly. This is further proof for the claim above that the changed scaling factors λ_E and λ_a are mostly due to the excited state changing.
Going to larger values of c_c, the ratio changes very drastically even for the ground state and is very far away from the universal number (Eq. (5.12)). This aspect of the Efimov states is therefore not very robust to adding a Coulomb force.

5.4 Scaling Factors of the Four-body States

In addition to the scaling factors pertaining to the three-body states, there are also universal factors that connect the tetramer and the trimer.
Deltuva [45, 124] calculated these values to be

$$\frac{B_4^{0,n}}{B_3^n} = 4.610(1) \quad \text{and} \tag{5.13}$$

$$\frac{a_{4,n}^-}{a_{3,n}^-} = 0.4254(2). \tag{5.14}$$

For the case without the Coulomb interaction the results for these values are 5.8±0.5 and 0.43±0.01, respectively. The ratio of the scattering lengths agrees very well, but the ratio of the binding energies does not. One has to keep in mind, however, that the binding energies are almost of the order of E_s in the unitary limit, so they are not expected to be fully universal any more.
Adding a weak Coulomb interaction decreases the ratio between the trimer and tetramer binding energies slightly, to 5.3(5). For stronger Coulomb interaction ($\tilde{c} = 0.07$), the tetramer binding energy is outside the range of validity of the underlying effective theory at unitarity. Extracting the value nevertheless yields 4.4(4), which is still rather close to the value for $\tilde{c} = 0.007$. For the strong Coulomb case, the factor becomes even smaller but still not too far off from the universal value. However, the same caveat applies as to the previous value, but more strongly, because the binding energy for the tetramer at unitarity in the strong Coulomb case is even farther away from the natural energy scale E_s.
This means that the tetramer is not very strongly affected by the presence of the Coulomb force, or more precisely that the tetramer is affected almost in the same way as the trimer. This is probably due to both the trimer and tetramer ground states having a similar size as can be seen in Fig. 5.3.
Comparing the ratios of the scattering lengths where the tetramer and trimer vanishes, respectively, the trend is similar, see Table 5.3. The ratio stays almost the same, and increases slightly. The slight increase is due to the tetramer becoming unbound at slightly larger scattering lengths, which agrees well with the analysis in Section 5.2.

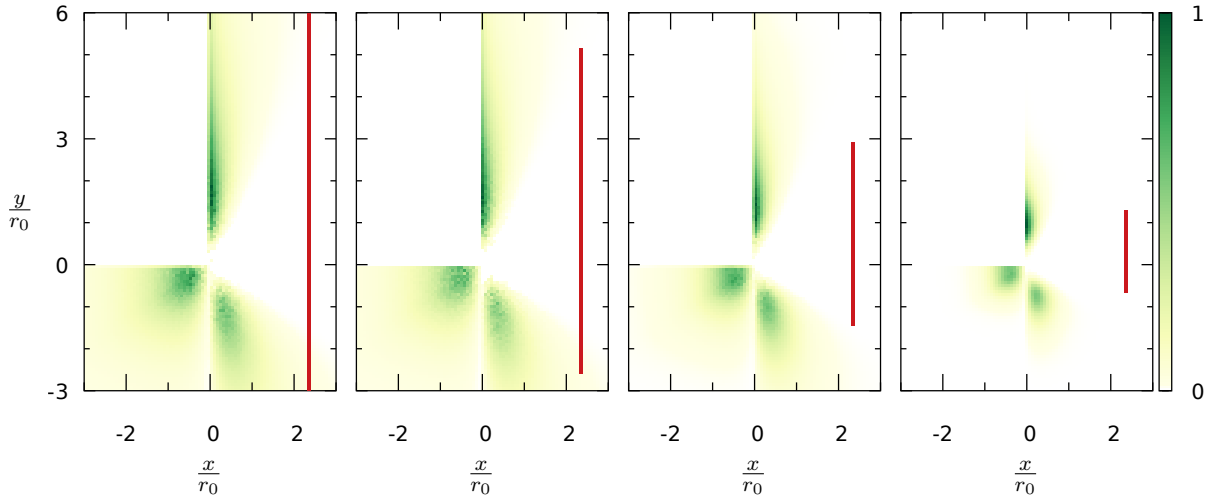

Figure 5.4: Contour plot of the ground state of the trimer at the binding energy $E_3 = 0.05E_s$ for different $\tilde{c}$ (from left to right $\tilde{c} = 0, 0.007, 0.07, 0.7$). It shows the probability distribution of the particles after ordering the configurations in space to bring out the structure. How this plot is produced is described in detail in Appendix C. The red bar shows the size of the rms radius for comparison. On each plot, the highest probability to find a particle is shown in dark green, while zero probability is shown in white. This plot was first published in [65]. © Società Italiana di Fisica / Springer-Verlag GmbH Germany, part of Springer Nature, 2019

However, the scaling between trimer and tetramer stays remarkably intact given that the plot in Fig. 5.1c) hardly resembles the Efimov plot any more.

5.5 Additional Remarks on the Structure of Three-Body States

In addition to explaining features of the generalised Efimov plot (Fig. 5.1), analysing the structure is interesting in its own right.
To this end I processed the wave functions such that the overall structure of the state became visible. This complements and helps understand the rms radius calculations that are presented in Fig. 5.3.
The steps involved in that process are described in detail in Appendix C.
The main steps are to

1. sample three particles at randomly generated positions,
2. calculate the probability of this configuration of particles using the wave function that is produced as a byproduct of the GEM calculations of the binding energies,
3. rotate and mirror this configuration in space to align similar configurations and expose probable shapes,
4. and repeat this process until a clear picture emerges.

The result from this process using wave functions of the ground state of the trimer for $\tilde{c} = 0, 0.007, 0.07$, and 0.7 at the point where the binding energy equals $0.05E_s$ is shown in Fig. 5.4. A fixed energy was chosen because the size and structure depends a lot on the energy as shown in

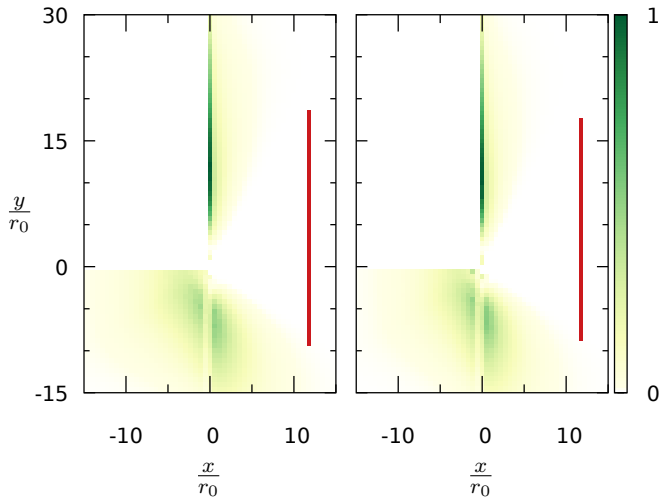

Figure 5.5: The same as Fig. 5.4, but for the excited state of the trimer, again at the binding energy $E_3^{(1)} = 0.05E_s$. Since there is no excited state near the threshold for $\tilde{c} = 0.07$ and $\tilde{c} = 0.7$, only $\tilde{c} = 0$ and $\tilde{c} = 0.007$ are shown (from left to right). This plot was first published in [65]. © Società Italiana di Fisica / Springer-Verlag GmbH Germany, part of Springer Nature, 2019

Fig. 5.3, so using a fixed energy is the best way to compare. Of course, this leads to different values of $1/a_C$ for each plot, but this has a minor effect compared to the binding energy. Additionally, a very small binding energy was chosen in order to have as little finite-range contributions as possible and in order to be able to observe the changes that take place close to the N-body breakup threshold.

For the excited state of the trimer, there are only figures for the case of $\tilde{c} = 0$ and 0.007, because for higher $\tilde{c}$ the excited state does not exist. The results for the excited state are shown in Fig. 5.5.

What can be seen on Fig. 5.4 is not only that the states become smaller as the Coulomb interaction strength becomes larger, which is expected and could also be discerned from the rms radius calculations. But it can in addition be seen that it is primarily the particle in the upper right quadrant, which moves closer to the other two particles, that is causing the shrinking rms radius.

In the case without Coulomb interaction, the ground state has a slightly elongated shape. This is expected for Efimov states, which were characterised in [74] as states with a diffuse geometry that favour configurations that resemble elongated triangles. For the ground state, which is expected to be distorted by finite-range effects, the shape is not as pronounced, but the diffuseness is still present.

As the Coulomb interaction is added and increased, the shape becomes less elongated and starts to resemble more an equilateral triangle, enlarging the deviation from the Efimov scenario.

In addition to that, the probability distribution of all particles becomes more concentrated in one point and less diffuse compared with the distribution without the Coulomb interaction. Thereby the states lose the other structural Efimov characteristic.

The excited state (Fig. 5.5) is a much more pronounced elongated triangle. The two particles on the lower half of the plot are very close together.

As can be seen in Fig. 5.5, adding a weak Coulomb interaction does not disturb the Efimov state structural characteristics described above.

This was also investigated in the context of the Hoyle state by Fedorov *et al.*[82]. They used the Ali-Bodmer potential together with a three-body force and found an equilateral triangle configuration

for the ground state of ^{12}C and a more dilute and elongated one for the Hoyle state. So they found a very similar result for a different potential which points to the universality of the results presented here.
Another widely used criterion for Efimov states is that the size of the trimer should be much larger than the interaction range[76]. As an estimate for the short-range interaction range, one can take r_0. Then it is easy to see in Fig. 5.3 that the rms radius is pushed closer to r_0 for increasing Coulomb interaction strength and therefore out of the universal region where $r_{\mathrm{rms}} \gg r_0$.
For $\tilde{c} = 0.007$ this criterion is still fullfilled quite well as can be seen in Fig. 5.3, but for stronger Coulomb interaction it breaks down.
To summarize, it can be said that while adding a weak Coulomb interaction does not disturb the key characteristics of Efimov states much, the addition of a strong Coulomb interaction, comparable for example to α particles, destroys those characteristics, at least in the bound state sector, that is accessible here.

5.6 Application to Nuclear Physics

In order to assess whether universal effects can be seen in nuclear systems the results presented will be transferred to ^{17}F and ^{16}O in the following section.
However, as mentioned before, there is some ambiguity due to the two competing scales of r_0 and c_c. The formula for calculating the charge from $\tilde{c}$ and r_0 (Eq. (5.9)) can be reversed to give

$$\tilde{c} = Z_i Z_j \alpha m r_0 \frac{c}{\hbar} = \frac{c_c}{c_s}. \tag{5.15}$$

This means that there will be different $\tilde{c}$ possible for the same charge and mass of particles, as long as r_0 is not fixed.
However, $\tilde{c}$ is the parameter that determines how strongly a system is affected by the Coulomb interaction as shown in the previous sections.
To solve this problem, r_0 has to be determined. To this end, there are two obvious ways of determining r_0.
In the spirit of the effective range expansion (Eq. (2.15)), one could argue that one has to go to the next order and not only fix the scattering length to the one that is observed for the particles in question (for example the $\alpha\alpha$ scattering length $a_{\alpha\alpha} \approx 1920\,\mathrm{fm}$ [80], which was determined from scattering data from [125] compiled in [126] and a measurement of the ^{8}Be ground state from [127]), but also the effective range.
Another approach would be to eliminate r_0 by going to the zero-range limit. Using a zero-range potential that produced the correct scattering length is a standard approach of universal physics[7, 128–130] and widely used in nuclear [17, 19, 131–133] and atomic physics[25, 50, 51, 58, 74, 90, 134, 135].
In the context of the applications proposed here, if done naively it might yield worse results than the other approach, because the approach of fixing r_0 involves more data input which will probably lead to the indirect inclusion of finite-range effects to some extent. Finite-range effects are expected to have more effects in charged systems, because the Coulomb barrier forces the particles to spend more time inside the short-range potential [136]. Nevertheless, the zero-range approach might also prove to be an interesting starting point for investigating realistic few-body systems of charged particles.
However, Volosniev has suggested in [66] that one finite-range parameter can be introduced to account for finite-range corrections to the binding energy. He proves this analytically for shallow two-body bound states. For three- and four-body systems I provided numerical calculations which were also published in [66].

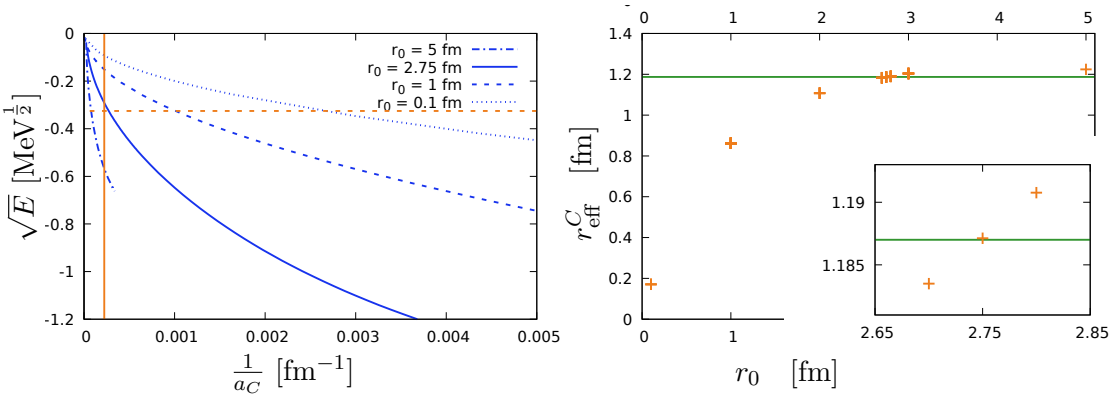

Figure 5.6: Plots for the ^{17}F system. *Left panel:* Efimov plot in physical units with different ranges r_0 of the Gaussian potential (see legend). Only the dimer is shown (blue lines). The physical value of the ^{16}O-p scattering length is shown as a vertical orange line, and the binding energy of the excited state ^{17}F ($\frac{1}{2}^+$) is shown as a horizontal dashed orange line. *Right panel:* The Coulomb-modified effective range as a function of r_0 for fixed scattering length. The physical value is shown as a horizontal green line. The inset shows the region close to the physical value. This figure was first published in [64]. Reprinted by permission from Springer Nature Customer Service Centre GmbH: Springer, Cham, Universality and the Coulomb Interaction. In: Orr N., Ploszajczak M., Marqués F., Carbonell J. (eds) Recent Progress in Few-Body Physics. FB22 2018. Springer Proceedings in Physics, vol 238. by C. H. Schmickler © Springer Nature Switzerland AG 2020 (2020).

In the following I will first present results for the first approach of fixing r_0. The example systems used are the first excited state of ^{17}F calculated as a dimer consisting of ^{16}O + p, and the $N\alpha^2$ system in the bound state sector. The results shown were first presented in [64] for ^{17}F and [65] for $N\alpha$.
Then I will briefly discuss going to the zero-range limit and show results which were first shown in [66].

5.6.1 ^{17}F as a Dimer

As mentioned before, in this section the method of fixing the range of the short-range Gaussian potential r_0 such that the Coulomb-modified effective range r_{eff}^C is reproduced is applied to the first excited state of ^{17}F, which is ^{17}F($\frac{1}{2}^+$). This is a well-known proton halo nucleus[79, 118], so it should be possible to describe it within the theory developed here as dimer of a proton and the ^{16}O core.
Values for the proton-^{16}O Coulomb-modified scattering length a_{Op}^C and the effective range were extracted from [79] using the formulae derived there and plugging in the binding momentum $\gamma = 13.6\,\text{MeV}$ and the asymptotic normalization coefficient (ANC) $A \approx 80\,\text{fm}^{-\frac{1}{2}}$:

$$a_{Op}^C = 4476\,\text{fm} \tag{5.16}$$
$$r_{\text{eff}}^C = 1.187\,\text{fm}. \tag{5.17}$$

To illustrate the point that r_0 has to be fixed, curves for different r_0 are shown in the left panel of Fig. 5.6. There, $Z_1 = 1$, $Z_2 = 8$ and $\mu = 873\,\text{MeV}$ have been plugged in, and the location of the ^{17}F($\frac{1}{2}^+$) state in question is marked by a vertical line where the scattering length has the physical value a_{Op}^C.

[2]The N here stands for 2, 3, or 4, not for "nucleon".

It is easy to see that different r_0 give wildly different results for the binding energy of $^{17}\mathrm{F}(\frac{1}{2}^+)$ relative to the $^{16}\mathrm{O}$ + p threshold, which can be read off from the left panel of Fig. 5.6 at the intersection of the dimer curve with the vertical line representing the physical scattering length a_{Op}^C.
To resolve this ambiguity, r_0 is chosen in such a way as to reproduce the physical effective range r_{eff}^C. Following the description in Section 2.1.2, the Coulomb-modified effective range was calculated for different r_0 with the condition that the scattering length be within 80 fm of the physical scattering length. This condition was chosen such that the value for a^C within that interval would not have a larger effect on r_{eff}^C than the aimed-for precision of r_0.
The result is shown in the right panel of Fig. 5.6. The green horizontal line shows the physical value $r_{\mathrm{eff}}^C = 1.187\,\mathrm{fm}$. Since r_{eff}^C rises monotonically with r_0, r_0 can be uniquely determined. The value for r_0 that was extracted from this is 2.75 fm.
Using this value for r_0 reproduces the binding energy of $^{17}\mathrm{F}(\frac{1}{2}^+)$ well, as can be seen in the left panel of Fig. 5.6.
One might argue that since the binding momentum and the ANC was used as an input to compute a_{Op}^C and r_{eff}^C, this is only a consistency check. However, the method (Halo effective field theory (EFT)) used in [79] to connect these values with the binding energy is different from what is used here and as such it is irrelevant where the values for a_{Op}^C and r_{eff}^C came from. Some of the underlying ideas are however similar in Halo EFT and the Hamiltonian used here, so the results are not completely independent.

5.6.2 $N\alpha$ System

The $N\alpha$ system has sparked a lot of interest, because of its simplicity and symmetry, and also due to the central role of $^8\mathrm{Be}$, $^{12}\mathrm{C}$ and $^{16}\mathrm{O}$ in the formation of elements inside stars[86–88, 137, 138]. The ground states of these systems are 0^+ states which makes it conceivable that they could be described as clusters of α particles. $^{12}\mathrm{C}$ and $^{16}\mathrm{O}$ are however very tightly bound, so that the ground state contains significant contributions from more compact configurations.
For excited 0^+ states, especially those near the $N\alpha$ breakup threshold or above it, the α cluster contribution might become dominant.
For the calculations, which follow the same procedure as for $^{17}\mathrm{F}$, we used the Coulomb-modified $\alpha - \alpha$ scattering length and effective range from [80]:

$$a_{\alpha\alpha} = (-1920 \pm 90)\,\mathrm{fm} \tag{5.18}$$

$$r_{\mathrm{eff}} = (1.098 \pm 0.005)\,\mathrm{fm} \tag{5.19}$$

In Fig. 5.7 the r_{eff} resulting from calculations with $Z_1 = Z_2 = 2$, $\frac{\hbar^2}{2\mu} = 10.525\,\mathrm{MeVfm}^2$ (from [139]) and different r_0 are presented. Only results for which the scattering length[3] was calculated to be within the error margin in Eq. (5.18) are shown.
In this case, $r_0 = 2.3\,\mathrm{fm}$. For comparison with the calculations in Section 5.2, $\tilde{c} = 1.27$ with this value for r_0. Using this value to calculate the dimer, trimer and tetramer consisting of α particles reveals that the results do not immediately fit with the physical states in this region. It can be seen in the left panel of Fig. 5.8 that the ground state of $^{12}\mathrm{C}$ is below E_s, the natural energy scale associated with r_0. This means that this state is not accessible with this approach.
There is a three-body state for the physical scattering length $a_{\alpha\alpha}$ which is much closer to the $N\alpha$ breakup threshold than the ground state of $^{12}\mathrm{C}$. This points to a three-body force being needed to accurately represent the physics. Introducing a three-body force is a standard procedure and has been found to be necessary in many cases [51].

[3] The scattering length in these calculations is a function of the range and depth of the Gaussian potential, r_0 and V_0, and c_c, the strength of the Coulomb potential as defined in Eq. (2.23)

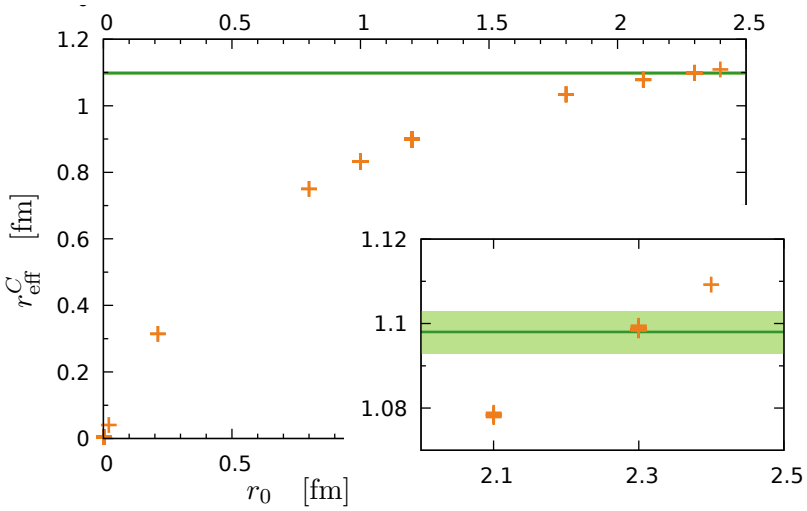

Figure 5.7: The same figure as the right panel of Fig. 5.6 for the $N\alpha$ system. The physical value of the Coulomb-modified effective range is shown as a green line with an error band (values from [80]). The points shown are for the $a_{\alpha\alpha}$ within the error band quoted in Eq. (5.18). This figure first appeared in [65]. © Società Italiana di Fisica / Springer-Verlag GmbH Germany, part of Springer Nature, 2019

Here, the following three-body force is used (compare Eq. (3.79) and Eq. (4.2)):

$$V_3 = W_0 \sum_{i\neq j\neq k\neq i}^{N} e^{\frac{r_{ij}^2+r_{jk}^2+r_{ki}^2}{16r_0^2}} . \tag{5.20}$$

What is interesting is that even with a three-body force, the bound states or absence thereof cannot be accurately represented within this approach. This is illustrated in the middle and right panel of Fig. 5.8: In the right panel it can be seen that adding a three-body force strong enough to eliminate the trimer also eliminates the tetramer.

There is however a tetramer in the accessible region between E_s and the $N\alpha$ breakup threshold. It is an excited state of ^{16}O, usually referred to as $^{16}\mathrm{O}\ (0_5^+)$, which lies at 14032 keV above the ground state according to [140], which translates to approximately 0.4 MeV below the four-α breakup threshold. It is included in Fig. 5.8 with its width indicated as a shaded band. Since this state is in the accessible region, near the $N\alpha$ threshold and has the appropriate quantum numbers, it is not unreasonable to expect that it should be possible to describe it within the chosen approach at least in first approximation.

So the fact that it does not appear at all is a puzzle. When fitting the three-body force such that the tetramer is reproduced, as shown in the middle panel of Fig. 5.8, there is also a trimer, which does not exist in nature.

This might point to the approach not being valid any more for such high $\tilde{c}$, or to a four-body force being needed. It could also mean that the short-range non-α-cluster contributions to this state are much larger than anticipated.

The rms radius for the tetramer without three-body force at the $\alpha\alpha$ scattering length is only 3.1 fm, not much larger than $r_0 = 2.3$ fm. This is not substantially changed by adding a three-body force: $r_{\rm rms} = 3.4$ fm in the case of a three-body force that reproduces the $^{16}\mathrm{O}\ (0_5^+)$ binding energy, corresponding to the middle panel in Fig. 5.8. At such a small size, large short-range contributions are to be expected and might explain the discrepancy between experiment and universal description.

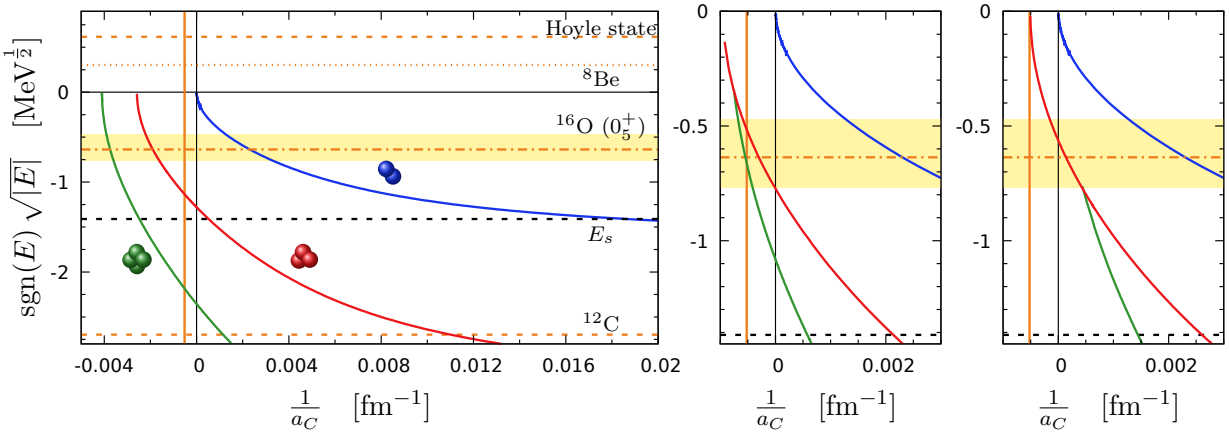

Figure 5.8: *Left panel:* Results for the $N\alpha$ system as plot of the square root of the binding energy versus the inverse of the Coulomb-modified scattering length, with the dimer shown in blue, the trimer in red and the tetramer in green. Selected 0^+ states of the $N\alpha$ system are shown as horizontal lines, with values taken from [140–142]. The width, if visible, is shown as a band. *Middle panel:* Zoomed-in version of the left panel, with a three-body force tuned such that the tetramer reproduces the shallowest ^{16}O 0^+ state with respect to the 4α breakup threshold. *Right panel:* Zoomed-in version of the left panel, with a three-body force tuned such that the trimer is unbound at the physical α-α scattering length. This figure has first been published in [65]. © Società Italiana di Fisica / Springer-Verlag GmbH Germany, part of Springer Nature, 2019

Further investigation is needed to definitively solve this. Calculating resonance states such as the Hoyle state or the ^{8}Be ground state might help in this endeavour.

5.6.3 Zero-Range Limit

Since fixing the range of the Gaussian potential, r_0, such that the effective range is reproduced leads to unsatisfactory results, the alternative way of eliminating r_0 by letting it go to zero will be explored in the following.

Dimer

Focussing on the two-body system first, Volosniev derived an identity for the relation between the scattering length and the binding energy [66] in the zero-range limit (as an analogue to Eq. (2.26)):

$$2\eta\frac{\Gamma'(\eta)}{\Gamma(\eta)} - 2\eta\ln(\eta) + 1 = -\frac{1}{\kappa a_C}, \tag{5.21}$$

where η is the Sommerfeld parameter as defined in Eq. (2.17), but now for negative energy:

$$\eta = \frac{\mu c}{\hbar} Z_1 Z_2 \frac{\alpha}{\kappa}, \tag{5.22}$$

$\kappa = ik$ is the wave number connected to the binding energy as in Eq. (2.6):

$$E = -\frac{\hbar^2\kappa^2}{2\mu}, \tag{5.23}$$

and $\Gamma(\eta)$ is the gamma function. This relation (Eq. (5.21)) is shown in Fig. 5.9b), together with the results for the Gaussian range $r_0 = 1\,\mathrm{fm}$ (cyan circles) and $r_0 = 0.0002\,\mathrm{fm}$ (dark-cyan triangles).

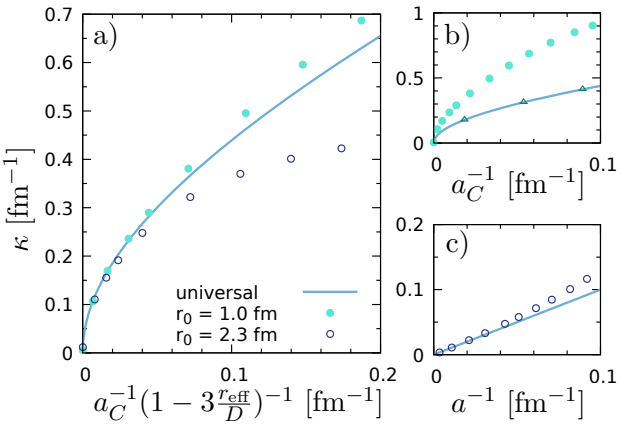

Figure 5.9: Zero-range limit of the dimer binding wave number versus the inverse scattering length. The universal limit is shown as a solid curve. The mass and charge are those of α particles. *Panel a):* κ as function of the rescaled scattering length as discussed in the text. The results for finite r_0 are shown as points with values for r_0 given in the legend. *Panel b):* The same as panel a), without the rescaling, and with additional points for $r_0 = 0.0002\,\mathrm{fm}$ shown as dark-cyan triangles. *Panel c):* The case without Coulomb as a comparison, while all other parameters are the same. This figure was adapted from [66] (published under CC-BY 4.0 [143]) by adjusting notation and adding points in panel b).

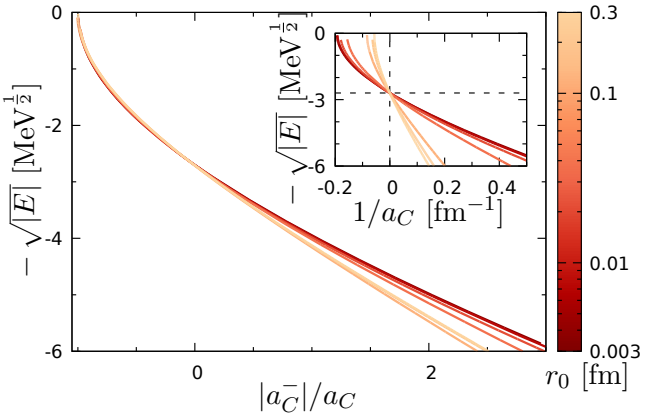

Figure 5.10: The trimer energies in the 3α system for different values of the range of the Gaussian potential r_0. The curves are color-coded according to the size of r_0. The inset shows the results without rescaling of a_C, the outer figure shows the same results with rescaled Coulomb-modified scattering length. A three-body force was used to fit the trimer to the ^{12}C ground state at the α-α scattering length. The figure was first published in [66] under CC-BY 4.0 [143] with different notation.

As such it is essentially the same figure as the left panel of Fig. 5.6, with the mass and charge of α particles instead of ^{16}O and a proton. The universal curve lies on top of the points for small r_0 (dark cyan triangles). For large r_0, the binding energies do not match those of the universal curve even very close to the unitary limit, where $a_C \to \infty$.
Introducing a length scale

$$D = \frac{1}{\kappa\eta} = \frac{\hbar}{\alpha\mu c Z_1 Z_2}, \tag{5.24}$$

that characterises the Coulomb potential, Volosniev found that Eq. (5.21) led to

$$\kappa^2 \approx \frac{6}{Da_C} + \frac{18}{5a_C^2} \tag{5.25}$$

in the limit of a strong Coulomb interaction ($a_C \gg D$). Comparing this to the case for neutral particles, for which the expression is

$$\kappa^2 \propto \frac{1}{a_C^2}, \tag{5.26}$$

it is interesting to note that in the limit of a strong Coulomb force, κ^2 has a different dependence on a_C for $a_C \to \infty$.
In order to incorporate finite-range corrections in Eq. (5.21), one can replace a_C^{-1} in this equation by

$$\frac{1}{a_C} + \frac{1}{2} r_{\text{eff}}^C \kappa^2, \tag{5.27}$$

which corresponds to the next term in the Coulomb-modified effective range expansion (compare Eq. (2.15)).
This yields [66]

$$2\eta \frac{\Gamma'(\eta)}{\Gamma(\eta)} - 2\eta \ln(\eta) + 1 = -\frac{1}{\kappa}\left(\frac{1}{a_C} + \frac{r_{\text{eff}}^C \kappa^2}{2}\right). \tag{5.28}$$

This will lead to a leading order expression for κ^2 for $a_C \gg D$ that contains r_{eff}^C:

$$\kappa^2 \approx \frac{6}{a_C D} \frac{1}{1 - 3\frac{r_{\text{eff}}^C}{D}}. \tag{5.29}$$

This means that if one corrects a_C by this additional factor

$$(1 - 3\frac{r_{\text{eff}}^C}{D}), \tag{5.30}$$

the results for different r_0 should coincide for small κ. This is shown in Fig. 5.9a). It can be seen that this is actually the case even for fairly large r_0 that are comparable to the size of the system. From this equation it is also very clear that r_{eff}^C contributes at leading order in this case, which explains why r_0 had to be fixed to reproduce r_{eff}^C in Section 5.6.1 and Section 5.6.2 in order to make comparisons to experimental values.

Trimer

Moving on to the three-body system, Fig. 5.10 shows the convergence of the binding energy of the trimer of three α-particles for $r_0 \to 0$, which coincides with $r_{\text{eff}}^C \to 0$ as has been shown in the right panel of Fig. 5.6 and in Fig. 5.7. The trimer has been fixed to the ground state of ^{12}C at the α-α scattering length $a_{\alpha\alpha}$, which is very close to $a_C^{-1} = 0$, using a three-body force (Eq. (3.79)). This leads to a different three-body potential strength W_0 for each r_0.
In the inset of Fig. 5.10 results for different r_0 between 0.003 fm and 0.3 fm are shown. It is easy to see that for $r_0 \to 0$ the curves converge. This converged curve is also shown in Fig. 5.12.

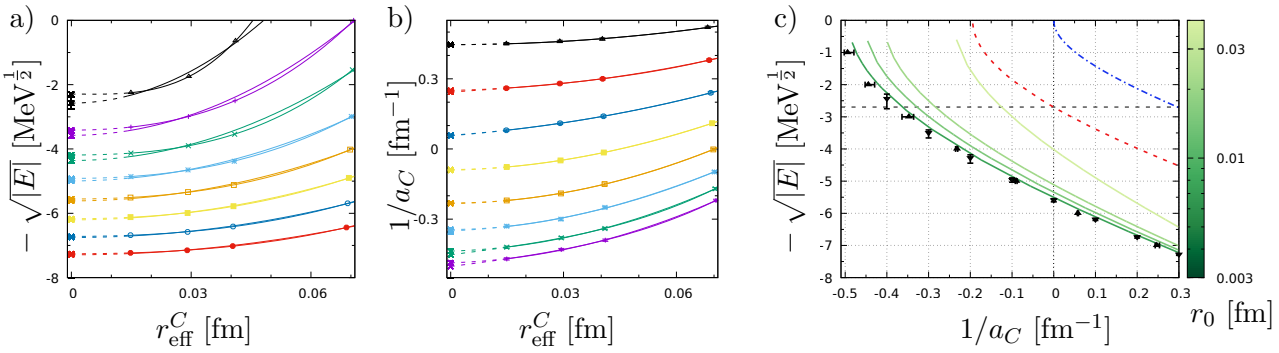

Figure 5.11: Extrapolation of the tetramer results. *Panel a)* shows the extrapolation with fixed scattering length for several different scattering lengths, corresponding to the vertical grid lines in panel c), while *panel b)* shows the extrapolation with fixed binding energy for several different binding energies corresponding to the horizontal grid lines in panel c). *Panel c)* shows the results for the tetramer binding energy for different r_0 with the three-body force fixed in the same way as the corresponding trimer. It also shows the result of the extrapolation in black, alongside the zero-range limit for the trimer (dashed red line) and for the dimer (dash-dotted blue line). This figure was modified from the version published in the supplementary material of [66] under CC-BY 4.0 [143] by adjusting the notation.

Similarly to the rescaling of a_C for the dimer, one can also rescale a_C for the trimer and finds coinciding curves for small energies. However, this has been done in Fig. 5.10 simply by extracting a_C^-, the point where the trimer vanishes at the 3α breakup threshold, and dividing by a_C^- for each curve. In future work, it would be interesting to find an expression like Eq. (5.30) for the rescaling factor in the three-body sector.
In addition to that, the inset of Fig. 5.12 shows that instead of tuning the three-body force to a specific value, as has been done here, one can also just scale the binding energy by a three-body parameter κ_3, while at the same time scaling a_C appropriately, to obtain matching curves. This means that the results shown here are not specific to the way the three-body force was tuned and very similar results are expected when tuning the three-body force to a different trimer binding energy.

Tetramer

In the four-body sector, an interesting question to answer is whether the tetramer binding energy curve converges for $r_{\text{eff}}^C \to 0$ if the same three-body force as for the trimer is used for each r_0.
The curves for the smallest r_0 accessible numerically ($r_0 = 0.0075\,\text{fm}, 0.0150\,\text{fm}, 0.0212\,\text{fm}$ and $0.0374\,\text{fm}$) are shown in Fig. 5.11c). Since they are not quite converged in the accessible r_0 range, an extrapolation is needed to estimate the results in the zero-range limit.
To extrapolate, points read off from Fig. 5.11c) for several fixed a_C (shown in Fig. 5.11a)) and several fixed E (shown in Fig. 5.11b)) were fitted by

$$f(r_{\text{eff}}^C) = a_1 r_{\text{eff}}^C + c_1 (r_{\text{eff}}^C)^2 + b_1, \tag{5.31}$$

with potentially different a_1, c_1, b_1 for each set of points. This function was chosen because one would expect an analytic function near $r_{\text{eff}}^C = 0$. This fit yields b_1 with an associated error e_1 that comes from the fitting procedure.
In order to obtain an error estimate, a second fit was done using one more term in the r_{eff}^C expansion:

$$f(r_{\text{eff}}) = a_2 r_{\text{eff}}^C + c_2 (r_{\text{eff}}^C)^2 + d_2 (r_{\text{eff}}^C)^3 + b_2. \tag{5.32}$$

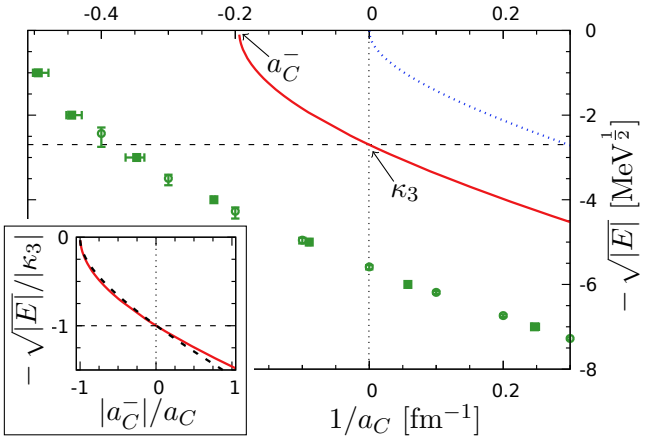

Figure 5.12: Zero range limit of the binding energies of the dimer (dotted blue line), trimer (solid red line) and tetramer (green points with errorbars). The mass and charge of the bosons are given by the α particle values. As for Fig. 5.10, a three-body force was used to fit the trimer to the binding energy of ^{12}C at $1/a_C \approx 0$. The inset shows trimer results for the same r_0 with different three-body forces. The energy is rescaled such that both curves coincide for $1/a_C = 0$ and the scattering length is rescaled such that both curves also coincide for $E = 0$. This figure was first published in [66] under CC-BY 4.0 [143].

Since there are four parameters for four points now, this will yield b_2 with the error $e_2 = 0$.
The difference between b_1 and b_2 together with the error e_1 can be used to make a conservative error estimate.
As result of this extrapolation the average of b_1 and b_2 is plotted together with error bars that have the lower end at $\min_i(b_i - e_i)$ and the upper end at $\max_i(b_i + e_i)$. This is shown in Fig. 5.11c) and Fig. 5.10.
The two extrapolation directions (for fixed a_C and for fixed E) agree well.
Regarding the value for the ^{16}O ground state binding energy that was obtained in this way in the zero-range limit, which is approximately 30 MeV, it is noted that it is very overbound as the binding energy of ^{16}O relative to the 4α breakup threshold is $\approx$ 14 MeV[140]. However, the zero-range limit is not expected to yield directly applicable results for charged particles. To make comparisons to physical systems, one would have to find a way to incorporate finite-range corrections similar to the two-body case, where the factor Eq. (5.30) was found.

6 Conclusions and Outlook

In this thesis I investigated two aspects of universality: The behaviour of trimer and tetramer states close to the dimer plus atom (plus atom) threshold in mixtures of heavy and light bosons and the influence of the Coulomb interaction on universal states. For both parts I used the GEM with Gaussian potentials for almost all calculations.

In the first part (Chapter 4), I investigated the experimentally relevant mass ratios $M/m = 7/6$, 87/7, and 133/6, which correspond to mixtures of ^{7}Li, ^{6}Li, ^{87}Rb and ^{133}Cs. I found that the trimer and tetramer vanish at almost the same point into the dimer + atom(s) threshold for all mass ratios investigated. This was not known a priori. In fact, it was not anticipated that the states vanish at the same point to such high accuracy.

This made the next part of that project, investigating the predictions about effective dimer-atom-atom Efimov states near the dimer-atom-atom threshold by [35, 51], more difficult. I extracted the difference between the points where the trimer and the tetramer vanish and interpreted them with the help of H.-W. Hammer in the three-body picture of the effective Efimov states. Some deviations from that picture where found, and it would be a worthwhile future project to calculate for more mass ratios and maybe a different potential to shed more light on these deviations.

Finding a second effective Efimov state in the region near the threshold proved impossible due to the high accuracy that would have had to be reached. It was even impossible to rule out the claim by [35] that the scaling factor λ is only 23 and not ≈ 2000 as was predicted in [51]. The future work outlined above might help to find a more favourable mass ratio where this would be possible.

In the second part (Chapter 5), I studied the interplay between the Coulomb interaction and the universal states. First, I introduced and used natural units and found that for a weak (in terms of the natural Coulomb scale) Coulomb potential strength the universal states are only subtly affected. The scaling factor between consecutive states is changed the most, while other aspects like the structure are relatively unaffected.

For stronger Coulomb force, more effects can be found. The excited trimer that was present in the weak-Coulomb case vanishes slowly from the breakup threshold downwards. The excited tetramer also vanishes in the same way. Looking at the structure of the trimers, the states become less dilute and are bounded by the Coulomb barrier. The rms radius approaches the range of the short-range potential r_0, which means that the states cease to be universal.

The applications to physical systems were successful for ^{17}F, but proved more challenging for ^{16}O and ^{12}C. The highest excited state of ^{16}O below the $N\alpha$ threshold (^{16}O (0_5^+)) could not be described within our framework, and further study is needed to find out why. A step in this direction would be to investigate resonances, i.e. states above the $N\alpha$ breakup threshold, of ^{12}C and ^{16}O. There, the universal aspects might survive longer and work in this region could point to ways to improve the description in order to describe ^{16}O (0_5^+). It was however shown that finite-range corrections are important and that therefore the effective range has to be fitted in addition to the scattering length, even in leading order.

This finding was formalised by A. G. Volosniev and I used this to present my results in a new light. Scaling the scattering length for the dimer using his correction factor, the results for different ranges of the short-range potential r_0 coincided and were shown to be universal near the threshold.

I also presented my results for the zero-range limit for the trimer and tetramer, where the latter had to be extrapolated because of slow convergence. It was shown that the trimer, too, could be brought to coincide for different r_0 if the scattering length was scaled appropriately.
It would be interesting to further investigate this and study whether a similar rescaling is possible for the tetramer.

Bibliography

1. Wigner, E. "Über die Streuung von Neutronen an Protonen". *Z. Phys.* **83,** 253–258 (1933).
2. Thomas, L. H. "The interaction between a neutron and a proton and the structure of H^3". *Phys. Rev.* **47,** 903–909 (1935).
3. Efimov, V. "Energy levels arising from resonant two-body forces in a three-body system". *Phys. Lett. B* **33,** 563–564 (1970).
4. Phillips, A. C. "Consistency of the low-energy three-nucleon observables and the separable interaction model". *Nucl. Phys. A* **107,** 209–216 (1968).
5. Tjon, J. A. "Bound states of ^{4}He with local interactions". *Phys. Lett. B* **56,** 217–220 (1975).
6. Amado, R. D. & Greenwood, F. C. "There is no Efimov effect for four or more particles". *Phys. Rev. D* **7,** 2517–2519 (1973).
7. Efimov, V. N. "Weakly-bound States of three resonantly-interacting Particles". *Sov. J. Nucl. Phys.* **12,** 589 (1971).
8. Efimov, V. "Low-energy Properties of Three Resonantly Interacting Particles". *Sov. J. Nucl. Phys.* **29,** 546 (1979).
9. Braaten, E., Hammer, H.-W. & Kusunoki, M. "Universal equation for Efimov states". *Phys. Rev. A* **67,** 022505 (2003).
10. Efimov, V. "Qualitative treatment of three-nucleon properties". *Nucl. Phys. A* **362,** 45–70 (1981).
11. Efimov, V. & Tkachenko, E. G. "On the correlation between the triton binding energy and the neutron-deuteron doublet scattering length". *Few Body Syst.* **4,** 71–88 (1988).
12. Platter, L., Hammer, H.-W. & Meißner, U.-G. "On the correlation between the binding energies of the triton and the α-particle". *Phys. Lett. B* **607,** 254–258 (2005).
13. Kievsky, A., Viviani, M., Gattobigio, M. & Girlanda, L. "Implications of Efimov physics for the description of three and four nucleons in chiral effective field theory". *Phys. Rev. C* **95,** 024001 (2017).
14. Nielsen, E., Fedorov, D. V. & Jensen, A. S. "The structure of the atomic helium trimers: halos and Efimov states". *J. Phys. B* **31,** 4085–4105 (1998).
15. Hammer, H.-W. & Higa, R. "A model study of discrete scale invariance and long-range interactions". *Eur. Phys. J. A* **37,** 193 (2008).
16. Tusnski, D. S., Yamashita, M. T., Frederico, T. & Tomio, L. "Continuum resonances with shielded Coulomb-like potential and Efimov effect". *Phys. At. Nucl.* **77,** 504–508 (2014).
17. Jensen, A. S., Riisager, K., Fedorov, D. V. & Garrido, E. "Structure and reactions of quantum halos". *Rev. Mod. Phys.* **76,** 215–261 (2004).
18. Ji, C. "Three-body systems in physics of cold atoms and halo nuclei". *Int. J. Mod. Phys. E* **25,** 1641003–269 (2016).

19. Hammer, H.-W., Ji, C. & Phillips, D. R. "Effective field theory description of halo nuclei". *J. Phys. G* **44,** 103002 (2017).

20. Raha, U., Kamiya, Y., Ando, S.-I. & Hyodo, T. "Universal physics of the few-body system of two neutrons and one flavored meson". *Phys. Rev. C* **98,** 034002 (2018).

21. Bedaque, P. F., Hammer, H.-W. & van Kolck, U. "The three-boson system with short-range interactions". *Nucl. Phys. A* **646,** 444–466 (1999).

22. Braaten, E. & Hammer, H.-W. "Universality in the three-body problem for ^{4}He atoms". *Phys. Rev. A* **67,** 042706 (2003).

23. Esry, B. D., Greene, C. H. & Burke Jr., J. P. "Recombination of three atoms in the ultracold limit". *Phys. Rev. Lett.* **83,** 1751–1754 (1999).

24. Bedaque, P. F., Braaten, E. & Hammer, H.-W. "Three-body recombination in Bose gases with large scattering length". *Phys. Rev. Lett.* **85,** 908–911 (2000).

25. Braaten, E. & Hammer, H.-W. "Enhanced dimer relaxation in an atomic and molecular Bose-Einstein condensate". *Phys. Rev. A* **70,** 042706 (2004).

26. Feshbach, H. "Unified theory of nuclear reactions". *Ann. Phys.* **5,** 357–390 (1958).

27. Chin, C., Grimm, R., Julienne, P. & Tiesinga, E. "Feshbach resonances in ultracold gases". *Rev. Mod. Phys.* **82,** 1225–1286 (2010).

28. Kraemer, T. *et al.* "Evidence for Efimov quantum states in an ultracold gas of cesium atoms". *Nature* **440,** 315–318 (2006).

29. Lee, M. D., Köhler, T. & Julienne, P. S. "Excited Thomas-Efimov levels in ultracold gases". *Phys. Rev. A* **76,** 012720 (2007).

30. Knoop, S. *et al.* "Observation of an Efimov-like trimer resonance in ultracold atom-dimer scattering". *Nat. Phys.* **5,** 227–230 (2009).

31. Huang, B., Sidorenkov, L. A., Grimm, R. & Hutson, J. M. "Observation of the second triatomic resonance in Efimov's scenario". *Phys. Rev. Lett.* **112,** 190401 (2014).

32. Braaten, E. & Hammer, H.-W. "Resonant dimer relaxation in cold atoms with a large scattering length". *Phys. Rev. A* **75,** 052710 (2007).

33. D'Incao, J. P. & Esry, B. D. "Enhancing the observability of the Efimov effect in ultracold atomic gas mixtures". *Phys. Rev. A* **73,** 030703 (2006).

34. Helfrich, K., Hammer, H.-W. & Petrov, D. S. "Three-body problem in heteronuclear mixtures with resonant interspecies interaction". *Phys. Rev. A* **81,** 042715 (2010).

35. Wang, Y., Laing, W. B., von Stecher, J. & Esry, B. D. "Efimov physics in heteronuclear four-body systems". *Phys. Rev. Lett.* **108,** 073201 (2012).

36. Blume, D. & Yan, Y. "Generalized Efimov scenario for heavy-light mixtures". *Phys. Rev. Lett.* **113,** 213201 (2014).

37. Acharya, B., Ji, C. & Platter, L. "Effective-field-theory analysis of Efimov physics in heteronuclear mixtures of ultracold atomic gases". *Phys. Rev. A* **94,** 032702 (2016).

38. Zaremba-Kopczyk, K., Żuchowski, P. S. & Tomza, M. "Magnetically tunable Feshbach resonances in ultracold gases of europium atoms and mixtures of europium and alkali-metal atoms". *Phys. Rev. A* **98,** 032704 (2018).

39. Platter, L., Hammer, H.-W. & Meißner, U.-G. "Four-boson system with short-range interactions". *Phys. Rev. A* **70,** 052101 (2004).

40. Hammer, H.-W. & Platter, L. "Universal properties of the four-body system with large scattering length". *Eur. Phys. J. A* **32,** 113–120 (2007).

41. von Stecher, J., D'Incao, J. P. & Greene, C. H. "Signatures of universal four-body phenomena and their relation to the Efimov effect". *Nat. Phys.* **5,** 417–421 (2009).

42. D'Incao, J. P., von Stecher, J. & Greene, C. H. "Universal four-boson states in ultracold molecular gases: Resonant effects in dimer-dimer collisions". *Phys. Rev. Lett.* **103,** 033004 (2009).

43. Gattobigio, M., Kievsky, A. & Viviani, M. "Spectra of helium clusters with up to six atoms using soft core potentials". *Phys. Rev. A* **84,** 052503 (2011).

44. von Stecher, J. "Five- and six-body resonances tied to an Efimov trimer". *Phys. Rev. Lett.* **107,** 200402 (2011).

45. Deltuva, A. "Properties of universal bosonic tetramers". *Few Body Syst.* **54,** 569–577 (2013).

46. Nicholson, A. N. "N-body Efimov states from two-particle noise". *Phys. Rev. Lett.* **109,** 073003 (2012).

47. Gattobigio, M., Kievsky, A. & Viviani, M. "Energy spectra of small bosonic clusters having a large two-body scattering length". *Phys. Rev. A* **86,** 042513 (2012).

48. Kievsky, A., Timofeyuk, N. K. & Gattobigio, M. "N-boson spectrum from a discrete scale invariance". *Phys. Rev. A* **90,** 032504 (2014).

49. Gattobigio, M. & Kievsky, A. "Universality and scaling in the N-body sector of Efimov physics". *Phys. Rev. A* **90,** 012502 (2014).

50. Yan, Y. & Blume, D. "Energy and structural properties of N -boson clusters attached to three-body Efimov states: Two-body zero-range interactions and the role of the three-body regulator". *Phys. Rev. A* **92,** 033626 (2015).

51. Braaten, E. & Hammer, H.-W. "Universality in few-body systems with large scattering length". *Phys. Rep.* **428,** 259–390 (2006).

52. Deltuva, A. "Universal bosonic tetramers of dimer-atom-atom structure". *Phys. Rev. A* **85,** 042705 (2012).

53. Deltuva, A. "Universal four-boson system: Dimer-atom-atom Efimov effect and recombination reactions". *Few Body Syst.* **54,** 1517–1521 (2013).

54. Barontini, G. *et al.* "Observation of heteronuclear atomic Efimov esonances". *Phys. Rev. Lett.* **103,** 043201 (2009).

55. Marzok, C. *et al.* "Feshbach resonances in an ultracold ^{7}Li and ^{87}Rb mixture". *Phys. Rev. A* **79,** 012717 (2009).

56. Pires, R. *et al.* "Observation of Efimov resonances in a mixture with extreme mass imbalance". *Phys. Rev. Lett.* **112,** 250404 (2014).

57. Maier, R. A. W., Eisele, M., Tiemann, E. & Zimmermann, C. "Efimov resonance and three-body parameter in a lithium-rubidium mixture". *Phys. Rev. Lett.* **115,** 043201 (2015).

58. Wang, F., Ye, X., Guo, M., Blume, D. & Wang, D. "Observation of resonant scattering between ultracold heteronuclear Feshbach molecules". *Phys. Rev. A* **100,** 042706 (2019).

59. Häfner, S. *et al.* "Role of the intraspecies scattering length in the Efimov scenario with large mass difference". *Phys. Rev. A* **95,** 062708 (2017).

60. Zenesini, A. *et al.* "Resonant five-body recombination in an ultracold gas of bosonic atoms". *New J. Phys.* **15,** 043040 (2013).

61. Voigtsberger, J. *et al.* "Imaging the structure of the trimer systems $^{4}He_3$ and $^{3}He^{4}He_2$". *Nat. Commun.* **5,** 5765 (2014).

62. Schmickler, C. H., Hammer, H.-W. & Hiyama, E. "Trimer and tetramer bound states in heteronuclear systems". *Few Body Syst.* **58,** 22 (2017).

63. Schmickler, C. H., Hammer, H.-W. & Hiyama, E. "Tetramer bound states in heteronuclear systems". *Phys. Rev. A* **95,** 052710 (2017).

64. Schmickler, C. H. "Universality and the Coulomb interaction". *Recent Progress in Few-Body Physics* (eds Orr, N. A., Ploszajczak, M., Marqués, F. M. & Carbonell, J.) (Springer International Publishing, Cham, 2020), 861–865. ISBN: 978-3-030-32357-8.

65. Schmickler, C. H., Hammer, H.-W. & Hiyama, E. "Efimov universality with Coulomb interaction". *Eur. Phys. J. A* **55,** 85 (2019).

66. Schmickler, C. H., Hammer, H.-W. & Volosniev, A. G. "Universal physics of bound states of a few charged particles". *Phys. Lett. B* **798,** 135016 (2019).

67. Sakurai, J. & Napolitano, J. *Modern Quantum Mechanics, 2nd Edition, International Edition.* ISBN: 9780321503367 (Addison-Wesley, 2011).

68. König, S. "Effective quantum theories with short- and long-range forces". PhD thesis (Rheinische Friedrich-Wilhelms-Universität Bonn, 2013).

69. Bethe, H. A. "Theory of the effective range in nuclear scattering". *Phys. Rev.* **76,** 38–50 (1949).

70. van Haeringen, H. & Kok, L. P. "Modified effective-range function". *Phys. Rev. A* **26,** 1218–1225 (1982).

71. Machleidt, R. & Entem, D. R. "Chiral effective field theory and nuclear forces". *Phys. Rep.* **503,** 1–75 (2011).

72. Grisenti, R. E. *et al.* "Determination of the bond length and binding energy of the helium dimer by diffraction from a transmission grating". *Phys. Rev. Lett.* **85,** 2284–2287 (2000).

73. Cencek, W. *et al.* "Effects of adiabatic, relativistic, and quantum electrodynamics interactions on the pair potential and thermophysical properties of helium". *J. Chem. Phys.* **136,** 224303–224303 (2012).

74. Naidon, P. & Endo, S. "Efimov physics: a review". *Rep. Prog. Phys.* **80,** 056001 (2017).

75. Efimov, V. "Level spectrum of three resonantly interacting particles". *Sov. J. Exp. Theor. Phys. Lett.* **16,** 34 (1972).

76. Deltuva, A. "Efimov physics in bosonic atom-trimer scattering". *Phys. Rev. A* **82,** 040701 (2010).

77. Mestrom, P. M. A., Wang, J., Greene, C. H. & D'Incao, J. P. "Efimov-van der Waals universality for ultracold atoms with positive scattering lengths". *Phys. Rev. A* **95,** 032707 (2017).

78. Giannakeas, P. & Greene, C. H. "Van der Waals universality in homonuclear atom-dimer elastic collisions". *Few Body Syst.* **58,** 20 (2017).

79. Ryberg, E., Forssén, C., Hammer, H.-W. & Platter, L. "Range corrections in proton halo nuclei". *Ann. Phys.* **367,** 13–32 (2016).

80. Higa, R., Hammer, H.-W. & van Kolck, U. "$\alpha\alpha$ scattering in halo effective field theory". *Nucl. Phys. A* **809,** 171–188 (2008).

81. Higa, R. "Exploring universality in nuclear clusters with Halo EFT". *Few Body Syst.* **50,** 251–253 (2011).

82. Fedorov, D. V. & Jensen, A. S. "The three-body continuum Coulomb problem and the 3α structure of ^{12}C". *Phys. Lett. B* **389,** 631–636 (1996).

83. Chernykh, M., Feldmeier, H., Neff, T., von Neumann-Cosel, P. & Richter, A. "Structure of the Hoyle state in ^{12}C". *Phys. Rev. Lett.* **98,** 032501 (2007).

84. Epelbaum, E., Krebs, H., Lähde, T. A., Lee, D. & Meißner, U.-G. "Structure and rotations of the Hoyle state". *Phys. Rev. Lett.* **109,** 252501 (2012).

85. Ohtsubo, S.-I., Fukushima, Y., Kamimura, M. & Hiyama, E. "Complex-scaling calculation of three-body resonances using complex-range Gaussian basis functions: Application to 3α resonances in ^{12}C". *Prog. Theor. Exp. Phys.* **2013,** 073D02 (2013).

86. Ikeda, K., Takigawa, N. & Horiuchi, H. "The systematic structure-change into the molecule-like structures in the self-conjugate 4n nuclei". *Prog. Theor. Phys. Suppl.* **E68,** 464–475 (1968).

87. Oryu, S., Kamada, H., Sekine, H., Nishino, T. & Sekiguchi, H. "Four-alpha model calculation for the ^{16}O nucleus by the four-body integral equation". *Nucl. Phys. A* **534,** 221–247 (1991).

88. Sofianos, S. A., Adam, R. M. & Belyaev, V. B. "α-cluster-model description of nuclei". *Phys. Rev. C* **84,** 064304 (2011).

89. Tohsaki, A. & Itagaki, N. "α clustering with a hollow structure: Geometrical structure of α clusters from platonic solids to fullerene shape". *Phys. Rev. C* **97,** 011301 (2018).

90. Braaten, E. & Hammer, H.-W. "Three-body recombination into deep bound states in a Bose gas with large scattering length". *Phys. Rev. Lett.* **87,** 160407 (2001).

91. Tung, S.-K., Jiménez-García, K., Johansen, J., Parker, C. V. & Chin, C. "Geometric scaling of Efimov states in a ^{6}Li-^{133}Cs mixture". *Phys. Rev. Lett.* **113,** 240402 (2014).

92. Ferlaino, F. *et al.* "Evidence for universal four-body states tied to an Efimov trimer". *Phys. Rev. Lett.* **102,** 140401 (2009).

93. Kunitski, M. *et al.* "Observation of the Efimov state of the helium trimer". *Science* **348,** 551–555 (2015).

94. Machtey, O., Shotan, Z., Gross, N. & Khaykovich, L. "Association of Efimov trimers from a three-atom continuum". *Phys. Rev. Lett.* **108,** 210406 (2012).

95. Hiyama, E., Kino, Y. & Kamimura, M. "Gaussian expansion method for few-body systems". *Prog. Part. Nucl. Phys.* **51,** 223–307 (2003).

96. Hiyama, E., Kamimura, M., Motoba, T., Yamada, T. & Yamamoto, Y. "Three-body model study of A=6-7 hypernuclei: Halo and skin structures". *Phys. Rev. C* **53,** 2075–2085 (1996).

97. Hiyama, E., Kamimura, M., Motoba, T., Yamada, T. & Yamamoto, Y. "Three- and four-body cluster models of hypernuclei using the G-matrix ΛN interaction – ${}^{9}_{\Lambda}$Be, ${}^{13}_{\Lambda}$C, ${}^{6}_{\Lambda\Lambda}$He and ${}^{10}_{\Lambda\Lambda}$Be". *Prog. Theor. Phys.* **97,** 881–899 (1997).

98. Hiyama, E., Kamimura, M., Miyazaki, K. & Motoba, T. "γ transitions in A=7 hypernuclei and a possible derivation of hypernuclear size". *Phys. Rev. C* **59,** 2351–2360 (1999).

99. Hiyama, E., Kamimura, M., Motoba, T., Yamada, T. & Yamamoto, Y. "Λ-Σ conversion in ${}^{4}_{\Lambda}$He and ${}^{4}_{\Lambda}$H based on a four-body calculation". *Phys. Rev. C* **65,** 011301 (2002).

100. Hiyama, E., Kamimura, M., Motoba, T., Yamada, T. & Yamamoto, Y. "Four-body cluster structure of A=7-10 double-Λ hypernuclei". *Phys. Rev. C* **66,** 024007 (2002).

101. Hiyama, E., Kamimura, M., Yamamoto, Y. & Motoba, T. "Five-body cluster structure of the double-Λ hypernucleus ${}^{11}_{\Lambda\Lambda}$Be". *Phys. Rev. Lett.* **104,** 212502 (2010).

102. Hiyama, E. & Kamimura, M. "Variational calculation of ^{4}He tetramer ground and excited states using a realistic pair potential". *Phys. Rev. A* **85,** 022502 (2012).

103. Hiyama, E. & Kamimura, M. "Linear correlations between ^{4}He trimer and tetramer energies calculated with various realistic ^{4}He potentials". *Phys. Rev. A* **85,** 062505 (2012).

104. Hiyama, E. & Kamimura, M. "Universality in Efimov-associated tetramers in ^{4}He". *Phys. Rev. A* **90,** 052514 (2014).

105. Varga, K. & Suzuki, Y. "Precise solution of few-body problems with the stochastic variational method on a correlated Gaussian basis". *Phys. Rev. C* **52,** 2885–2905 (1995).

106. Suzuki, Y. & Varga, K. *Stochastic Variational Approach to Quantum-Mechanical Few-Body Problems. Lecture Notes in Physics. Monographs* **54.** ISBN: 9783-540-65152-7 (Springer, Berlin, Heidelberg, New York, 1998).

107. Suzuki, Y. & Takahashi, M. "α cluster condensation in ^{12}C and ^{16}O?" *Phys. Rev. C* **65,** 064318 (2002).

108. Mitroy, J. *et al.* "Theory and application of explicitly correlated Gaussians". *Rev. Mod. Phys.* **85,** 693–749 (2013).

109. Ritz, W. "Über eine neue Methode zur Lösung gewisser Variationsprobleme der mathematischen Physik". *J. Reine Angew. Math.* **135,** 1–61 (1908).

110. Kellner, G. W. "Die Ionisierungsspannung des Heliums nach der Schrödingerschen Theorie". *Z. Phys.* **44,** 91–109 (1927).

111. Hill, R. N. "Rates of convergence and error estimation formulas for the Rayleigh-Ritz variational method". *J. Chem. Phys.* **83,** 1173–1196 (1985).

112. Kukulin, V. I. & Krasnopol'sky, V. M. "A stochastic variational method for few-body systems". *J. Phys. G* **3,** 795–811 (1977).

113. `http://www.netlib.org/lapack/explore-html/dc/dd2/group__double_o_t_h_e_reigen_ga059beb16ce5345c3a2dfbf9692650401.html`.

114. Hiyama, E. personal communication. 2014.

115. Blume, D. personal communication. 2016.

116. Wang, Y. personal communication. 2017.

117. Freer, M., Horiuchi, H., Kanada-En'yo, Y., Lee, D. & Meißner, U.-G. "Microscopic clustering in light nuclei". *Rev. Mod. Phys.* **90,** 035004 (2018).

118. Morlock, R. *et al.* "Halo properties of the first $1/2^+$ state in ^{17}F from the ^{16}O(p,γ)^{17}F reaction". *Phys. Rev. Lett.* **79,** 3837–3840 (1997).

119. Adamowski, J. "Formation of Fröhlich bipolarons". *Phys. Rev. B* **39,** 3649–3652 (1989).

120. Alexandrov, A. S. & Mott, N. F. "Bipolarons". *Rep. Prog. Phys.* **57,** 1197–1288 (1994).

121. Devreese, J. T. & Alexandrov, A. S. "Fröhlich polaron and bipolaron: recent developments". *Rep. Prog. Phys.* **72,** 066501 (2009).

122. Kashirina, N. I. & Lakhno, V. D. "Large-radius bipolaron and the polaron-polaron interaction". *Phys.-Uspekhi* **53,** 431–453 (2010).

123. Frank, R. L., Lieb, E. H., Seiringer, R. & Thomas, L. E. "Bipolaron and N-polaron binding energies". *Phys. Rev. Lett.* **104,** 210402 (2010).

124. Deltuva, A. "Momentum-space calculation of four-boson recombination". *Phys. Rev. A* **85,** 012708 (2012).

125. Heydenburg, N. P. & Temmer, G. M. "Alpha-Alpha Scattering at Low Energies". *Phys. Rev.* **104,** 123–134 (1956).

126. Afzal, S. A., Ahmad, A. A. & Ali, S. "Systematic survey of the α-α interaction". *Rev. Mod. Phys.* **41,** 247–273 (1969).

127. Wüstenbecker, S. *et al.* "Atomic effects on α-α scattering to the ^{8}Be ground state". *Z. Phys. A* **344,** 205–217 (1992).

128. Bethe, H. & Peierls, R. “Quantum theory of the diplon”. *Proc. R. Soc. Lond. A* **148,** 146–156 (1935).

129. Demkov, Y. N. & Ostrovskii, V. N. *Zero-Range Potentials and Their Applications in Atomic Physics* (Plenum Press, New York, 1988).

130. Danilov, G. S. “On the three-body problem with short-range forces”. *Sov. J. Exp. Theor. Phys.* **13,** 349 (1961).

131. Jonson, B. “Light dripline nuclei”. *Phys. Rep.* **389,** 1–59 (2004).

132. Tanihata, I., Savajols, H. & Kanungo, R. “Recent experimental progress in nuclear halo structure studies”. *Prog. Part. Nucl. Phys.* **68,** 215–313 (2013).

133. Greene, C. H., Giannakeas, P. & Pérez-Ríos, J. “Universal few-body physics and cluster formation”. *Rev. Mod. Phys.* **89,** 035006 (2017).

134. Bringas, F., Yamashita, M. T. & Frederico, T. “Triatomic continuum resonances for large negative scattering lengths”. *Phys. Rev. A* **69,** 040702 (2004).

135. Ulmanis, J. *et al.* “Universal three-body recombination and Efimov resonances in an ultracold Li-Cs mixture”. *Phys. Rev. A* **93,** 022707 (2016).

136. Fedorov, D. V., Jensen, A. S. & Riisager, K. “Three-body halos: Gross properties”. *Phys. Rev. C* **49,** 201–212 (1994).

137. Meißner, U.-G. “Anthropic considerations in nuclear physics”. *Sci. Bull.* **60,** 43–54 (2015).

138. Adams, F. C. & Grohs, E. “Stellar helium burning in other universes: A solution to the triple alpha fine-tuning problem”. *Astropart. Phys.* **87,** 40–54 (2017).

139. Suno, H., Suzuki, Y. & Descouvemont, P. “Triple -α continuum structure and Hoyle resonance of ^{12}C using the hyperspherical slow variable discretization”. *Phys. Rev. C* **91,** 014004 (2015).

140. Tilley, D. R., Weller, H. R. & Cheves, C. M. “Energy levels of light nuclei A = 16-17”. *Nucl. Phys. A* **564,** 1–183 (1993).

141. Kelley, J. H., Purcell, J. E. & Sheu, C. G. “Energy levels of light nuclei A = 12”. *Nucl. Phys. A* **968,** 71–253 (2017).

142. Tilley, D. R. *et al.* “Energy levels of light nuclei A=8,9,10”. *Nucl. Phys. A* **745,** 155–362 (2004).

143. *Creative Commons - Attribution 4.0 International (CC BY 4.0).* `https://creativecommons.org/licenses/by/4.0/`.

Appendices

A Radial Equation for S-Waves

Starting from the well-known radial Schrödinger equation

$$\left(-\frac{\hbar^2}{2mr^2}\frac{\mathrm{d}}{\mathrm{d}r}\left(r^2\frac{\mathrm{d}}{\mathrm{d}r}\right)+\frac{\hbar^2 l(l+1)}{2mr^2}+V(r)\right)R(r)=ER(r) \tag{A.1}$$

with $R(r)$ the radial part of the wave function

$$\psi(r,\Omega)=R(r)Y_{lm}(\Omega), \tag{A.2}$$

we can define a new radial wave function

$$u(r)=rR(r). \tag{A.3}$$

For $l=0$ this yields the equation

$$-\frac{\hbar^2}{2mr^2}\frac{\mathrm{d}}{\mathrm{d}r}r^2\frac{\mathrm{d}}{\mathrm{d}r}\frac{u(r)}{r}+V(r)\frac{u(r)}{r}=E\frac{u(r)}{r}. \tag{A.4}$$

Working out the derivative, this can be rewritten as

$$-\frac{\hbar^2}{2mr}\frac{\mathrm{d}^2}{\mathrm{d}r^2}u(r)+V(r)\frac{u(r)}{r}=E\frac{u(r)}{r}. \tag{A.5}$$

Multiplying by r then results in

$$-\frac{\hbar^2}{2m}\frac{\mathrm{d}^2}{\mathrm{d}r^2}u(r)+V(r)u(r)=Eu(r), \tag{A.6}$$

which is the Schrödinger equation in one dimension. If we are not interested in the actual wave-functions, but just in the phase shift, we can use the one-dimensional Schrödinger equation for the calculation. It is of course also possible to get back $R(r)$ by using Eq. (A.3).

A.1 The Scattering Amplitude

To show the relationship of the phase shift defined through the scattering amplitude, like it is done in [67], with the more intuitive definition of the s-wave phase shift presented in Section 2.1, one has to calculate $f(\theta)$, the scattering amplitude. It is connected to the phase shifts through

$$f(\theta)=\frac{1}{k}\sum_l(2l+1)e^{i\delta_l}\sin\delta_l P_l(cos\theta), \tag{A.7}$$

$$f(\theta)=\sum_l(2l+1)f_l P_l(cos\theta), \tag{A.8}$$

where θ is the angle between the incoming and outgoing momenta and $P_l(cos\theta)$ are the Legendre Polynomials. The partial-wave scattering amplitude f_l is

$$f_l = \frac{e^{i\delta_l}\sin\delta_l}{k} = \frac{1}{k\cot\delta_l - ik}. \tag{A.9}$$

Here, the widely used definition that can be found in [67] is used.
The scattering amplitude describes the scattering of the outgoing wave. For an incident plane wave, the total wave function is:

$$\Phi(r) = e^{ikz} + f(\theta)\frac{e^{ikr}}{r}. \tag{A.10}$$

To get an expression for the partial-wave scattering amplitude in terms of the wave function one has to expand this expression on both sides in terms of partial waves using spherical Bessel functions ($j_l(x)$):

$$\sum_l (2l+1)\left(i^l j_l(kr) + f_l\frac{e^{ikr}}{r}\right)P_l(\cos\theta) = \sum_l A_l(2l+1)\frac{\phi_l(r)}{r}P_l(\cos\theta), \tag{A.11}$$

with A_l a prefactor. Because of the orthogonality of the Legendre polynomials, the equation has to hold for each l separately. For $l = 0$, the equation becomes

$$j_0(kr) + f_0\frac{e^{ikr}}{r} = A_0\frac{\phi_0(r)}{r}. \tag{A.12}$$

For $\phi_0(r)$ we take

$$\phi_0(r) = \sin(kr + \delta), \tag{A.13}$$

which is a general solution of the outside part of Eq. (2.4) and corresponds to Eq. (2.5) via

$$\sin(kr+\delta) = \cos\delta\sin(kr) + \sin\delta\cos(kr) \tag{A.14}$$

$$= \cos\delta(\sin(kr) + \tan\delta\cos(kr)). \tag{A.15}$$

Eq. (A.12) then becomes

$$r\frac{\sin(kr)}{kr} + f_0 e^{ikr} = A_0\sin(kr+\delta). \tag{A.16}$$

This can be rewritten as

$$\frac{1}{2ik}(e^{ikr} - e^{-ikr}) + f_0 e^{ikr} = \frac{A_0}{2i}(e^{ikr}e^{i\delta} - e^{-ikr}e^{-i\delta}). \tag{A.17}$$

Comparing coefficients for e^{ikr} and e^{-ikr} yields

$$\frac{1}{2ik} + f_0 = \frac{A_0}{2i}e^{i\delta} \quad \text{and} \tag{A.18}$$

$$-\frac{1}{2ik} = -\frac{A_0}{2i}e^{-i\delta}. \tag{A.19}$$

A_0 is then

$$A_0 = \frac{1}{k}e^{i\delta} \tag{A.20}$$

and f_0 can be expressed as

$$f_0 = -\frac{1}{2ik} + \frac{1}{2ik}e^{2i\delta} = \frac{1}{2ik}(e^{2i\delta} - 1) = \frac{e^{i\delta}}{2ik}(e^{i\delta} - e^{-i\delta}), \tag{A.21}$$

which corresponds exactly to the expression for f_0 from Eq. (A.9) and thus,

$$\delta = \delta_0, \tag{A.22}$$

the s-wave scattering phase shift.

B Scattering Length and Phase Shift

One intuitive way presented in [67] to see the connection between scattering length and phase shift is considering that the solution for the outside wave function Eq. (2.5) can be rewritten as

$$\cos\delta(\sin(kr) + \tan\delta\cos(kr)) = \cos\delta\sin(kr) + \sin\delta\cos(kr) \tag{B.1}$$

$$= \sin(kr + \delta) = \phi(r). \tag{B.2}$$

The phase shift the δ describes is the difference between the phase of the free solution $\sin(kr)$ and the solution taking into account a non-zero short-range potential. Taking the low-energy limit, i.e. $k \to 0$, Eq. (2.4) for the outside wave function becomes

$$\frac{\partial^2\varphi(r)}{\partial r^2} = 0, \tag{B.3}$$

which can be solved by

$$\varphi(r) = N(r - a), \tag{B.4}$$

where N is a normalisation coefficient and a will turn out to be the scattering length. Taking the logarithmic derivative of $\phi(r)$, one finds

$$\frac{\phi'(r)}{\phi(r)} = \frac{k\cos(kr + \delta)}{\sin(kr + \delta)} = k\cot(kr + \delta), \tag{B.5}$$

while for $\varphi(r)$ we get

$$\frac{\varphi'(r)}{\varphi(r)} = \frac{N}{N(r - a)}. \tag{B.6}$$

At $r = 0$ the last two equations, which should be the same in the limit $k \to 0$, yield

$$\lim_{k\to 0} k\cot\delta = -\frac{1}{a}, \tag{B.7}$$

which corresponds to Eq. (2.1).

C Contourplot

In order to visualise the structure of three-body states without noise that comes from different spatial orientations of apart from this the same configurations, the following procedure is used.

We sample triplets of points $(\mathbf{r}_1, \mathbf{r}_2, \mathbf{r}_3)$ in a box of size L, with the constraint that the center of mass is at the origin of the box. This does not exclude any sampled configuration, because it can just be shifted accordingly, and is the easiest way to handle this, because our wave function is also in the center of mass frame.

To illustrate, we use some example triplets. As a first step, the determined points are rotated into the xy-plane. Since there are only three points, this is always possible.

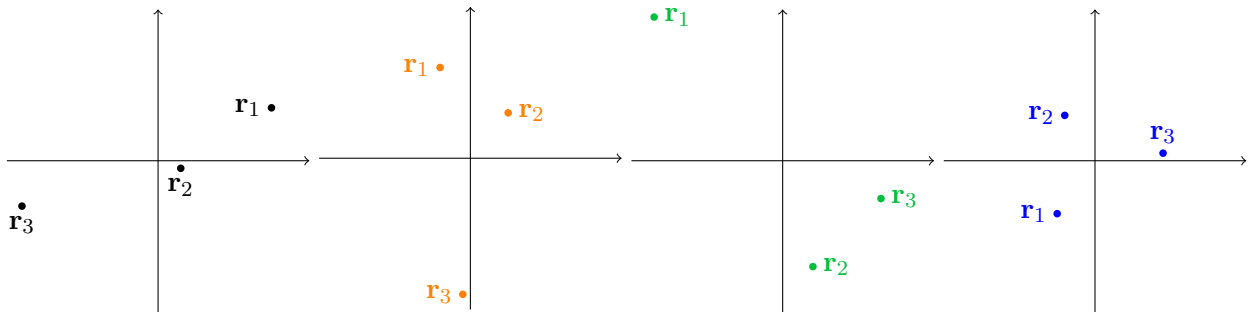

To determine the probability of the three particles being in that spatial configuration, we calculate the square of the total wave function for these parameters.

$$P(\mathbf{r}_1, \mathbf{r}_2, \mathbf{r}_3) = \Psi(\mathbf{r}_1, \mathbf{r}_2, \mathbf{r}_3)^2, \tag{C.1}$$

where Ψ is defined in Eq. 3.29.

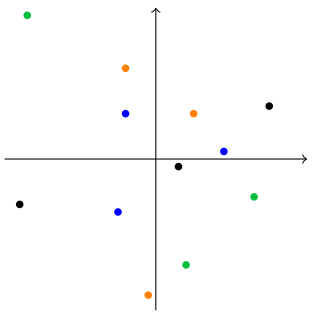

Now, to be able to discern an overall structure, it is important to sort the configurations in some way. Otherwise the different spatial orientations will wash out much of the structure.
Note that in the figure here the probabilities have not been taken into account yet, but for example assuming that the black, orange and green configurations were all equally probable being elongated triangles, and the blue one was less probable, one could not discern that elongated triangles were favoured from a plot aggregated from the orange, black and green points without further processing.

In the sorting scheme employed here, the principal axis with the smallest moment of inertia is determined and the points are rotated about the origin such that it lies on the y-axis.
In the figure the principal axis about which the points have to be rotated to have the smallest moment of inertia are shown as lines in the same colour as the points they belong to. The angles about which the configurations are rotated are also shown where possible. The line for the orange points already lies on the y-axis, so the orange points will not be rotated.

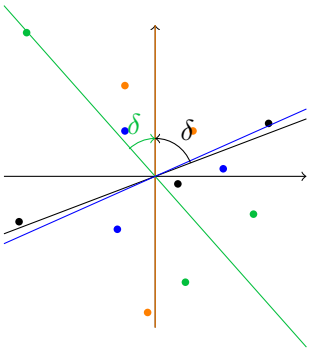

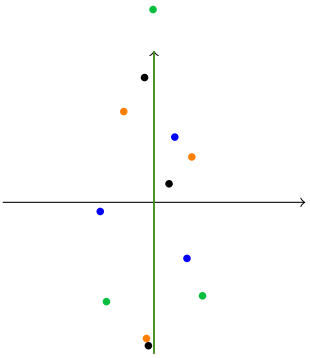

As a result, a somewhat elongated shape already crystallises, but aggregated into a plot at this stage, nothing could be said beyond that.
It should be noted that at this stage, even though there are only two requirements (center of mass frame plus principal axis with smallest moment of inertia on y-axis), we already achieved that there is only at most one particle of each configuration in a given quadrant.

Now, what remains to be done is mirrorring the points on the x- and y-axis to empty the left upper quadrant and to achieve a situation where exactly one particle is in each of the other quadrants.
If the configuration already fulfills the condition, the mirrorring steps are skipped (for example the blue points, and for the second step the green points).

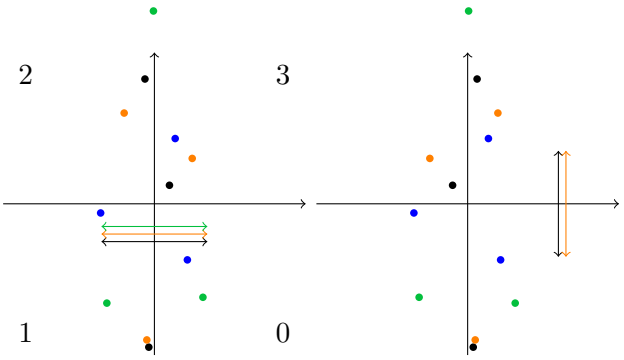

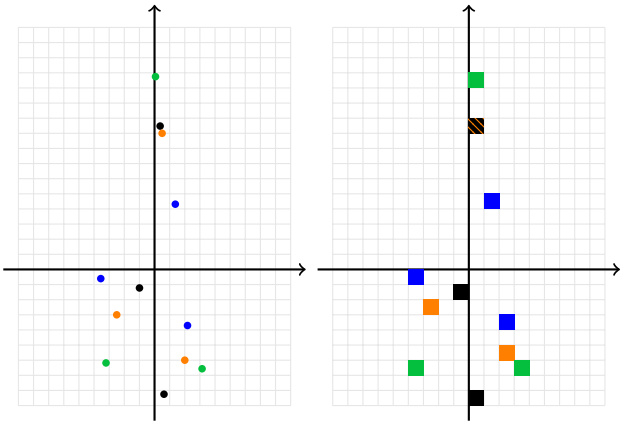

The last step is now to define a grid and place the points into bins. When the bin the point belongs in is identified, the probability that was calculated in the beginning for the configuration the point belongs to is added to this bin.

Since the probability is added to three bins (one for each point that belongs to the configuration), the sum over each quadrant should give the same total probability. Normalising appropriately the sum for each quadrant should be 1, corresponding to the one particle that can be found in each quadrant.
The figure shows the simplistic case of each sampled configuration being equally probable, leading to a distribution of equal probability P (black squares) and one square shown in red that has a probability $2P$.

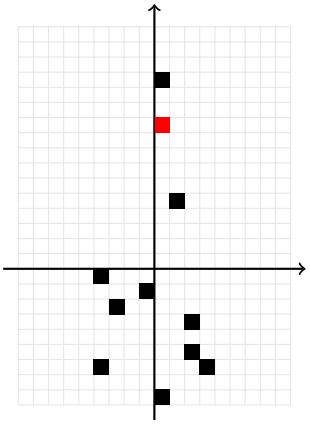

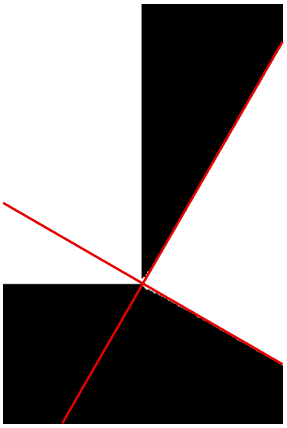

To understand better what can and cannot be seen on this kind of plot, it helps to visualise forbidden regions, where because of the constraints that were introduced no particle can be located.
Using a larger sample size and plotting which bins received at least one particle from any configuration, it is revealed that in addition to the explicitly forbidden region in the left upper quadrant, there is a second forbidden region which is formed by

$$y_b > \sqrt{3}x_b \quad \text{and} \quad y_c < -\frac{x_c}{\sqrt{3}}, \tag{C.2}$$

where we named the particle in the left lower quadrant particle a with coordinates x_a, y_a and the particles in the right upper and lower quadrants b and c, respectively.

An additional point that should be made is that around the edges of such a plot, shapes arise that are due to sampling points coming from within a box of a certain size L. The treatment described in this section then leads to the aforementioned peculiar shapes.
This means that when using this kind of plot one should take care that the areas of high probability are far away from the edges, such that missing contributions from points outside the sampling box can be ruled out.
One should also keep in mind that the hard edges in general result from tipping points, where were a particle to cross over that edge, the resulting configuration would be treated differently in the process.
An example would be if the particle in the lower left quadrant crosses over continuously into the upper left quadrant. In that case, during the step where the whole configuration is mirrored along the x-axis depending on the presence of a particle in the upper left quadrant, an additional flip would take place, if the particle is in the upper left quadrant, placing the particle back in the lower left quadrant.

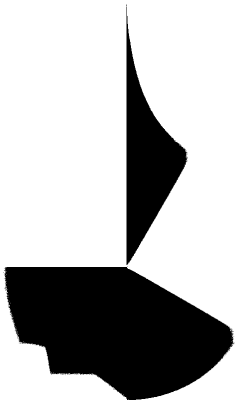

After considering the constraints the process poses on the resulting figure, it is now much more clear what one would expect to see.
The general size of the state can easily be seen by looking at the regions of highest probability for each particle, provided the size of the sampling box L is large enough.
In addition, if elongated triangles are preferred, then the regions of highest probability will appear near the y-axis.
If an equilateral triangle is the configuration with the highest probability, then this will appear

as prominent regions of high probability in the respective middle of the allowed region for each particle.
In general, it is useful to remember that the process to produce these plots does not include anything that distorts the configurations of particles; it only sorts them to make preferred shapes visible.

Acknowledgements

I would like to thank the people who supported and encouraged me during the work for this thesis. First of all I would like to thank Prof. Hans-Werner Hammer, my thesis advisor, for his help and advice over the years, for suggesting interesting topics to me and providing encouragement. I would also like to thank him for encouraging me to present my work from an early stage to international audiences.
I would also like to thank Prof. Emiko Hiyama, whom I was lucky to be able to visit and learn from after the completion of my Master's degree. During my stay at RIKEN, she taught me her method (the Gaussian Expansion Method (GEM)) and provided helpful advice and a stimulating environment. I would also like to thank the German Academic Scholarship Foundation (Studienstiftung des deutschen Volkes) for supporting my stay at RIKEN and opening up this opportunity for me.
Moreover, I would like to thank Dörte Blume for providing helpful explanations and additional data regarding her work, both in person and via correspondence. I would also like to thank Mario Gattobigio for discussions on the four-body universality and for explanations regarding his articles. Furthermore, I would like to thank Yujun Wang for providing additional information regarding his journal article. My thanks goes also to Artem Volosniev for the collaboration and stimulating discussions on the zero-range limit.
To the people at the institute in Darmstadt and at RIKEN, I would also like to say thank you for a supportive and stimulating environment. I am also grateful for the interesting opportunities that were provided by the SFB.
Lastly, I would like to thank Prof. Robert Roth for agreeing to evaluate this thesis.